



LUND UNIVERSITY

Nanofabricated Devices Based on Molecular Motors: Biosensing, Computation and Detection

Lard, Mercy

2014

[Link to publication](#)

Citation for published version (APA):

Lard, M. (2014). *Nanofabricated Devices Based on Molecular Motors: Biosensing, Computation and Detection*. [Doctoral Thesis (compilation), Solid State Physics].

Total number of authors:

1

General rights

Unless other specific re-use rights are stated the following general rights apply:

Copyright and moral rights for the publications made accessible in the public portal are retained by the authors and/or other copyright owners and it is a condition of accessing publications that users recognise and abide by the legal requirements associated with these rights.

- Users may download and print one copy of any publication from the public portal for the purpose of private study or research.
- You may not further distribute the material or use it for any profit-making activity or commercial gain
- You may freely distribute the URL identifying the publication in the public portal

Read more about Creative commons licenses: <https://creativecommons.org/licenses/>

Take down policy

If you believe that this document breaches copyright please contact us providing details, and we will remove access to the work immediately and investigate your claim.

LUND UNIVERSITY

PO Box 117
221 00 Lund
+46 46-222 00 00

Nanofabricated devices based on molecular motors

Biosensing, Computation and Detection

Mercy Lard
Doctoral thesis
2014



LUND
UNIVERSITY

DOCTORAL DISSERTATION

by due permission of the Faculty of Engineering, Lund University, Sweden.

To be defended at Rydbergsalen, Sölvegatan 14, Lund, Sweden. Date 12th
September 2014 and time 13:15.

Faculty opponent

Professor Henry Hess

Columbia University, New York, USA

Organization LUND UNIVERSITY		Document name Doctoral Dissertation	
Author: Mercy Lard		Date of issue 2014-9-12	
		Sponsoring organization	
Title and subtitle Nanofabricated devices based on molecular motors: Biosensing, Computation and Detection			
Abstract <p>The thesis describes the use of molecular motors in nanofabricated devices designed for potential applications in, biosensing, computation and detection. We utilize the well-established guiding principles for controlling the motion of actin filaments propelled by myosin molecular motors, and build upon these developments in order to improve upon previously demonstrated techniques, and establish new methods that, we believe, offer significant progress in these fields.</p> <p>One application area, in which use actin filaments and myosin motors, is in biosensing. Here we show that with the use of actomyosin, we can achieve fast concentration, due to the high speed of actin filaments, in a highly miniaturized molecular concentration device. This fast concentration, and small device footprint, will allow for rapid read-out and higher signal-to-noise ratios, of significance for the development of this field.</p> <p>We also demonstrate the use of 1D semiconductor nanowires, coated with an aluminum oxide shell, as light-guides for biosensing. Because of their high surface-area-to-volume ratio, these nanowires are capable of detecting many molecular probes over their total surface area. Each nanowire acts as an individual detector, with a high signal-to-noise ratio. These nanowires may be used for future detection of a variety of molecular probes rapidly and with high sensitivity.</p> <p>We also use actin filaments propelled by myosin motors, to solve a small-scale instance of a mathematical problem encoded in a 2D network of nanoscale channels, as a method of biocomputation. Due to their small size, high speed, low energy cost, and self-propelled motion, we show that molecular motors offer a significant improvement over alternative methods proposed for computing.</p> <p>Here, localized fluorescence interference contrast detectors were proposed as useful components in biocomputation, as a way to achieve more automated readout of large numbers of motile objects, a requirement for scaling in our biocomputation device. We also demonstrate the use of hollow nanowires to achieve transport of actin filaments by myosin motors within the 1D structures, for use in our biocomputation device. These hollow nanowires may also prove useful in the fundamental study of actin and myosin interactions.</p>			
Key words: biosensing, biocomputation, hollow nanowires, molecular motors, nanostructures, nanowires			
Classification system and/or index terms (if any)			
Supplementary bibliographical information		Language: English	
ISSN and key title		ISBN 978-91-7623-066-4	
Recipient's notes		Number of pages	Price
		Security classification	

I, the undersigned, being the copyright owner of the abstract of the above-mentioned dissertation, hereby grant to all reference sources permission to publish and disseminate the abstract of the above-mentioned dissertation.

Signature _____ Date 2014-08-01

Nanofabricated devices based on molecular motors

Biosensing, Computation and Detection

Mercy Lard



LUND
UNIVERSITY

Division of Solid State Physics
Department of Physics
Lund University
Sweden

Cover art: Image montage of nanofabricated devices taken from this thesis.

Copyright Mercy Lard

Faculty of Engineering
Department of Physics
Division of Solid State Physics
ISBN 978-91-7623-066-4 (print)
ISSN 978-91-7623-067-1 (electronic pdf)

Printed in Sweden by Media-Tryck, Lund University
Lund 2014



Contents

List of publications	7
Abstract	11
Popular science article	13
1. Introduction	17
2. Actomyosin	21
2.1. Motility assays	22
2.2. Motility assay applications	24
2.3. Fabrication nano-scale devices for <i>in vitro</i> motility assays	26
3. Biosensing with molecular motors	31
3.1. Molecular detection by concentration	32
3.1.1. First-generation device	32
3.1.2. Second-generation device	36
3.1.3. Future directions	38
3.2. Nanowires for molecular detection	39
3.2.1. Future applications	48
4. Computation devices	51
4.1. Computational problems	51
4.1.1. Subset Sum problem	54
4.2. Parallel computing methods	55
4.2.1. DNA computation	55
4.2.2. Quantum computation	57
4.2.3. Other computation techniques	59
4.3. Biocomputation with molecular motors	59
4.3.1. Device design	62
4.3.2. Error requirements and device performance	64
5. Achitectural elements	69
5.1. Detection: fluorescence contrast checkpoints	69
5.1.1. FLIC Theory	69
5.1.2. Device Design	71
5.1.3. Cross-correlation	72

5.2. Hollow nanowire tunnels	74
5.2.1 Hollow nanowire fabrication and alignment	75
5.2.2. Potential and future use	80
6. Conclusions	81
Abbreviations	83
Acknowledgements	87
References	89

List of publications

I. Ultrafast molecular motor driven nanoseparation and biosensing.

Lard, M.*, ten Siethoff*, L., Kumar, S., Persson, M., te Kronnie, G., Linke, H., Månsson, A. *Biosens. Bioelectron.* 48, 145-152 (2013).

I contributed to design of the devices and performed all fabrication of the devices. I contributed to motility assay experiments, and analyzed the data. I co-wrote the paper.

*Equal contribution

II. Molecular motor propelled filaments reveal light-guiding in nanowire arrays for enhanced biosensing.

ten Siethoff*, L., Lard, M.*, Generosi, J., Andersson, H. S., Linke, H., Månsson, A. *Nano Lett.* 14(2), 737-742 (2013).

I fabricated the devices, contributed to motility assay experiments and analysis of the data. I co-wrote the paper.

III. Massively-parallel computation with molecular motor-propelled agents in nanofabricated networks.

Nicolau, D. V. J.*, Lard, M.*, Korten, T.*, van Delft, F., Persson, M., Bengtsson, E., Månsson, A., Diez, S., Linke, H., Nicolau, D. V. *Under review* (2014).

I fabricated the devices for use with actomyosin, and contributed to design of the devices for actomyosin. I contributed to motility assay experiments with actomyosin and analysis of the data for actomyosin. I contributed to writing the paper.

IV. Tracking actomyosin at fluorescence check points.

Lard, M., ten Siethoff, L., Månsson, A., Linke, H. *Sci. Rep.* 3, 1092 (2013).

I fabricated the devices and contributed to planning the study. I performed the motility assay experiments, and analyzed the results. I wrote the paper.

V. Molecular motor transport through hollow nanowires.

Lard, M., ten Siethoff, L., Generosi, J., Månsson, A., Linke, H. *Nano Lett.* 14(6), 3041–3046 (2014).

I fabricated the devices, performed motility assay experiments, analyzed the data, and wrote the paper.

Publications outside the scope of this thesis:

VI. Antibodies Covalently Immobilized on Actin Filaments for Fast Myosin Driven Analyte Transport.

Kumar, S. ten Siethoff, L., Persson, M., Lard, M., te Kronnie, G., Linke, H., Månsson, A. *PLoS One* 7, e46298 (2012).

I contributed to analyzing the data, and to editing the paper. I also contributed motility assay experiments.

VII. Plasmon hybridization in pyramidal metamaterials: a route towards ultrabroadband absorption.

Lobet, M., Lard, M., Sarrazin, M., Deparis, O., Henrard, L. *Optics Express* 22(10), 12678-12690 (2014).

I contributed to editing and writing the paper.

VIII. Food Chain Transport of Nanoparticles Affects Behaviour and Fat Metabolism in Fish.

Cedervall, T., Hansson, L. A., Lard, M., Frohm, B., Linse, S. *PLoS ONE* 7(2), e32254 (2012).

I performed experiments and collected data. I contributed writing the paper.

IX. Tracking the Small with the Smallest – Using Nanotechnology in Tracking Zooplankton.

Lard, M., Bäckman, J., Yakovleva, M., Danielsson, B. & Hansson, L.-A. *PLoS ONE* 5(10), e13516 (2010).

I conceived of and designed the study. I performed experiments and analyzed the data. I wrote the paper.

Abstract

The thesis describes the use of molecular motors in nanofabricated devices designed for potential applications in biosensing, computation and detection. We utilize the well-established guiding principles for controlling the motion of actin filaments propelled by myosin molecular motors, and build upon these developments in order to improve upon previously demonstrated techniques, and establish new methods that, we believe, offer significant progress in these fields.

One application area, in which use actin filaments and myosin motors, is in biosensing. Here we show that with the use of actomyosin, we can achieve fast concentration, due to the high speed of actin filaments, in a highly miniaturized molecular concentration device. This fast concentration, and small device footprint, will allow for rapid read-out and higher signal-to-noise ratios, of significance for the development of this field.

We also demonstrate the use of 1D semiconductor nanowires, coated with an aluminum oxide shell, as light-guides for biosensing. Because of their high surface-area-to-volume ratio, these nanowires are capable of detecting many molecular probes over their total surface area. Each nanowire acts as an individual detector, with a high signal-to-noise ratio. These nanowires may be used for future detection of a variety of molecular probes rapidly and with high sensitivity.

We also use actin filaments propelled by myosin motors, to solve a small-scale instance of a mathematical problem encoded in a 2D network of nanoscale channels, as a method of biocomputation. Due to their small size, high speed, low energy cost, and self-propelled motion, we show that molecular motors offer a significant improvement over alternative methods proposed for computing.

Here, localized fluorescence interference contrast detectors were proposed as useful components in biocomputation, as a way to achieve more automated readout of large numbers of motile objects, a requirement for scaling in our biocomputation device. We also demonstrate the use of hollow nanowires to achieve transport of actin filaments by myosin motors within the 1D structures, for use in our biocomputation device. These hollow nanowires may also prove useful in the fundamental study of actin and myosin interactions.

Popular science article

Naturally occurring machines are ubiquitous in nature. For example, plants, algae and cyanobacteria use sunlight (radiant energy) and water to create fuel (energy-rich chemical substances), in the process of photosynthesis. These and other chemical substances are also used as energy sources for other reactions in nature, such as the generation of motion by molecular motors. Due to their high energy-efficiency, speed, flexibility and ability to transport cargo, these molecular motors have been proposed as nano-sized machines for use in, for example, diagnostics and drug discovery. Using state-of-the-art technology, it is possible to control these molecular motors in an artificial environment, and harness their unique self-propelled motion in a range of other applications. Figure 1 shows actin filaments transported by myosin motors over a planar substrate. The actin filament is labeled with fluorescent molecules to allow for viewing in a fluorescent microscope. This thesis is focused on the use of myosin motors, which transport actin filaments, however, the kinesin-microtubule motor system is also commonly used for similar techniques.

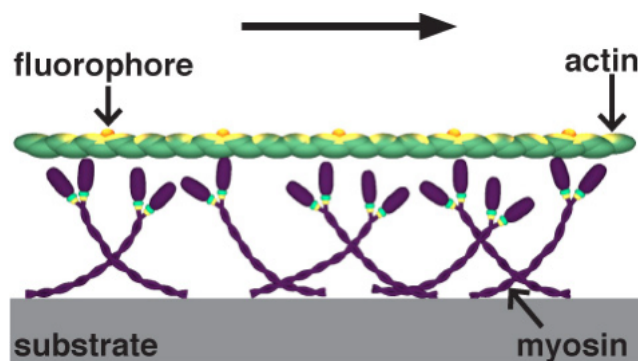


Figure 1. Schematic of actin filaments propelled by myosin motors. Myosin is immobilized on a substrate. Fluorescently labeled actin filaments glide along the surface as they are propelled by the myosin. The conformation of myosin is directly related to the surface properties of the substrate.

Nano-scale structures. The structural elements, used for controlling molecular motor motion, are typically a few hundred nanometers wide (1 nanometer is 1 billionth of a meter, e.g. 10,000 times smaller than the width of a human hair), and a few or few tens of micrometers long, having similar dimensions as the molecular

motors (myosin; 5 by 70 nanometers and actin; 10 by several 1000 nanometers). In this size range, many individual devices can be patterned onto millimeter-sized samples (chips), where experiments are carried out. This type of work is known as a lab-on-a-chip technology. Within this thesis I describe the fabrication of nano-scale structures, such as nanochannels and nanowires, on millimeter sized chips for two particular applications i.e. biosensing and biocomputation with molecular motors. The continued advancement of these types of structures will likely provide more opportunities for molecular motor research to expand in other areas of science and medical diagnostics.

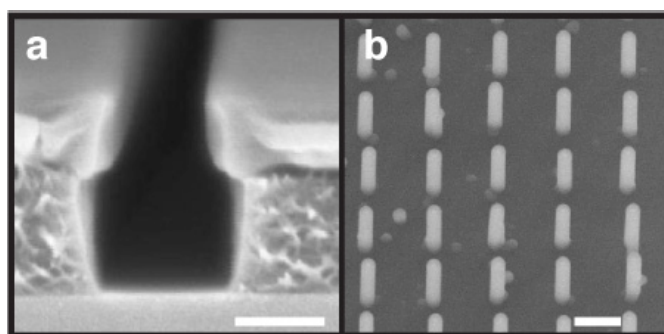


Figure 2. Scanning electron micrographs of nanostructures for molecular motor control. a) Cross-sectional view of nanochannel made from polymer resists on top of silicon oxide substrate. Guidance through these nanochannels is well controlled in one-dimension. Scale bar: 200 nm. b) Side view of nanowires for use in biosensing devices. These nanowires are coated with an aluminum oxide layer in order to achieve suitable adsorption of molecular motors for actin filament guidance. Nanowire diameter and length here is approximately 200 nm and 1 μm , respectively. Sample tilt: 30°. Scale bar: 500 nm.

Three-dimensional interactions. By harnessing the robustness of these molecular motors it has been shown previously, that a variety of devices can be made to control the molecular motors and cytoskeletal filaments outside of their natural environment. However, these studies use motors in two dimensions, which can be seen as a primary limitation in, for example, understanding how myosin interacts with the actin under physiological conditions. Therefore, I show here how hollow nano-sized tubes (hollow nanowires) can be used to achieve interactions, between actin and myosin in a three-dimensional environment, at physiological length scales. These hollow nanowires may also prove useful in other applications described below.

Biosensing and diagnostics. The primary aim of biosensing is to be able to identify the presence of a very small amount of a chemical substance, which is useful for example, in patient diagnostics. Through the use of molecular motors and engineered nano-structures there is a high potential to be able to sense foreign

molecules and diagnose patients, while using a very low sample volume. Recent demonstrations reveal that it is possible to collect and concentrate very small amounts of molecules on a chip using kinesin molecular motors transporting microtubules. Here, I show how myosin molecular motors transporting actin filaments can be used to concentrate molecules attached to actin in two-dimensions on a surface or in one-dimension on nanowires. Here, the devices operate in a much shorter temporal and spatial scale than those previously demonstrated devices. These results are highly relevant for fast diagnostics and performance in lab-on-a-chip technology.

Biocomputation. Molecular motors can also be useful within the field of computational mathematics. It is known that problems exist for which there is no fast way to determine a solution. These problems arise in areas of, for example, cryptography (encryption and decoding) and in optimization (network routing). An example optimization problem is the traveling salesman problem, which asks for the optimal (shortest) path that a salesman (motile agent) can take to visit all cities (points) on a map (network) exactly once. Such problems quickly become difficult for modern computers when the number of cities becomes very large. Molecular motors, however, have been proposed as a possible substitution. By finding solutions in parallel, they can effectively decrease the computation time. Here, I show how myosin and actin filaments can be used to find all solutions to a given instance of a problem mapped out into a two-dimensional network of nano-sized channels, in a fast and energetically efficient way. I also discuss the challenges of scaling-up such a device for solving computationally more challenging problems.

Architectural elements. While the above mentioned biocomputation device has potential for solving highly complex mathematical problems, the scaling up of such a device requires the development of architectural elements to increase performance. In scaling up these biocomputation devices, the number of agents (actin filaments) and outputs (solutions) also increases quickly. Therefore, I show here how oxide coated metal detectors can be used to count and track these filaments. A secondary requirement for biocomputation is to provide error-free computations, which can be extremely detrimental when scaling up such a device. Here, I show how hollow nanowires can be used to transport actin filaments in a fully enclosed one-dimensional channel. By using these hollow nanowires, it is possible to remove error in the biocomputation network and essentially eliminate error.

1. Introduction

The use of molecular motors in lab-on-a-chip technology has expanded over more than a decade, with the ability to control the motion of these motors spatially in 2D with micro-fabricated tracks ^{1,2}, to more recent demonstrations adding temporal control of motion with thermo-sensitive polymers ³ or caged release of ATP ⁴. With these developments, molecular motors have been proposed as valuable tools in a variety of applications ⁵. The utility of molecular motors has been demonstrated due to their speed and flexibility, or their robust cargo towing capabilities, depending on the type of motors and transporters used.

Molecular-motor based devices ⁶ offer a significant advantage over micro- and nanofluidics based devices due to their capability to run on a chemical fuel supply in order to transport molecules, rather than by externally driven power supplies ⁷. For example, in molecular motor powered devices, no external pressure is required to transport species, or to perform mixing and sorting, as is fundamental to fluidics devices, where pumps and external controls are critical to control of delivery ⁸⁻¹⁰. The two most common molecular motors used are myosin and kinesin, which transport actin filaments and microtubules, respectively. Each of these systems are capable of self-propelled motion by the conversion of adenosine triphosphate (ATP) into adenosine diphosphate (ADP) and an inorganic phosphate ion (P_i). In contrast to microfluidics platforms, much of the surfaces designed for microtubule and actin transport require less sample solution to operate. Thus these molecular motor systems are miniaturized, of particular relevance for lab-on-a-chip applications in biosensing ¹¹⁻¹³ and biocomputation ¹⁴. A detailed description of the actomyosin system including a brief discussion of previously developed molecular motor devices is provided within Chapter 2.

The need for fast, directed transport of biomolecules is critical for increased sensitivity in biosensing platforms ^{15,16}. Previously the kinesin-microtubule system has been used as an effective tool in biosensing devices, due to its capability to transport large cargos ^{12,17,18}. The actomyosin system offers other advantages, such as higher operating speeds, up to 10 times higher than the kinesin-microtubule system. Actin filaments are also more flexible than microtubules, and as such, allow for the possibility to miniaturize active capture regions required for delivering molecules to a detection area. Here we demonstrate the use of 2D nanostructures, related to those designed for kinesin-microtubule based

biosensing. We show that the actomyosin system is capable of faster delivery, while operating on a reduced total surface area. The reduction in size of detectors or capture regions is critical for effectively maximizing the use of space on a device¹³. We also demonstrate biosensing with actomyosin in a 1D platform using vertical nanowires. In this device many individual nanowire detectors can be arranged in a much smaller area than previous devices. These nanowires have high surface-area-to-volume ratios, thus they offer comparatively larger detection sites. This increase in the effective detector area allows for higher signal-to-noise ratios, a critical component in biosensing applications¹⁶. Both of these biosensing devices are described in Chapter 3, with a comparison to other recent developments.

In the field of computational mathematics, there exist problems which are computationally complex and therefore can be highly difficult to solve, such as optimized network routing^{19,20}, decryption of encoded messages²¹⁻²³ and predicting protein folding conformations²⁴⁻²⁶. For such problems, there are currently no existing efficient algorithms that can be used to find solutions in relatively fast time scales, particularly those problems for which the solution space grows exponentially. This is primarily a concern for modern computers that use serial processes to solve problems, and can therefore be overwhelmed with a quickly diverging solution space. Previously, alternative computation approaches have been developed, for example, DNA^{27,28}, quantum²⁹ and microfluidics-based¹⁰ computation. However, these systems have significant drawbacks in terms of scaling-up, an intrinsic parameter required for any meaningful computing approach. Molecular motors, however, have been proposed as another viable alternative, as they can perform with high fidelity and speed in order to solve problems in a highly parallel fashion³⁰. We have demonstrated the first use of molecular motors to solve a computation problem mapped out into a two-dimensional network of nano-sized channels, in a fast and energetically efficient way. Chapter 4 provides the results of this demonstration as well as a background on the computationally complex problems of interest, and alternative computing approaches.

The biocomputation devices mentioned above can quickly become more complex as the problems we would like to encode become more mathematically challenging due to scaling-up. As such, they require a large number of agents (actin or microtubules) to compute solutions. Therefore, we must rely on more sophisticated devices, which can efficiently detect or track agents as they enter and exit the network, which is a non-trivial problem. Here we show how fluorescence interference contrast (FLIC) detectors can be used to track and to monitor direction and speed of filaments. An increase in the sensitivity to error is a consequence of the scaling-up of these devices. Therefore, architectural elements are also needed to reduce or eliminate error caused by fluctuations in transport

throughout the network. Here we demonstrate the transport of actin filaments through hollow nanowires, for use as a potential error correction element in these biocomputation devices. Chapter 5 is dedicated to describing these architectural elements for detecting, sorting or collecting filaments, which can be implemented into biocomputation devices to alleviate such bottlenecks. Finally, Chapter 6 gives a brief outlook for the future of molecular-motor based devices, including some current limitations of the field.

2. Actomyosin

All experiments in this thesis were carried out using the actomyosin molecular motor system from rabbit skeletal muscle. Skeletal muscle is formed from bundles of myofibrils, which are made up of repeating sarcomere segments; see figure 2.1a, which are in turn comprised of actin, myosin and a range of regulatory and other proteins. Here bundles of the motor proteins (myosin) are arranged in hexagonal arrays surrounded by the thin filaments, comprised mainly of actin, figure 2.1c. The lattice spacing and sarcomere length depends highly on the type of muscle, as well as its state (rest or contracted)^{31,32}. Sarcomere length in the equilibrium or rest state is typically around 2.4 to 2.6 μm for rabbit skeletal muscle³¹.

The process of muscle contraction is complex, involving many factors³³⁻³⁵. A highly simplified view of the process is as follows. After calcium binding to the regulatory troponin-tropomyosin complex on the thin filaments, myosin binding sites on actin are exposed and myosin motor domains act collectively to pull the actin filaments, and in this way, they are responsible for muscle contraction. Upon dissociation of the actin-myosin links, as regulated by calcium dissociation from the troponin-tropomyosin complex, re-extension of the muscle occurs. Essentially, the pulling motion is generated by a chemical reaction called adenosine triphosphate (ATP) hydrolysis, which is the conversion of ATP into adenosine diphosphate (ADP) and an inorganic phosphate ion (P_i). This conversion results in a conformational change in the state of the myosin heads bound to actin filaments^{36,37}. Accordingly, the turnover of every single ATP molecule by one molecular motor will produce force of a few pN with a step size of a few nm³⁸⁻⁴⁰ acting on the actin filament causing it to move forward, in a process referred to as the power stroke³⁶. With the release of energy from ATP turnover $\sim 20 \text{ kT}$ ^{6,41}, the movement of myosin of a few nm, in the force range of a few pN, corresponds to mechanical energy of approximately 9 kT, yielding a thermodynamic efficiency up to $\sim 50\%$ ^{6,41}.

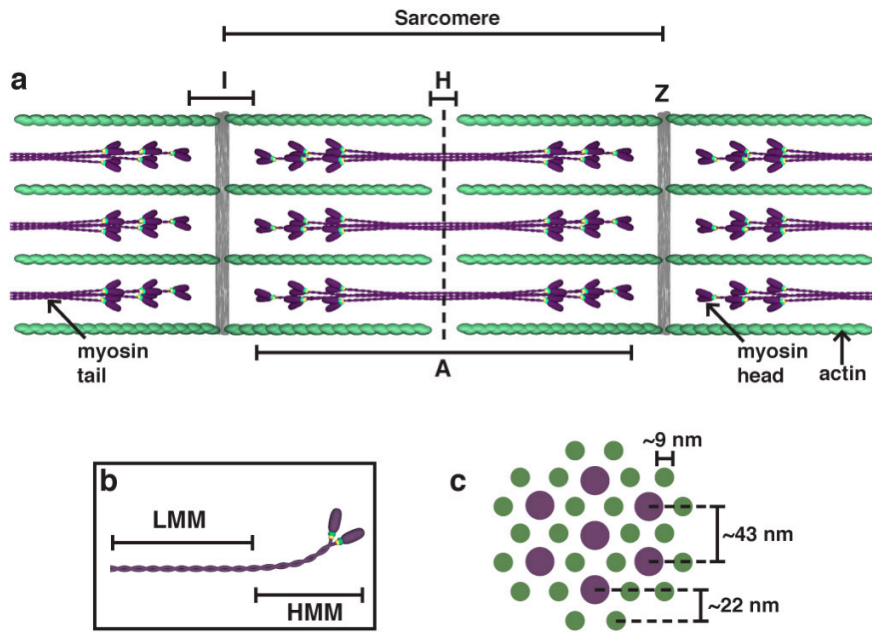


Figure 2.1. Schematic of the sarcomere. a) The sarcomere is the most basic repeating unit of muscle and is made up of thick and thin filaments. Myosins (thick filaments) are bundled together by their tails and join at the center (M-band). Myosins exist within the A-band and in the H-band. Actins-containing thin filaments are surrounded by the thick myosin-containing filaments in a hexagonal matrix. Actin filaments are found in the I-band and are tethered to the Z-line or disk, which divides the repeating sarcomere units. Figure based on ³⁴. b) Myosin is shown with two main fragments that are obtained e.g. by chymotryptic cleavage. These are denoted: light meromyosin (LMM), approximately 80 - 90 nm in length, comprising much of the myosin tail portion, and heavy meromyosin (HMM), approximately 60 – 70 nm in length, retaining the primary motor function with both motor domains (heads) ^{42,43}. c) Side view of the sarcomere lattice with approximate values given ^{34,44}.

2.1. Motility assays

In an *in vitro* motility assay (IVMA), molecular motors, extracted from their natural environment, are observed in two main configurations. In the bead assay, motors attached to fluorescent microspheres, walk over cytoskeletal filaments that are fixed on a surface ⁴⁵. In the gliding assay used here, we observe the motion of fluorescently labeled actin filaments as they are propelled by (glide over) HMM adsorbed to the substrate (Fig. 2.2a) ^{46,47}. Here, two glass slides, or a glass slide and a structured surface, are joined by double-sided tape in what is known as a flow cell (Fig.2.2b). The motors, filaments, assay and buffer solutions are flown in on one side, and drawn out of the other by capillary force. A heated objective is

used to observe the sample from below (Fig. 2.2c) on an inverted fluorescence microscope.

We utilize rabbit skeletal muscle for obtaining myosin II motors and actin filaments. However, depending on the application, other animal sources can be used for deriving myosin and actin filaments³². In our studies we use only a portion of myosin II, namely heavy meromyosin (HMM). HMM is formed by proteolytic digestion of myosin and retains its primary functionality in motility assays⁴⁸. Actin filaments or F-actin is formed from polymerization of G-actin (monomers) into a helical arrangement of 13 G-actin molecules per 6 left-handed turns in a 36 nm cross over structure (72 nm for full repeat)⁴⁴. Each G-actin monomer has dimensions of 5.5x5.5 nm sides with a depth of 3.5 nm⁴⁹. The actin filament is typically stabilized by phalloidin molecules, which can be fluorescently tagged for imaging the filaments⁴⁶. The filaments are typically fluorescently labeled with: Alexa-488 Phalloidin (Aph) or Rhodamine Phalloidin (RhPh)⁵⁰ and motion can be recorded with the use of a fluorescence microscope using appropriate filter sets: fluorescein isothiocyanate (FITC) or tetramethyl rhodamine iso-thiocyanate (TRITC) and a CCD camera.

Analysis of this motion can be performed using image analysis software such as ImageJ or Matlab and information such as the speed of the filaments can be evaluated^{51,52}. Further information on the quality of the substrate, i.e. the uniformity of the surface treatment or variations in topography, can be indirectly obtained using these types of assays^{53,54}. As myosin II are non-processive motors, they are not in constant contact with the filament. It has therefore been seen that under conditions where filaments are very short < 1 μm and/or HMM density is low, a methylcellulose solution is added to IVMAs to keep filaments close to the surface where motors are bound in order to facilitate transport³⁸. Typical filament lengths used in IVMAs presented here are observed to be a few micrometers, while HMM density is approximately 10 000 μm^{-2} ⁵⁵.

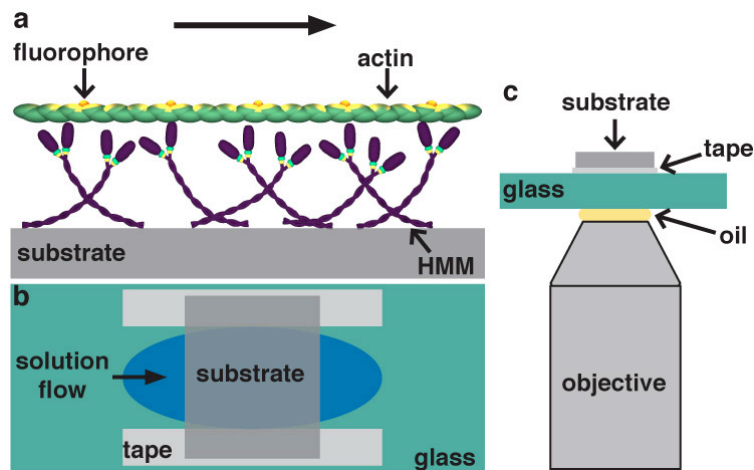


Figure 2.2. Schematic of actomyosin gliding assay and flow cell. a) HMM is immobilized on a glass surface. Fluorescently labeled actin filaments glide along the surface as they are propelled by the HMM molecules. The conformation of HMM is directly related to the surface properties⁵⁵. b) Flow cells are created by placing a substrate upside down on top of the glass support slide with double-sided tape used as spacers⁴⁸. Solutions of the HMM, actin and assay buffers are flown in from one side and drawn out on the other by a piece of filter paper. c) Viewing of the surface of the substrate is performed through the underside of glass slide with a temperature controlled oil immersion objective (with an inverted fluorescence microscope).

2.2. Motility assay applications

While actomyosin has been used with the aim to develop a variety of applications for diagnostics in lab-on-a-chip devices⁵⁶⁻⁶², other cytoskeletal proteins like the microtubule-kinesin system are also used in IVMA for many similar applications^{3,4,12,18,63-68}. The microtubule-kinesin system offers the benefits of the capacity for transporting larger cargoes⁶³ as it is more rigid and its outer diameter (20 nm) is twice the size of actin (10 nm), but has a lower maximum speed than actomyosin at approximately 1 $\mu\text{m/s}$. Conventional kinesin is processive and therefore one motor can transport a microtubule (with more binding sites than actin) for long distances before detaching⁶⁹. The actomyosin system has the advantages of high speed (up to 20 $\mu\text{m/s}$), allowing high throughput in future devices and high flexibility, enabling further miniaturization of devices⁶². The high flexibility of actin filaments can also be seen as a draw back in some applications where extremely precise control is required, and where fluctuations in the filament transport can lead to poor device performance. Utilizing the high speed of actin filaments with the stiffness and stability of microtubules would provide an ideal system for use in a variety of applications. In one demonstration of such a combination, the velocity of transport was low compared to actin filament gliding

on HMM⁷⁰. Alternatively, the possibility to use actin filament bundles to transport large cargo has been demonstrated, e.g. to transport *E. coli* cells and liposomes⁵⁹.

With over a decade of research, a high level of control over molecular motor systems is achievable. The most advanced demonstrations thus far have relied on microtubules to capture molecules from a bulk solution and/or the surface, and transport them to another region for detection^{12,18}. While some improvements in terms of, for example, speed of delivery, can be made, these types of devices reveal that molecular motors can be used in lab-on-a-chip applications (particularly for biosensing) see further Chapter 3.

Specific examples of advancements over time for molecular motor use in lab-on-a-chip applications are given in figure 2.3. Among these is the possibility to control the motility by surface patterning using selective chemistry⁵⁵ (Fig. 2.3a). Physical barriers made from polymer resists or SiO₂ have also been implemented for microtubule-kinesin^{2,71,72} or actomyosin^{1,73,74} active transport regions (Fig. 2.3a). Also, a combination of physical and chemical patterning can be used⁷⁵ (Fig. 2.3a). With further developments using overhanging roofs^{60,76} or enclosed channels⁷⁷, it is possible to reduce loss of actin and microtubules from guiding channels or structures during transport or capture (Fig.2.3a). The use of rectifiers^{2,78,79} (Fig. 2.3b), which can control or change the directionality of motion of cytoskeletal filaments, has been a critical development. Molecular concentrators have also been developed^{12,18,80} for capture and transport of very low concentration of analytes of high relevance for diagnostics, see figure 2.3c. While many of these techniques for creating physical barriers and rectifiers can be used for both molecular motor systems, restrictions, due to the need for narrow channels to maintain unidirectional guiding and minimum bending radius, must also be considered⁸¹. Further advances using thermally activated polymers³ (Fig. 2.3d), electrophoretic steering^{82,83}, or controlled release of ATP⁴ in order to sort or obtain a temporal control over microtubules, have also been presented. The use of more exotic substrates, such as HMM coated silicon nanowires⁸⁴, glass micron-sized wires⁸⁵, carbon nanotube networks⁸⁶ and recently carbon nanotubes⁸⁷ or graphene^{88,89} for *in vitro* motility gliding assays has also been developed, verifying that these molecular motors can operate on a wide variety of surfaces and geometries.

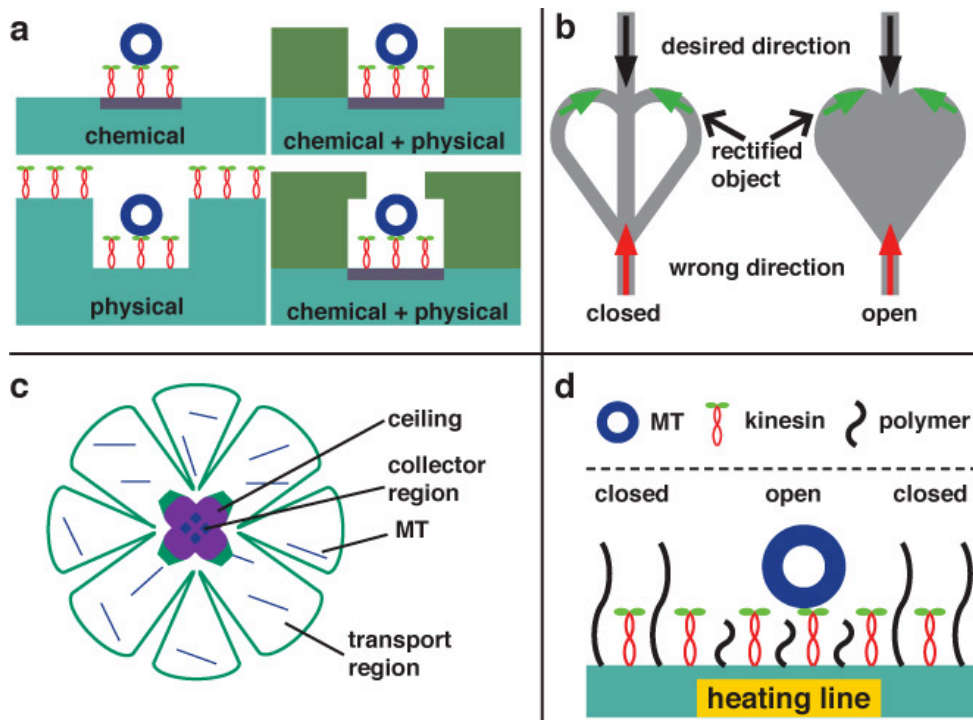


Figure 2.3. Molecular motor applications. a) Schematic of chemical (top left), physical (bottom left), and a combination of the two (top and bottom right), in order to guide motion of cytoskeletal filaments. Here, kinesin (red and green) transport microtubules (blue). Of these techniques, the use of selective chemical patterning and channels with overhanging roofs (bottom right) is the most effective at guiding and preventing escape of, e.g. microtubules. b) Rectifiers with closed loops (left) or open areas (right) connected to guiding channels are used to correct the motion of actin or microtubules. c) Microtubule-kinesin based device to transport and concentrate molecules attached to microtubules (MT), using a free standing ceiling for zero loss of MT from collector/detection region¹². d) Microtubule-kinesin (MT-kinesin) based demonstration of electrical steering with thermo-sensitive polymers as physical gates³.

2.3. Fabrication of nano-scale devices for *in vitro* motility assays

The ability to fabricate nano-scale devices for high-precision guidance of the actin filaments in an IVMA requires high-resolution techniques, such as electron beam lithography (EBL)⁶⁰ and nano-imprint lithography⁷⁴. Here, the fabrication of nanochannels is performed with EBL, capable of high precision (down to 10-20 nm resolution), but is limited in throughput. Scanning electron microscopy (SEM) is used to inspect these devices, post processing. A brief explanation of these two

techniques is first given below, followed by a general explanation of the fabrication process for a nano-scale device, see figure 2.4.

Electron beam lithography. The basic principle of EBL is as follows: electrons are generated from a source (either tungsten (W) or lanthanum hexaboride (LaB_6) crystal under high vacuum, $\sim 10^{-9}$ mBar) by inducing a high voltage bias (~ 10 -20 kV) over the source (the cathode). The ejected electrons are then focused into a narrow beam by electromagnetic lenses and scan coils (deflector plates), which work in series to adjust the shape and deflection of the beam. As the beam of electrons is focused towards the substrate, apertures with micrometer-sized openings are used to tune the size of the beam. All of the components are situated vertically inside of a column, which resides above the stage where the sample is placed in a high vacuum environment ($\sim 10^{-6}$ mBar). Overall, the stability of the system housing the electron source will determine the quality of the exposure, as weak sources, large drifts and poor control of the beam will greatly affect the outcome despite good control over other preparation methods.

EBL exposure. As the beam reaches the sample, it is capable of scanning over a very small area before the sample must be moved for further exposure. As the sample sits on a piezoelectric driven stage, high precision movements of the sample, coinciding with the previously exposed areas and un-exposed areas, is achievable. The parameters used for exposure are included in the following equation:

$$D = \frac{I \cdot t}{s^2} \quad (2.1)$$

where I is the current of the beam, typically on the order of 0.02 nA, t is the dwell time of the beam (often in ms), i.e. the time that the beam rests in one position before moving on, and s is the step size (range of tens of nm or less), equal in the x and y-directions. D is the dose (on the order of a few to a few hundreds of $\mu\text{C}/\text{cm}^2$), input by the user during exposure, and is generally set by guidelines according to the resist manufacturer or by carrying out a series of dose tests. Alternatively, single pixel lines or dots can be exposed, which require a one or zero dimensional step size input respectively.

EBL resists. We use an electron beam sensitive polymer resist as a mask, in order to write our intended pattern of channels or open areas onto substrate. Here we use polymethyl methacrylate (PMMA), a so-called positive resist for EBL. As the narrow (~ 10 nm in diameter) beam of electrons, scans over the surface of the resist, chains in the polymer begin to break, thus weakening the resist in the exposed regions. After exposure, in a process called development, these damaged areas are removed by a brief rinsing in solution. Other resists like hydrogen silsesquioxane (HSQ), can have opposite properties. These negative resists

become hardened, i.e. undergo cross-linking, during EBL exposure and remain after development. In order to control the fidelity of the pattern exposure with EBL, one must consider a number of variables which can influence the dose D , in equation 2.1, e.g. the resist used, thickness of resist and substrate, the substrate material, size of the aperture used, the accelerating voltage, and the pre- and post-exposure treatments, including baking time and temperature, development and finally ashing and etching if required.

Scanning electron microscopy. Verification of the size and shape of the nanostructures is often performed using scanning electron microscopy (SEM). Here the set-up is similar to that used in EBL but the stage is free to rotate and tilt such that cross-sectional views of the sample are more easily obtained. Prior to SEM, organic material, e.g. resist, must be coated with a metallic layer to make it conductive and to prevent significant damage and deformation due to charge up of electrons at the surface of the material. Typically a few nanometers of metal are sputtered onto the surface under low vacuum for SEM viewing. SEM imaging works by converting electrons (i.e. secondary electrons or backscattered electrons) generated from the surface of a conductive material into an image via a photo-detector. The number of electrons collected on the detector will influence the resolution of the image, therefore increasing the acceleration voltage can enhance the signal to noise ratio. However, too high accelerating voltages can cause damage to the surface. Therefore, only a few kV is used for viewing the resist-based nanostructures. For larger structures on the micrometer scale, optical microscopy is a suitable alternative for imaging the overall quality of the device.

Fabrication procedure. In this work we use actomyosin motility assays in flow cells, made from placing a glass slide beneath a nanostructured surface and flowing solutions through the cell by capillary force⁴⁸, as shown in figure 2.2b. The most simple of these surfaces (a single layer nanochannel) is schematically illustrated in figure 2.4. i) a Si substrate, with a thermally grown SiO₂ layer on top, is cleaned with isopropanol (IPA) and acetone to remove possible debris. The thickness of the oxide layer is typically a few hundred nanometers and can be adjusted depending on the application. Then, ii) a photosensitive resist is spin coated and baked on top of the sample. Here we use PMMA, but it can be replaced by any other electron beam sensitive (positive or negative) resist, according to the application. iii) After exposure, regions of damaged resist are removed (in the case of positive resists) with developers such as methyl isobutyl ketone (MIBK) and cleaned with IPA.

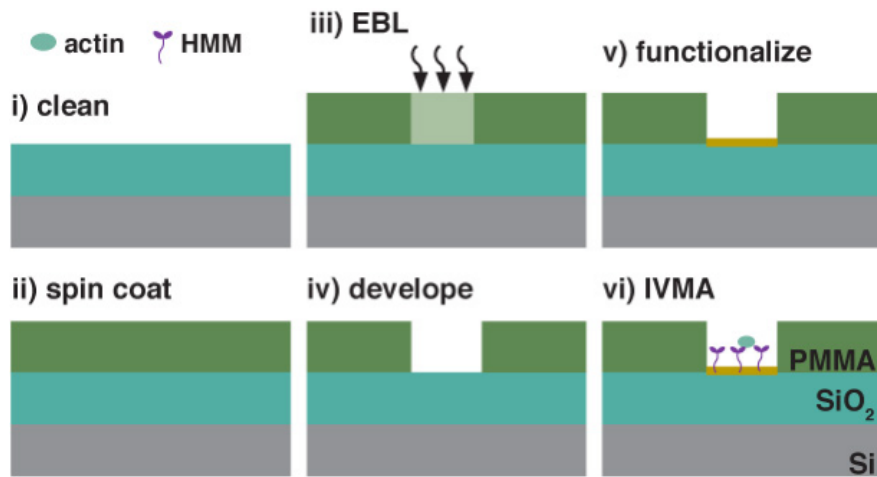


Figure 2.4. Schematic of single layer nanochannel fabrication. The substrate (SiO₂/Si) is i) cleaned and photoresist (PMMA) is ii) spin coated on top. iii) Then, the resist is exposed with EBL according to the desired pattern. iv) Next, the resist is developed and oxygen plasma ashing can be applied to remove resist residues in the channel. v) Finally, a chemical surface treatment can be performed to allow functional motility only in the preferred regions. vi) In an IVMA, HMM is adsorbed to the bottom of the nanochannel and actin filaments are propelled through the channel over them.

Plasma ashing. In order to remove possible residues of the resist layer in channels after development, the sample is subject to Plasma ashing for a brief time, typically 15 seconds. Plasma ashing is a technique, which uses microwaves to ionize oxygen gas in a vacuum and react with a substrate to remove residues of resist material. The sample is placed into a chamber (the microwave) and oxygen is pumped into the vacuumed chamber at a pressure of approximately 5 mbar. When the microwave is started, the oxygen gas becomes ionized and is drawn to the substrate where it reacts chemically with the resist material. At lower temperatures and short time scales (as in this case) the process is relatively gentle and does not damage the substrate. The ashing rate in this case is a few nanometers per tens of seconds.

Double-layer nanostructures. For a double-layer system, a layer of lift-off-resist (LOR) is spin coated onto the surface and baked prior to spin coating of PMMA. This LOR-layer is used for creating channels with slight overhanging edges (see Article I and IV) useful for filament guiding and confinement⁶⁰. These double layer systems are also important for metallization techniques where metal contacts are required (see Article IV and V). For IVMA tests, however, LOR was omitted where possible, as this layer often contributed to a large background fluorescence signal (see Article I and III).

IVMA preparation. Prior to use in IVMA the surfaces must be treated with a chemical in a functionalization process (Fig. 2.4) in order achieve proper

absorption of molecular motors to the intended regions and channels. Most of surfaces described in this thesis are treated with trimethyl chlorosilane (TMCS), in a chemical vapor deposition (CVD) process. Silanization takes place in an inert environment, i.e. under nitrogen flow in a glove box where O₂ and H₂O levels are sub parts per million. TMCS adheres specifically to SiO₂ surfaces and creates a moderately hydrophobic layer to which the HMM can bind by their tail end⁹⁰ and thus maintain functionality, i.e. can transport actin filaments^{61,73}. Finally, wetting of the channels can be performed, by steaming of the surfaces for short times (less than 1 min), in order to prevent air bubbles from forming in the structures just prior to the IVMA⁶⁰.

3. Biosensing with molecular motors

Molecular motors have been proposed as biosensors due to their ability to achieve active transport as opposed to passive, diffusion-based transport, without the need for pressure-driven flow^{62,64}. Recent demonstrations with microtubules and kinesin^{12,18}, however, are slow compared to other techniques^{91,92}. Here we demonstrate the use of faster and more flexible myosin molecular motors and actin filaments in order to reduce the detection time and further reduce the size of the device, respectively.

In a broad definition a biosensor is a device that incorporates biological recognition elements, such as antibodies or oligonucleotides, and detects, by optical, electrical, or electrochemical means, a target analyte (e.g. antigen, DNA, enzyme). The main challenge is to amplify the signal of the target molecule, which is often low due to low sample concentrations, with respect to that of the bulk volume. Relevant analyte concentration is typically in the femto molar (fM) range¹⁶, i.e. a few thousand or hundred molecules per mL or μL , respectively. It is therefore necessary to increase the amount of the target analyte at the detection site, or reduce the detection area in order to increase the signal to noise ratio. If the detection site is reduced, the transport time of target analyte to the detector should also be increased, this is possible e.g. through directed, rather than diffusion-limited transport¹⁶. Therefore, molecular motors offer a significant advantage, due to their ability to actively transport molecules⁵.

Within the field of molecular-motor based biosensors, the most common technique is to use conjugation chemistry in an enzyme-linked immunosorbent assay⁹³ (ELISA), so-called sandwich assays. Here an antibody or linker molecule (e.g. biotin) is attached to microtubules^{4,65,68,94,95} or actin filaments^{56,96,97} and the fluorescently labeled antigen is captured from solution, from specific loading stations⁹⁸ or in a pre-incubation step⁹⁹. Through molecular motor propulsion, the target molecule can then be transported to a detection region, where the fluorescence signal of the labeled antigen (or loaded molecule, e.g. streptavidin, quantum dot or liposome) is read out optically.

The transport of analyte molecules can be from a larger open area, to a central location^{12,13,17}, or, as was demonstrated in one device, along the edge of the large open area¹⁸. The limit of detection achieved was shown, for one microtubule-

kinesin system evaluated, to be on the range of fM to nM¹². However, the use of large open regions and detection sites, used in microtubule-kinesin based devices, can be seen as a draw back, as further miniaturization would allow for an increase in the number of detection sites per device, thus increasing reliability in readout. Here we use myosin motors (specifically HMM) to transport labeled actin filaments in a concentration mechanism. We show that the time required for concentration and the total active device area is much faster and smaller, respectively, than previous molecular motor devices, primarily due to the high speed (up to 10 $\mu\text{m/s}$) and flexibility for actomyosin. We also use oxide-coated nanowires as fluorescence read-out detectors. Here, the fluorescence signal from actin filaments, transported by myosin motors along nanowires, is guided to the tip of the nanowire, where it is read out. This construct enables enhanced signal-to-noise ratio due to the high surface area to volume ratio of the nanowire detectors.

3.1. Molecular detection by concentration

Within the context of molecular concentration with actomyosin, two primary challenges are considered in the device design: i) the ability to concentrate analyte molecules at a high rate and ii) the ability to detect very low concentrations of analyte from the bulk solution. First, we use the guiding effect of sloped walls^{13,53} to concentrate filaments to the detector. Second, we rely on miniaturized collector/detector regions (trapping zones, TZ), which are much smaller than the transport areas (loading zones, LZ) where actin filaments are initially bound.

3.1.1. First-generation device

In a first-generation device, the loading zones (area $\approx 34 \times 40 \mu\text{m}^2$) were designed to collect filaments from the solution and to direct them⁵⁸ to the trapping zones (area $\approx 11 \times 11 \mu\text{m}^2$) via nanochannels, of approximately 250 nm width at their base, see figure 3.1a. We placed heart-shaped rectifiers along the length of the nanochannels to prevent filaments from escaping back into the LZs. For each nanochannel, we placed three rectifiers in series, with radius of curvature = 3 μm , resulting in high cumulative rectifying efficiencies of approximately 96%. We also assigned control loading-zones (CTR-LZ), which were not connected to the TZ, in order to correct for photo-bleaching in LZ and TZ. Whereas, in a fully realized device, all LZs would be connected. The entire structure was made using EBL applied to a double layer of resist (PMMA on LOR, see Ch. 2.3 and Article I, for further information on fabrication details).

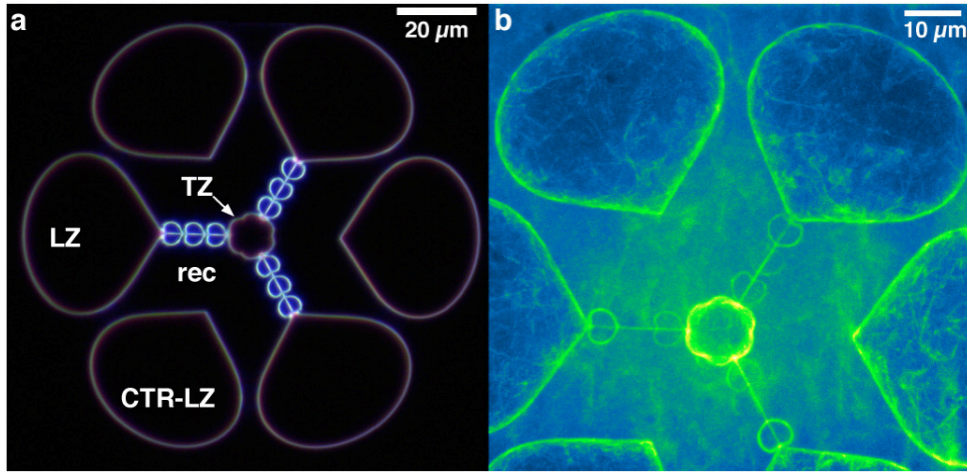


Figure 3.1: Molecular concentrator. a) Dark field optical micrograph of concentrator structure, with components labeled. Myosin motors propel actin filaments across the surface of large open areas of loading zones (LZ). The LZ configuration allows actin to be concentrated (via nanochannels) towards the central area or trapping zone (TZ) where they are confined. Rectifiers (rec) are aligned along the nanochannels to create uni-directional guiding in the case where filaments may escape from the TZ. Non-connected regions or control loading zones (CTR-LZ) were used as control areas, to which the fluorescence signal of the LZ and TZ could be compared. b) Z-stack (maximum projection) of fluorescence micrographs during motility assay. Color coding for clarity. Time span is approximately 5 min in total after addition of ATP to the flow cell.

In this device, actin filaments accumulate, from solution, at the loading zones. Once ATP is added, actin filaments are transported to the detector regions where they are trapped, figure 3.1b. The fluorescence signal of the detector region (TZ) increases with time, while that of the transport regions (LZ) decreases. Here, we would like to quantify the rate accumulation of filaments at the TZ, and also to know if all of the filaments transported from the LZs were arriving at the TZ, and contributing to the increased fluorescence signal, i.e. not lost due to, e.g. escape. This is important when considering the limit of detection achievable in this device. We, therefore, first examined the rate of decay of the fluorescence signal at the LZs, i.e. filaments exiting the LZs, in order to determine the expected rate and maximal increase in the TZ.

After addition of ATP, the rate of fluorescence decay can be estimated according to the following equation:

$$I(t) = I_0 * f * \exp(-k_+t) + B \quad (3.1)$$

where I_0 is the initial fluorescence intensity, f is the fraction of motile filaments, k_+ is the decay constant, and B is the background signal. Experimental data from a single LZ, and theoretical fit according to equation 3.1, are plotted in figure 3.2.

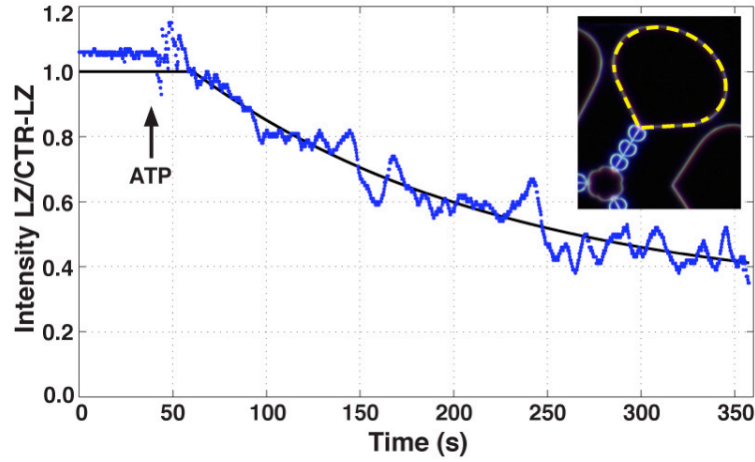


Figure 3.2: LZ depletion over time. Total fluorescence intensity of the background-subtracted ratio of the LZ (yellow dashed line, inset) and CTR-LZ over 6 min recording time. Black arrow indicates addition of ATP. Data is normalized to the readjustment time for maintaining focus after ATP addition. Black curve indicates fit of data from readjustment time, $t = 60$ s, according to equation 3.

The fluorescence signal of the TZ increased by a factor of about 2.6, 1 min after addition of ATP (Fig. 3.3a). At 5 min after ATP addition, the fluorescence intensity ratio reached a value of approximately 3.4. The theoretically predicted average filament density ratio at steady-state (C_{ss}^T) and time zero (C_i) is given by:

$$\frac{C_{ss}^T}{C_i} \approx \frac{k_+ * f}{(k_+ + k_-)} \left(\frac{A_L}{A_T} + 1 \right) \quad (3.2)$$

where k_+ and k_- are the rate constants for emptying and filling in the LZ and TZ respectively. The ratio of the area of the LZ and TZ is given by A_L and A_T and f is the fraction of motile filaments in the LZ. According to the rate of emptying in the LZ connected to the TZ, and equation 3.2, we expected the ratio of fluorescence intensity of the TZ/CTR-LZ to be approximately 2.5 times higher than the experimental observation 5 min after ATP addition, see figure 3.3b.

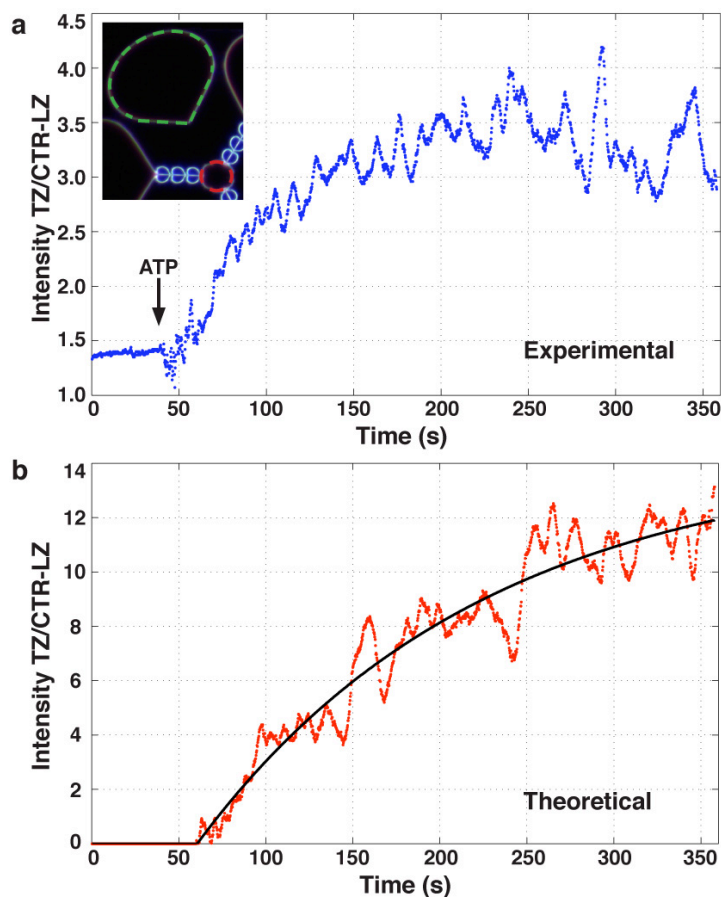


Figure 3.3: Concentration over time. a) Background subtracted ratio of the total area of the TZ (red dashed line, inset) to one CTR-LZ (green dashed line, inset). Black arrow indicates addition of ATP. The readjustment time for maintaining focus after ATP addition was approximately 20 s. Fluctuation in the intensity data are indicative of filament escape from the TZ, likely due to overcrowding. b) Theoretical increase in concentration ratio for TZ over CTR-LZ, modeled fit from equation 3.2 and data in Figure 3.2.

Concluding remarks. We were able to increase the signal to noise ratio at the TZ by a factor of 3 with accumulation of fluorescently tagged actin filaments 2 min after ATP addition (see Fig. 3.3a). Here we reduced the transport areas, i.e. the initial regions of capture (from a previously reported device¹² by a factor of 3.1) and the detection region (by a factor of 3) in order to reduce the overall footprint of the devices. However, the performance of the concentration device was not as theoretically predicted. From equation 3.2, and the rate of decrease in the loading zone, we expected an increase in the fluorescence signal at the trapping zone to be approximately 10 times higher than the experiment result at steady state.

In the CTR-LZs filaments were able to escape at the sharp vertex and therefore contributed to a larger background signal due to filaments floating in solution. Several filaments escaped from the TZ as the density of filaments increased, and on occasion, the overcrowding caused filaments to escape back up through the nanochannels to the LZs. The LOR layer used in the double resist layer design contributed to a large background fluorescence signal. From our observations, we could see that the maximal signal was found in a region of approximately 1 μm from the edge of the TZ. In order to improve the device, therefore, the TZ area should be directly reduced further into a ring-like object⁵⁸. Alternatively, detectors could be positioned in this region in order to selectively retrieve information at the detection site, for example in the use of magnetic particles for analyte pre-separation⁹⁹. Considering these issues, we revised the structure of the loading regions, nanochannels and trapping zone as a way to further increase the effectiveness of the concentration technique based on myosin propelled actin filaments. We also relied on Monte Carlo simulations to aid in the optimized design of the loading zones, to provide faster enrichment at the TZ area, details are given in Article I.

3.1.2. Second-generation device

On basis of the above considerations, a second-generation device was developed, where we modified both the loading zones and the trapping zone. We also removed rectifiers, as the new TZ design was self-rectifying, see figure 3.4a. Here, the CTR-LZs were also modified with small rings (radius = 1 μm), in order to prevent filament detachment at sharp intersections⁵⁸, see figure 3.4b. The resulting concentration device was markedly more effective, in that the signal-to-noise ratio from the TZ dramatically increased (Fig. 3.4c). We also omitted the LOR layer, in order to reduce background fluorescence. However, due to this omission, there were no over-hanging roofs, and over-crowding in the TZ lead to detachment of filaments.

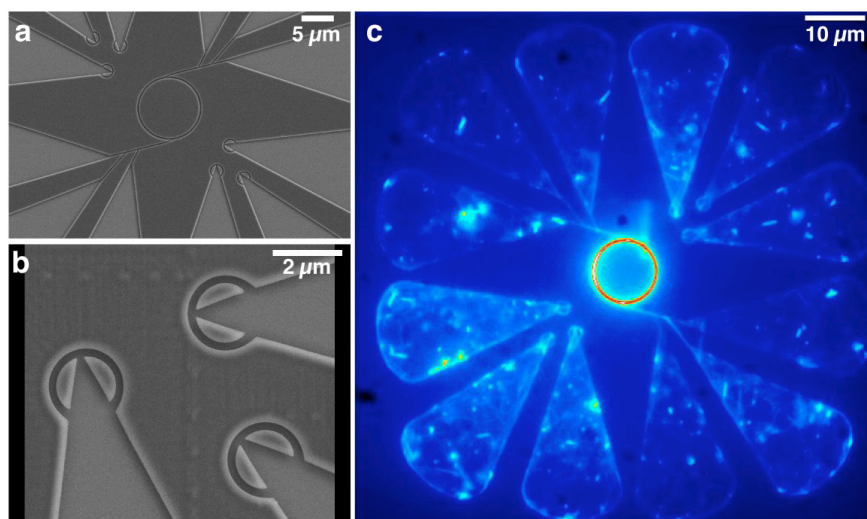


Figure 3.4: Scanning electron micrographs and fluorescence micrograph of second-generation molecular concentrator. a) SEM close-up of detection region connected to loading zones via nanochannels. b) SEM close up of non-connected loading zones. Rings are placed at the vertices to prevent filament loss due to sharp angle approach. Surfaces are coated with 5 nm Pt prior to SEM viewing. c) Z-stack (average projection) of fluorescence micrographs (1 min time span) of molecular concentrator, after ATP addition. The optimized geometrical configuration allows actin to be concentrated (via nanochannels) at a high rate towards the central ring where they become trapped without the use of rectifiers.

Figure 3.5 shows an example of the fluorescence intensity in the TZ for the first three minutes of recording in one device. Here, we see that the increase of the fluorescence signal of the TZ was enhanced by a factor of 4 above that of the first generation device in the first two minutes. This rapid increase in fluorescence stabilized quickly. From the same theoretical predictions used in the first-generation device, we estimated an expected increase of fluorescence intensity at the TZ to be 7 times higher than the experimental average. This lower than expected signal was likely due to the absence of overhanging roofs on the TZ, thus also causing the fluorescence signal to fluctuate and decay slightly over time. The use of ceilings¹² would prevent filament escape and rapid overcrowding, which lead to ejection of filaments from the TZ or escape back up through the nanochannels into the LZs. The use of rings at the vertices of the CTR-LZs did prevent, to a large extent, the loss of filaments from these regions. However, again due to the lack of roofs, some filaments escaped in these areas as well.

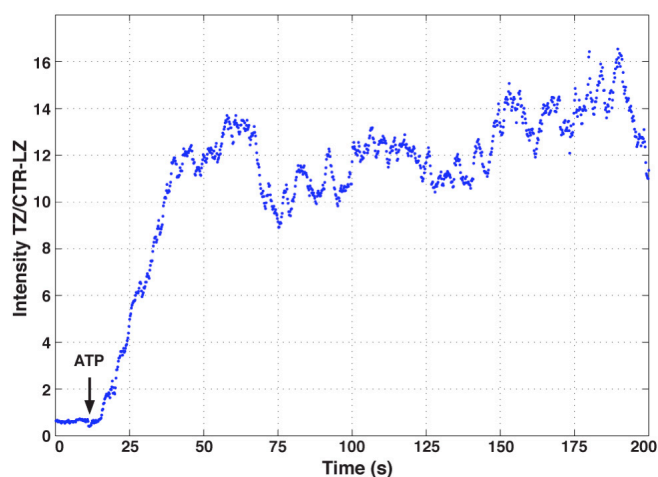


Figure 3.5: Concentration over time for second-generation device. Ratio of background-subtracted fluorescence in TZ to average of three CTR-LZs over 3.3 min. Black arrow indicates addition of ATP. The concentration rate for the device was approximately twice as fast as for the first generation device. Several spikes in the intensity data are indicative of filament escape from the TZ, due to overcrowding.

3.1.3. Future directions

There was a measureable improvement in the two critical features (rate of concentration and S/N) of a molecular-motor based biosensor, between the first- and second-generation devices and to previously demonstrated devices. First, the rate of concentration was approximately twice as fast from the first to the second-generation device, meaning that the time required for observation could be greatly reduced when investigating multiple devices on a chip. This rate in the second-generation device was an order of magnitude faster than a correspondingly similar demonstration with microtubules and kinesin motors¹². Secondly, the signal-to-noise ratio improved by a factor of 4 in the transition from the first generation device to the second. Here, the theoretical prediction for the increase in signal-to-noise for both devices was much higher than the experimental results, likely due to the problems described in device performance, in particular to filament loss in the detection regions due to over-crowding.

While the reduction of the TZ improved the signal-to-noise ratio in this second-generation device, the restricted number of filaments allowed in this area prevented stable accumulation. It would therefore be interesting to employ similar roof like structures as shown in previous devices¹² in order to capture all filaments entering to the detection site. Alternatively, one could build up the walls of the device, making it more difficult for filaments to escape; however, it is likely that a slightly overhanging roof⁶⁰ would still be required. It should also be noted that

recording of multiple devices on a chip is possible, with minimal loss of filaments, if for example, an ATP-free solution is added to the flow cell inducing a rigor state in the HMM motors subsequent to completed concentration of filaments in the TZ. If the rate of transport is as fast as shown in the second-generation device, then the bulk of the filaments carrying cargo would have arrived at the TZ within one to two minutes, before being halted. By shutting off the transport, a chip patterned with potentially thousands of devices within one square millimeter area could be monitored and recorded in a few hours time.

3.2. Nanowires for molecular detection

Due to their small size and high surface-area-to-volume ratio, nanowires are ideal surfaces for molecular sensing, and have been shown to achieve a very low level of detection in the sub-femto molar range^{100,101}, with correspondingly high signal-to-noise ratios. Nanowires used as biosensors represent a growing field in the areas of intracellular monitoring^{102,103}, studies of cell activity¹⁰⁴⁻¹⁰⁶ and molecular sensing¹⁰⁷⁻¹⁰⁹. These techniques typically operate by sensing a change in conductivity in the wire, instead of a fluorescence signal, and are therefore referred to as “label-free”. These types of devices, while reportedly highly sensitive, only interpret change in conductance as an event, and cannot specifically identify if the analyte is bound to the surface of the nanowire without using fluorescent probes to check. These devices are also limited, in the number of individual wires addressable on a single chip^{110,111}. Here we demonstrate the use of vertical, freestanding nanowires as molecular detectors based on their light-guiding properties. With the actomyosin molecular motor system, we can directly correlate an event (analyte recognition) with the motion of the actin filaments moving up or down the nanowires. In this configuration, potentially hundreds of thousands or millions of individual nanowire detectors can be accessible on a single chip, thus offering the potential for a higher level of multiplexing and increasing reliability in read-out.

Nanowire field effect transistors. Existing nanowire biosensors operate as three terminal field effect transistors (FET). The nanowire serves as the conducting channel, and is typically doped with boron or phosphorus¹¹². The nanowires are often functionalized with selective surface modifications, i.e. chemical or biological linkers (receptors). Detection of analyte is read out by a change in nanowire conductivity, induced by accumulation of target molecules at the surface of the nanowire, arriving from the bulk solution.

Challenges in NanowireFETs. Many challenges are encountered in the development of bio-nanoFETs; three such examples are listed here. One example

is the difficulty in correlating an electrical readout with a particular event at low analyte concentrations, due to low signal to noise ratio and lack of information in label-free approaches¹¹². Operation of devices in the sub-threshold regime when the carrier (dopant) concentration is low, such that accumulation of molecules yields a non-linear response in the conductance, can improve the signal to noise ratio and limit of detection¹¹³. A second challenge is the ability to operate under biologically relevant conditions, due to e.g. dampened signal strength or electrical screening of charge. Aside from operating in a sub-threshold regime¹¹³, the use of a metal-oxide shell has recently been shown to improve long term stability of devices in a physiological model solution¹¹⁴. Finally, analyte transport limitation, i.e. slow transport of a low concentration of molecules to the detection site, hinders rapid detection of probes¹⁶. This third limitation is relevant for nanowireFET design, regardless of the fabrication method, i.e. top down versus bottom up¹¹⁵. Most commonly, the nanowire is horizontal on a surface and the target molecules are delivered by diffusion-limited transport to the nanowire sensor from microfluidic channels. The flow into these channels can be pressure driven flow over the nanowire, however, molecules must be able to diffuse down to the surface, or static without any external pumping of solution¹⁰⁹. This limitation can be overcome, however, by active solution exchange above the nanowireFET with controlled mixing¹¹⁶ in order to reduce response time.

Nanowires as light-guides. Here, we rely on an optical read-out method that allows for direct observation of the sensing platform. By employing vertical nanowires, we make use of their total surface area, allowing many molecules to attach all around the wire at once and thus increase the signal-to-noise ratio. With the use of actomyosin, we can directly follow an event (fluorescent probes at the surface), when an actin filament travels up or down a nanowire. Both the core material, gallium phosphide (GaP) semiconductor nanowires, and the shell, Al₂O₃ act as bio-benign surfaces^{117,118}, important for biological applications. We observe that light emitted from fluorescent probes, attached to filaments moving along the length of the wire, is emitted from the wire tip. By focusing on the top of the nanowires, we can collect the fluorescence signal from all wires (in one field of view) at once. We predict that the nanowires act as light-guides for the labeled actin filaments moving along the length of the wire, and discuss this possibility in terms of material properties and optical configurations. Figure 3.6 provides a schematic representation of the set-up of our nanowires with actin filaments and HMM.

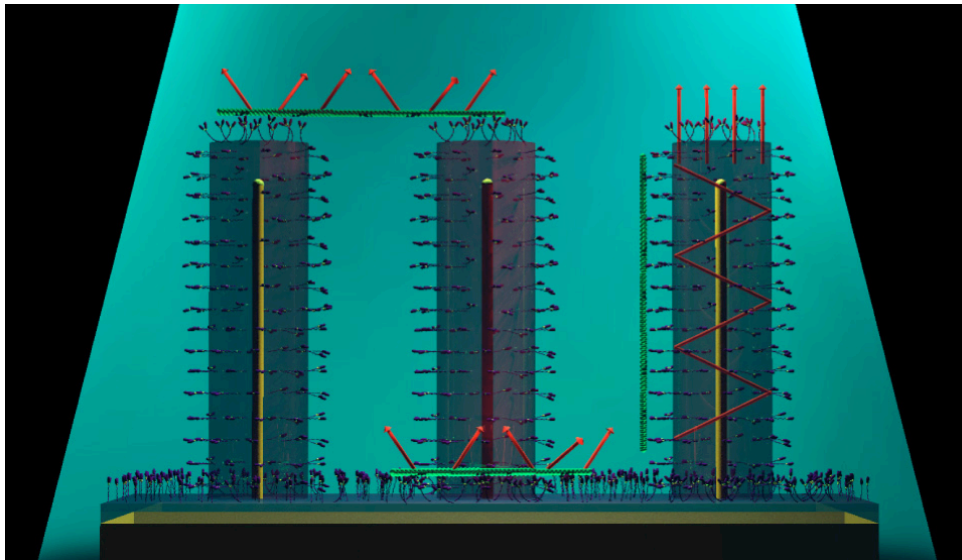


Figure 3.6: Schematic of actomyosin on nanowire arrays used for light guiding. Fluorescently labeled actin filaments can be detected moving on the surface of Al_2O_3 coated GaP and on top of the nanowires. As the filaments travel vertically along the wires the Al_2O_3 shell acts as a light-guide such that the fluorescence emission from the filaments is enhanced and detected locally at the tip of the nanowires.

Nanowire fabrication. In order to fabricate these structures, we use a standard bottom-up lithographic approach¹¹⁹, shown in figure 3.7. Briefly, the GaP substrate is coated with resist (e.g. PMMA or ZEP) and EBL is used to expose the pattern of dots into the resist, figure 3.7a-b. The sample is then immersed in developer solution in order to remove the exposed resist and placed into an evaporator where a thin film of Au (~ 20 nm) is deposited on the surface, figure 3.7c. After lift off of the resist and unwanted Au, only the Au particles remain, figure 3.7d. The sample is placed in a growth chamber, and wires are grown by Au particle assisted vapor liquid solid growth, with metal organic vapor phase epitaxy (MOVPE)^{120,121}, figure 3.7e, see details below. After the samples are removed from the growth chamber, they are coated with Al_2O_3 in an atomic layer deposition (ALD) process, figure 3.7f. In ALD, samples are placed in a growth chamber, and the substrate is heated to 250 °C. Alternating cycles of water and trimethylaluminum (TMAI) are introduced to the sample chamber and flow parallel to the surface. The duration of gas pulses is ~ 15 ms. For each cycle of H_2O and TMAI, a monolayer of Al_2O_3 is formed. Here we typically run 600 complete cycles yielding an approximately 60 nm thick layer of oxide material.

Nanowire growth. The nanowire growth process, while highly sophisticated¹²¹, can be explained in a few steps. 1) The GaP substrate is placed on a rotating disk (susceptor) inside a glass growth chamber and heated to, e.g. 470 °C. In order to

avoid surface decomposition, the precursor material, phosphine gas (PH_3 ; molar fraction $\sim 1.2 \cdot 10^{-1}$), is simultaneously supplied to the growth chamber via carrier gas (H_2) with a flow of $\sim 6 \text{ l min}^{-1}$. This annealing step is required to remove surface oxide, and to allow the Au nanoparticles to form an alloy on the surface (i.e. in a liquid phase) with the growth material¹²². 2) The precursor material, trimethyl gallium (TMGa; molar fraction $\sim 4.3 \cdot 10^{-4}$), is then added. 3) As the material accumulates in the Au droplet it becomes supersaturated and nucleation occurs below the droplet¹²². Once this nucleation occurs, a GaP layer is formed at the interface and the process continues as long as the Au particle is supersaturated¹²². 4) Growth is halted by switching off the gases, once the desired length is achieved, and the substrate is allowed to cool down. Typical growth rates, under these conditions, are on the order of $1 \mu\text{m}$ per minute or less. Our substrate, with (111)B crystal orientation, is used in order to achieve nanowire growth perpendicular to the surface¹²¹.

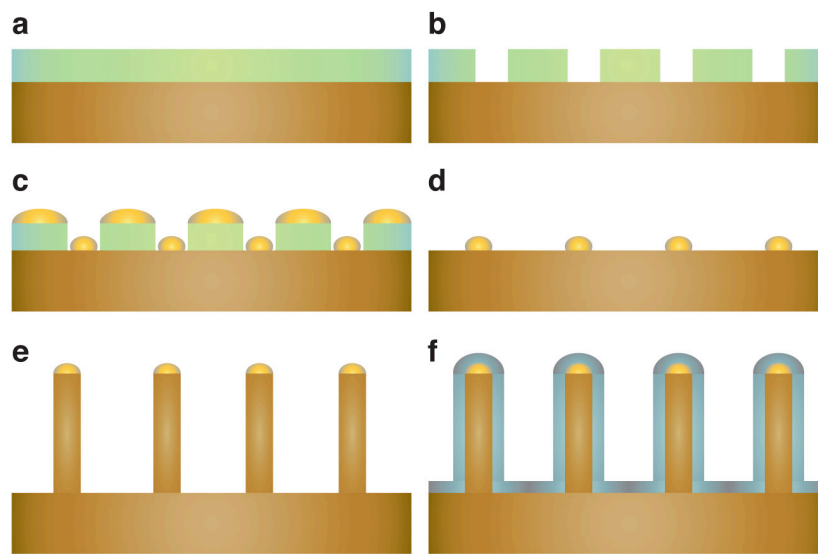


Figure 3.7: Schematic of fabrication of nanowire arrays. a) Resist is spun on the surface of the GaP sample. b) Electron beam lithography is used to expose dots in an array pattern and the sample is developed in order to remove exposed resist. c) Au is deposited on the surface of the sample. d) The unwanted Au is removed from the surface leaving only the Au particles required for growth. e) The samples are placed in a reactor and grown using metal organic vapor phase epitaxy. f) Al_2O_3 is coated on top of the nanowires in an atomic layer deposition process.

Nanowires for guiding actomyosin. Initially, we were motivated by the possibility to use arrays of nanowires for guiding of actin filaments at the surface e.g. at the bottom of the nanowires. This type of guiding was previously demonstrated for rectification of axons extending from neural cells¹²³. As the uni-directional guiding of actin filaments has been shown in nanochannels to be limited to a width

of approximately 300 nm⁶⁰, we decided to place this as our upper limit in nanowire spacing, see for example figure 3.8a. We evaluated the performance of these nanowires in a standard IVMA. Here we used actin filaments, fluorescently labeled with APh. Due to high background fluorescence in the TRITC filter, we did not use RhPh labeling. In these assays, we could see transport of actin filaments along the surface of the substrate and along the top of the nanowire arrays. We could not identify filaments moving between wires on the surface and therefore increased the spacing between wires in order to improve the localization.

In this step we included a variety of nanowire designs in order to investigate further, the guiding on top or potentially on the bottom of the wires, see figure 3.8. Among these designs, we aimed to achieve a concentrating effect, whereby filaments could enter at the top of a dense array and be guided by a meandering path of wires to a circular array and become trapped, see figure 3.8a-b. This guiding effect, was not successful, however, as filaments would be guided on top of the pattern from multiple access points and did not adhere to a specific path or directionality, figure 3.8d. In another configuration, we aligned a straight row of wires to a large inwardly spiraling structure, in order to observe the cut off radius for guiding, figure 3.8c,e. This attempt was also unsuccessful, as filaments could climb onto the structure at multiple points and even connect across large gaps in the spiral. Here we saw that filaments spent a similar amount of time on the wires, regardless of the radius of curvature of the structures, and that the movement was sporadic and random, i.e. without any directionality defined by the nanowire array.

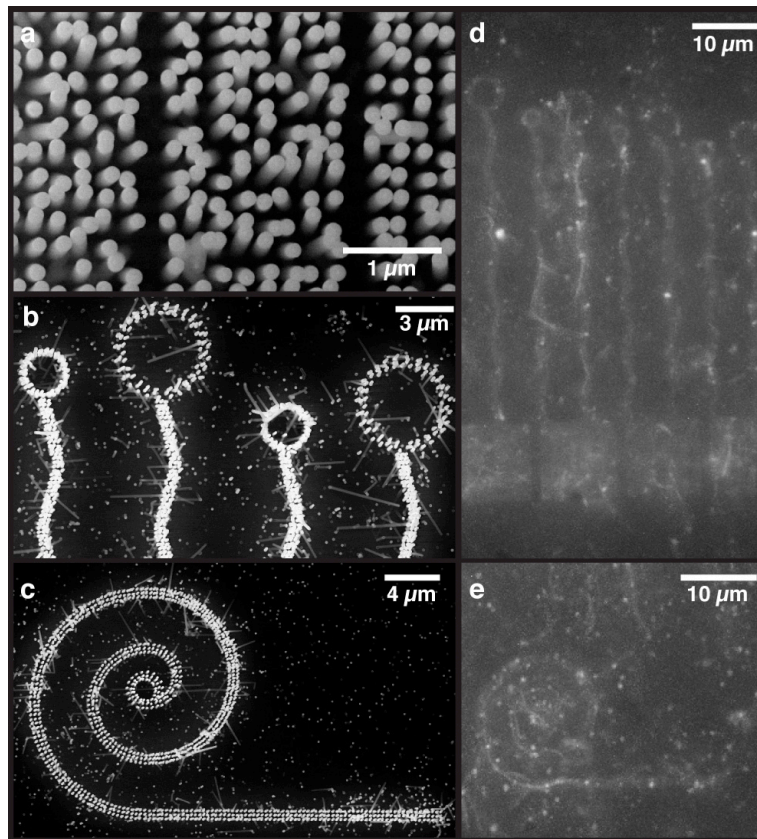


Figure 3.8: SEM and fluorescence images of nanowire designs for actin filament guiding. a) Dense arrays of wires, with approximately 200 nm spacing, intended to act as a guiding channel between wires. b) Meandering arrays of wires connected to circular arrays of varying diameters on one end and to dense arrays, as in panel a, on the other end. c) Circular arrays of wires in an outwardly spiraling configuration connected to a straight array of nanowires. d) Maximum projection of meandering arrays connected to dense patterns (as in panel a and b). Fluorescence micrographs integrated during a time span of 1 min. Filaments moving in both upward and downward directions. Occasionally filaments span the gap between structures. e) Maximum projection of spiraling array, integrated over 1.8 min. Narrow arrays in b and c are composed of three nanowires across the width.

Nanowires as light-guides. The final array of wires tested included wires aligned in sparse arrays, with 1 μm square spacing and 5 μm length, shown in figure 3.9a. In these arrays, filaments tended to spend the same time on top of the wires as in the other structures, but we also noticed another phenomenon. We observed blinking wires in arrays with 1 μm inter-wire spacing, see figure 3.9b. This observation led us to believe that the fluorescence emission of filaments, moving up or down the wires, was guided and emitted at the tip of the wire.

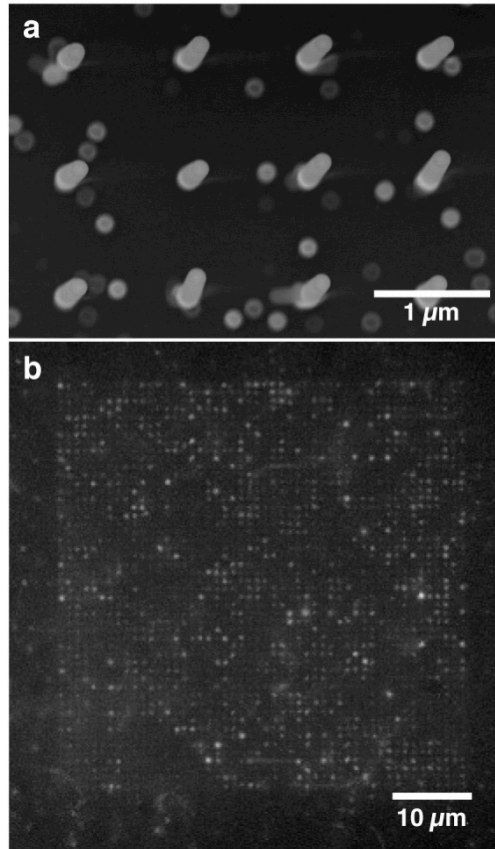


Figure 3.9: SEM and fluorescence images of nanowire designs. a) SEM image of sparse arrays of wires, with approximately 1 μm spacing. b) Maximum projection over 46 s of nanowire array in IVMA. Filaments are seen gliding across the tops of nanowires. Bright points indicate filaments moving up or down nanowires. Nanowire length = 5 μm . Figure modified from Article II.

In order to quantify the emitted fluorescence at the tip of the wires, we compared the intensity of an outstretched filament moving horizontally over the array to its' intensity while moving vertically down a nanowire. The ratio of the vertical versus horizontal intensity is plotted in figure 3.10a. We can see that longer filaments tend to have higher intensity ratios, which may be related to the focal depth, in the likelihood that light is simply collected from a larger portion of the wire, rather than just the tip. In order to rule out the possibility that light intensity at the tip of the wire could be due to a large collection depth along the wire, we estimated the depth of focus according to the following relationship:

$$\delta = \frac{\lambda \cdot n}{NA} + \frac{n}{M \cdot NA} d \quad (3.3)$$

where $\lambda \approx 490$ nm is the excitation wavelength, $n = 1.52$, is the index of refraction for the oil immersion objective, with a magnification of $M = 100X$, and numerical aperture of $NA = 1.4$. The pixel size of the camera is $d = 0.165$ μm , giving a depth of focus ~ 0.5 μm . This is only a fraction of the 5 μm long wires used here. Therefore, we would not expect that the light from the filament is simply recorded along the full length of the wire. This short depth of focus is also not expected to contribute to differences between long and short filament intensity ratios shown in figure 3.10a, as the shortest filament observed was longer than 1 μm . To further confirm the limited depth of focus, we compare the fluorescence intensity of a filament, which is stationary, vertically along a nanowire, to a filament that is stationary horizontally on the substrate (at the bottom of the nanowire array). The region of interest (ROI) in both cases is a 3×3 pixel² area. During the same time course we collect the fluorescence intensity in each ROI when focusing at the top and bottom of the sample, see figure 3.10b. From these curves, we can see that the fluorescence intensity emitted at the nanowire tip does not contribute to the fluorescence signal when focusing on the surface, at the bottom of the nanowires. We also do not see a contribution in fluorescence from the stationary filament, at the bottom of the nanowires, when focus is at the top of the nanowires. This information further supports our prediction that the GaP nanowires coated with an Al_2O_3 shell act as optical waveguides for light emitted from fluorescently labeled actin filaments, moving vertically along the nanowires.

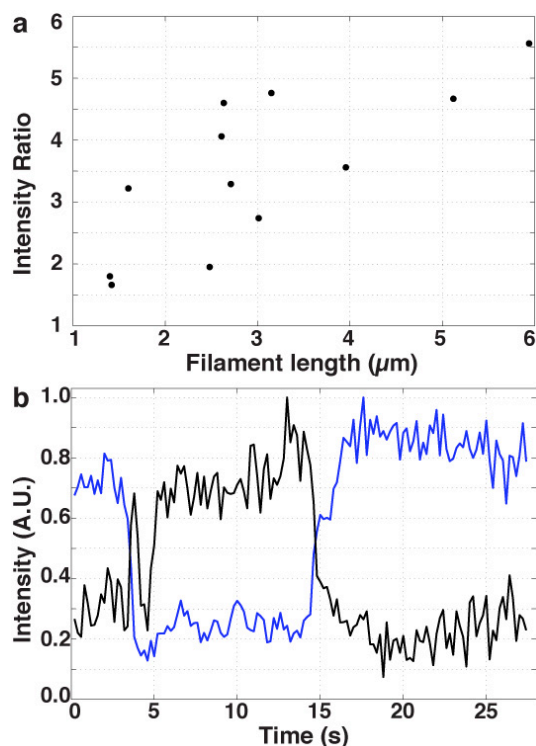


Figure 3.10: Intensity ratio and measured fluorescence comparison. a) Background-subtracted fluorescence intensity ratio of filaments moving horizontally along the tops of nanowires versus filaments moving vertically along wires. Region of interest (ROI) is 3×3 pixel² area centered at the filaments' brightest point (center or ends) and centered at the tip of the nanowire. b) Background subtracted and normalized fluorescence intensity in 3×3 pixel² ROI: centered at nanowire tip with stationary filament attached vertically along nanowire (blue curve) and on a stationary filament attached on the sample's surface just outside the array (black curve). For first 3.4 s and from ~15 s the camera is focused on the tips of the nanowires, while at 3.8-14 s the camera is focused on the bottom of the wires at the sample's surface.

Light-guiding mechanism. Due to the limited depth of focus of imaging during motility and the measured comparison of filaments in figure 3.10b, we can say for certain that the fluorescence intensity of a filament moving vertically along a wire is not fully detectable under normal imaging mode. Therefore, we conclude that a light-guiding effect is occurring as filaments are traveling vertically down or up nanowires. While this effect is not fully theoretically described within this work, we predict that the mechanism is most likely due to total internal reflection of a portion of the light emitted, from fluorophores on the actin filament. Total internal reflection is achieved when light travelling from a medium of a given refractive index to a medium of lower refractive index is incident at or above a minimum critical angle according to the following equation:

$$\theta_c = \sin^{-1} \left(\frac{n_2}{n_1} \right) \quad (3.4).$$

Here, n_i is the refractive index of the medium and θ_c , is the minimum angle from the normal, at which light is totally internally reflected. This value is $\sim 28.3^\circ$ and $\sim 51.5^\circ$, for the GaP-Al₂O₃ and the Al₂O₃-H₂O boundaries respectively. The incident light (emitted from excited fluorophores on the actin filaments) should therefore be partially internally reflected in the boundary of the GaP core and the Al₂O₃ shell, and from the Al₂O₃ shell to the surrounding medium to a lesser degree, due to a more dramatic change in the refractive indices of the core-shell material than the shell and surrounding medium. The light is thereby guided along and emitted at the tip of the nanowire, enabling our oxide coated semiconductor nanowires to act as wave guides^{124,125}.

3.2.1. Future applications

As a basis for future applications of these devices, it is highly relevant to perform theoretical modeling of the nanowire arrays to determine the in-coupling of light and wave propagation along the wires¹²⁶. In this way information about the core semiconductor material, the diameter of the core, the thickness of the oxide shell and the material used, as well as spacing, and lengths of the nanowires are important parameters to consider, as well as determining the ideal excitation and emission wavelengths for optimal light-guiding¹²⁷. It has been shown that metal-oxide nanoribbons also function as light-guides¹²⁵. By implementing alternative fabrication techniques, such as top-down etching, metal-oxide nanowires can also be created, thus eliminating the need for expensive growth substrates and growth techniques, which could reduce cost in device development.

Another potential route, would be to use axial heterostructure nanowires previously demonstrated as a bio-barcoding platform¹²⁸. These nanowires contain fluorescent segments, which, in our set up, could be used to locally excite fluorescent probes at specific locations along the nanowire. This local excitation can also be combined with other fluorescent techniques, such as fluorescence resonance energy transfer (FRET), by using locally excited fluorescent probes on the nanowire surface to excite molecules in a lipid bilayer or in a cell membrane¹²⁹. This type of highly localized sensing would be useful to investigate the possible penetration of a wire into a cell, for cell injection studies^{118,130,131}, or the conformation of a lipid bilayer on the nanowires¹³², determined by fluorescent molecules labeled along the exterior the cell membrane or bilayer. If for example a wire has broken through the membrane¹³⁰ or if the membrane or bilayer is fully wrapped around the wire^{106,132}, the use of fluorescent nanowires would allow for a simple optical check to see if, for example, molecules could be injected into a cell,

without the need for tedious and time consuming transmission electron microscopy or focused ion beam milling of the cell¹⁰⁶.

An effective tool in such biosensing techniques is the ability to increase signal-to-noise and reduce the amount of false positives caused by, for example, non-specific binding of molecules. In order to improve signal-to-noise and increase read-out reliability, several repeats of similarly treated nanowires in an ordered array could be used. We demonstrated the use of square arrays of approximately 2500 nanowires in less than 80 μm^2 area. The possibility to increase this number of nanowires to a few hundred thousand in a few hundred square microns area is also readily achievable using EBL in short time scales. Moreover, using state-of-the-art lithography techniques such as nano-imprint lithography, one could pattern an entire wafer with millions of nanowires in relatively fast time scales¹³³, while obtaining highly consistent samples in parallel. Finally, a higher level of sophistication for such nano-biosensors using light-guiding would be achieved by multiplexing the nanowire sensing capabilities¹¹¹. The possibility of such a sensing platform in the same device would require the use of microfluidic channels used as spacers between arrays, in this way individual regions of the device could be functionalized to detect a variety of target molecules.

4. Computation devices

The identification of intractable mathematical problems¹³⁴, and need for faster ways to solve them, has lead towards the search for alternative methods of computing, extending beyond the grasp of modern serial computers, to more parallel approaches. Examples like the Subset Sum Problem (SSP) and the Traveling Salesman Problem (TSP) become intractable when the number of variables, i.e. the set of numbers or cities, respectively, is very large. These problems belong to a class of mathematical problems known as NP-Complete¹³⁵. The combinatorial nature of these problems requires a parallel approach in order to solve instances for which serial computation is impractical. Molecular motors, on the other hand may be used as to solve such computationally complex problems in comparably fast time scales, as they are naturally small, energy efficient and self-propelled, i.e. they do not require an externally driven power supply. We demonstrate the ability to solve an instance of the SSP using actin filaments and microtubules propelled by myosin and kinesin molecular motors, respectively, in a two-dimensional network, as a new parallel computing method. This chapter describes the benefits and limitations of alternative parallel computing techniques, and the advantages and challenges of using actomyosin-based computation in terms of scalability and energy efficiency.

4.1. Computational problems

Decision problems. In order to understand NP-Completeness, we build on the most basic class of problems known as *decision* problems. A decision problem is a class of problems that poses questions having a yes or no answer, for a generic instance of the problem¹³⁵. Suppose we have the following problem: for a given real and positive integer, n , e.g. $n = 13$, does m , a real and positive integer, e.g. $m = 7$ divide n evenly? If yes then m is a solution if no it is not a solution. Because we can easily check if m divides n evenly in this case, the problem can be solved quickly. In this example, the possible inputs would be the set of natural numbers. In a general sense, the decision problem can be described as the set of instances D , having a set of yes solutions in that set $Y \subseteq D$ ¹³⁵.

Time complexity and the class P. The time required for solving a decision problem will determine its complexity. Figure 4.1 shows the time growth for finding solutions using polynomial $f(n) = C*n^x$ and exponential $g(n) = C*k^n$ algorithms for a given problem. For comparison, the functions plotted are: the polynomial function $f(n) = n^3$ and exponential function $g(n) = 2^n$, where n represents the set of natural numbers. A decision problem, which can be solved in polynomial time, is a class P problem. This means that for a given instance of the problem, a polynomial time algorithm exists for finding solutions of yes or no. Such problems include, the example given above, i.e. does m divide n evenly? A problem which cannot be solved in polynomial time is generally referred to as a class E problem, and it can be stated that $P \subset E$. It is for those more difficult problems, i.e. those having exponential time complexity, that we find the most interesting in real world applications, e.g. in optimal network routing^{19,20}, protein folding²⁴⁻²⁶, and cryptography²¹⁻²³. The order of the time complexity $O(f(n))$, is based on the function (algorithm) used to solve a given problem, i.e. if the function is polynomial $f(n) = C*n^x$, the time complexity is polynomial $O(n^x)$. For algorithms that include both exponential and polynomial components the order of the function will be dominated by the exponential function for large values of n . In consideration of computation techniques, using a highly parallel computation method would be beneficial for solving problems, which have exponential time complexity, faster and potentially reduce them to polynomial time complexity¹³⁶.

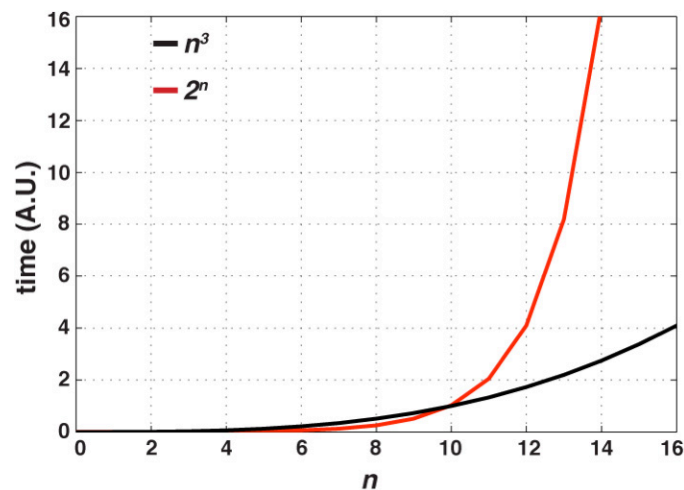


Figure 4.1. Graph representing exponential (red curve) and polynomial (black curve) time growth in arbitrary units (A.U.) of time. For small values of n , there is little difference between exponential and polynomial time growth, however, as n increases the complexity of problems requiring exponential algorithms for finding a solution becomes quite demanding and therefore have a rapidly increase time constraint. In this example $x = 3$.

Non-deterministic polynomial time problems and P vs. NP. A non-deterministic polynomial time (NP) problem is a decision problem for which the solutions having a yes instance also have proofs, which can be verified in polynomial time. Here, non-deterministic means that for a given input, multiple outputs can exist. If a problem or system is deterministic then each input will yield a specific output, i.e. a single pre-determined result must exist for every input whether or not is a yes or no solution. A proof is a mathematical equation or logical argument that verifies the truthfulness of a statement. It is not known if there exists a polynomial time algorithm for solving NP problems, that is if $P = NP$ or if $P \neq NP$. In mathematics this is one of the most challenging problem which is currently unanswered¹³⁷. In general, this problem asks: if an NP-problem has a solution, which is verifiable in polynomial time, is there an exiting algorithm, which can be used to solve it in polynomial time? The verification of whether $P = NP$ or $P \neq NP$ holds significance not only in the field of mathematics, but also in other areas governed by computational complexity such as artificial intelligence, game theory, logistics, biological processes, e.g. protein folding, and cryptography.

NP-complete and hard problems. The class of NP-complete problems are more difficult to solve than P-problems due to their exponential time complexity, that is finding solutions to these problems generally requires exponential time. A few examples of known NP-complete problems are the Boolean satisfiability (SAT) problem, the knapsack problem, and the Traveling Salesman problem (TSP)¹³⁵. The TSP is typically represented as an optimization problem that searches for the shortest path, which connects a number of different points n , on a graph¹³⁸. For example, if a salesperson must visit a number of cities n , the question is: what is the shortest path that they should take in order to visit each city exactly once? Written as a decision problem, the question would be: given a number of points on a graph, e.g. $n = 30$, does a path p exist which goes through all n exactly once, such that the length of p , is less than or equal to, e.g. $k = 100$? It is clear that as the number of cities increases, this problem requires exponential time to solve. This problem is most commonly found in optimized network routing in, for example, social, biological or wireless networks^{19,20}. NP-hard problems are at least as hard as NP-complete problems, however, they are not required to be within NP or to be decision problems¹³⁵. They do not necessarily have solutions that are verifiable in polynomial time. For the TSP example above, an NP-hard version would ask for all possible paths p_i , passing through all points once, with lengths less than or equal to a given k .

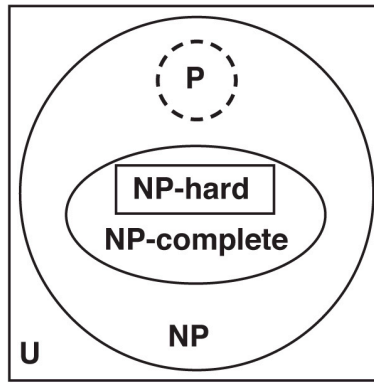


Figure 4.2. Schematic of decision problems. U are all of the decision problems in the universe. NP are non-deterministic polynomial time problems, e.g. those for which if you are given a solution, you can determine if it's true in polynomial time. NP-complete are not expected to be solvable in polynomial time, but given a specific solution, it can be verified in polynomial time. NP-hard problems are at least as hard as the NP-complete but may not be in NP. P problems are calculable in polynomial time. A question as to whether all NP are solvable in polynomial time, i.e. is $NP = P?$, is currently up for debate.

A schematic is used in figure 4.2, in order to describe graphically the relatedness of the different types of decision problems. If $P = NP$, then problems for which only an exponential algorithm currently exists, may be solvable in polynomial time. The class of NP-complete problems, for instance, could be solved if $P = NP$, since by definition a problem can only be NP-complete if it is in NP and if all problems in NP are transformable to that problem in polynomial time¹³⁵.

4.1.1. Subset Sum problem

Here we focus on the subset sum problem (SSP)¹³⁹, which is a NP-complete problem relevant to computational complexity theory and in cryptography¹⁴⁰⁻¹⁴³. We chose the SSP as it is readily translatable into a 2D graph composed of isomorphic unit cells, in which we encode the problem. The SSP can be described in two versions. One version is the same sum problem, in which one would like to know a subset of distinct positive real numbers which sum to the same value from a given set¹⁴⁴. In the other, integer relation version, we want to find all possible sums, which can be found from a given set, including the set values¹⁴⁵. In the encoded network, for small sets, we can identify solutions to both of these versions of the SSP. Mathematically, we can describe the SSP as follows. Given a set $S = (s_1, s_2, \dots, s_n)$, and the set or weights, $W = w_1, w_2, \dots, w_n$, ($w_i \in \{0, 1\}$), is there a subset of $S' \subset S$ and W such that:

$$T = \sum_{i=1}^n w_i s_i \quad (4.1)$$

where T is a positive real integer? As the size of S increases the problem becomes increasingly more difficult to solve. Because W is a binary set, the possible combinations of the set is given by 2^n , therefore the time it takes to cycle through all possible combinations of W , is 2^n , and it is therefore assigned to the exponential time class. If we would ask for all possible target sums T that exist for a given set S , this problem would be classified as an NP-hard problem. For a special class of SSPs, namely the super increasing SSP, a public-key cryptographic system was designed by Merkle and Hellman in 1978²². This cryptographic system uses a super increasing set $A = (a_1, a_2, \dots, a_n)$, such that each successive a_i is greater than all values in the set summed together, which come before it, and a method by which the order of the set is scrambled (encoding the message) into a new set $A' = (a'_1, a'_2, \dots, a'_n)$. The power of such an algorithm for cryptography relies on the value of n and the number of bits used for each a_i .

4.2. Parallel computing methods

As some problems - mathematical or biological - require highly parallel processing, other computing techniques have been investigated as alternatives due to their potential computational efficacy. DNA computing, for instance, under development for two decades, started by using DNA strands to perform a simple computation of the TSP²⁷. Although other methods have been proposed^{28,146,147}, issues with this technique persist, such as a need for large quantities for reaction volumes¹⁴⁸ and time constraints¹⁴⁹⁻¹⁵². Quantum computing has been proposed as another alternative¹⁵³, however, it is still far from establishing a significant contribution to solving difficult problems, due in part to limitations such as decoherence^{29,154}.

Other computing techniques exist for problem solving. Here a few of these methods are discussed briefly for context. The computing techniques described below do not necessarily all belong to biocomputation, but are listed as a point of reference. Each method for computing is discussed in terms of practical implementation or use, including a description of scalability and time requirements.

4.2.1. DNA-computation

Adleman computing model. DNA-based computing was first demonstrated by Leonard M. Adleman in 1994. A single string of DNA is comprised of the bases: adenosine (A), thymidine (T), cytosine (C) and guanidine (G). These bases join to form pairs (A with T and C with G), and thus make complementary strands of

DNA from single strands. In this seminal work, Adleman used DNA to solve the TSP or directed Hamiltonian graph by a brute force method, which requires i) each vertex or “city” on the graph should be visited exactly once ii) paths should start at a specified vertex v_{in} and end with a different vertex v_{out} . The graph described in Adleman’s experiment included seven vertices (v_1, v_2, \dots, v_7), and the algorithm for finding the Hamiltonian path from v_1 to v_7 was as follows: i) generate random paths through the graph, ii) keep only those paths which start with v_1 and end with v_7 , iii) if the graph contains n vertices, keep only paths which enter exactly n vertices, iv) keep the paths for which each vertex is visited only once, v) if any path remains it is a solution, if not, there is no solution²⁷. Here the vertices were single DNA strands of randomly generated oligonucleotides consisting of 20 nucleotides (20-mer) sequences denoted as (O_1, O_2, \dots, O_7). Here the edges of the Hamiltonian graph were made up of 20-mer bases, which were two 10-mer complementary bases for the different vertices, for example, O_1 could be joined to O_2 via a $O_{1 \rightarrow 2}$ string in a ligation reaction. Figure 4.3 gives an example of two 6-mer vertices joined to a complementary 6-mer edge.

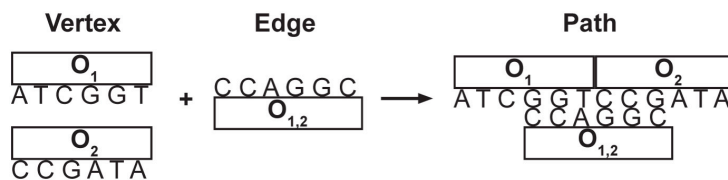


Figure 4.3. Schematic of a DNA computation event. The two vertices O_1 and O_2 comprised of 6-mer bases (oligonucleotides) are joined together by the “edge” $O_{1,2}$, which contains half of the complementary bases for O_1 and half for O_2 . This union creates the path from O_1 to O_2 .

In Adleman’s work, a computation event or operation was denoted as the formation of double strands of DNA from single strand compliments of the associated 20-mer vertices and edges in a ligation reaction. These ligation reactions took place in test tubes where, 50 pmol quantities for each vertex and edge were used. An estimated 10^{14} operations were achieved in the first step. The strands were then subject to polymerase chain reaction (PCR) to amplify only paths that started with O_1 and ended with O_7 . Following amplification, the DNA double-strands could be sorted based on molecular weight corresponding to the length of the strands. Thus, the strands with a length consisting of exactly 7 vertices could be identified. While other NP-complete problems have been experimentally solved using DNA¹⁵⁵, much of the work in this field has focused on devising new algorithms for solving different NP-complete problems using DNA^{28,149,150}.

Potentials and pitfalls. A primary benefit of DNA computing is that it is believed to achieve high parallelism and a capacity for vast amounts of storage, e.g. 1 μ mol

of DNA can potentially store up to 2 gigabytes of information^{149,155}. The energy efficiency is also unprecedented, as Adleman estimated that each ligation reaction requires only approximately $5 \cdot 10^{-20}$ J/operation (~ 12 kT/operation)²⁷. A significant drawback of DNA computing, however, is that the scalability requirements are quite high. DNA quantities needed for computations scale exponentially as the problem size, i.e. 2^n , and for large n , this is impractical to implement¹⁴⁸. For instance, in a DNA-based computation of the Maximal Clique problem, demonstrated by Ouyang *et al.*, the number of vertices n is restricted to 27 at picomolar concentrations of DNA, due to an exponential increase in the amount of DNA initially required for all possible paths to be searched¹⁵⁵. They estimate that increasing to nanomolar concentrations would allow for up to 36 vertices, while further increase in the number of vertices, thus increasing the complexity of the problem, would not be feasible¹⁵⁵. Time constraints exist, as mentioned above, as each ligation reaction “computation” and readout of these reactions can be time consuming^{27,155}, and require further optimization or newer faster methods for read out. Error rates are also important to consider when working with DNA-computing, which can arise from reaction based errors and those from the instability of the reaction volumes or the molecules themselves, i.e. non-specific or weak binding of oligonucleotides¹⁵⁰.

As the problem of scaling, related to amount of DNA required and large error rates, persists, the use of DNA computing will not be a viable potential alternative to solving NP-complete problems¹⁵⁶. Beyond NP-complete problems, however, DNA-computing techniques like biomolecular automation, DNA self-assembly and DNA-origami have been investigated to gain information on molecular processes and can even be used for molecular diagnostics^{151,157-163}.

4.2.2. Quantum computation

Another alternative form of computing has developed from the field of quantum mechanics. The quantum computer was first envisaged by Feynman in 1985, when he concluded¹⁶⁴, “...the laws of physics present no barrier to reducing the size of computers until bits are the size of atoms, and quantum behavior holds dominant sway”. Subsequently, many researchers have attempted to design and build this imagined quantum machine¹⁶⁵, which could potentially surpass modern computer performance in generating solutions to intractable problems^{153,166}.

While bits, 0 or 1, in an ordinary computer, exist in definite 2^n number of states, quantum binary digits (qubits) $|0\rangle$ or $|1\rangle$, can exist in a superposition of these states as 2^n states simultaneously. Since the qubits of a quantum computer can perform many operations quickly and simultaneously, the advantage of quantum computing is therefore, that those NP-complete problems with an exponential time

complexity could potentially be solved in polynomial time. The task of building a completely isolated system is a primary hurdle for quantum computing¹⁶⁷. This barrier is caused by quantum decoherence, as any contact with the outside environment can potentially cause serious perturbations in the phase of the qubit thus introducing error¹⁶⁸. Increasing decoherence time beyond that of the actual running time of the experiment is therefore a prerequisite. The use of quantum error correction, however, can be used to compensate for these errors to some degree, a key in scalability of such devices¹⁶⁹.

Quantum computing holds significant relevance in the field of cryptography²⁹. Secure encryption is vital for maintaining security for sending and receiving information and validation of the sender's signature in, for example, Internet banking transactions. Prime factorization is used in encryptions, for example in the RSA-problem, named after the designers Ron Rivest, Adi Shamir and Leonard Aldeman. The RSA-problem uses the product, n of two prime numbers (currently a few hundred digits long) and a ciphering and deciphering algorithm to create a public key and private key²³. In order for the integrity of the encryption to hold, it is essential that the private key is kept hidden. Modern computers are limited in deciphering "cracking" these types of problems, where a private key, shared between two users, contains a large number of bits n , requiring 2^{n-1} attempts in order to search through all possible combinations. This brute force attack would of course take exponential time and resources as n becomes larger and larger. It is believed that if quantum computing reaches the level of development that is predicted, it could be used to decrypt these public keys in polynomial time scale thus affecting the security of RSA and other cryptosystems.

Potential benefits from quantum computers include the application to very large scale integration (VLSI) advancement. VLSI is limited in the reduction of the size of transistors that can fit onto the surface of a chip due to, among other things, direct source-drain tunneling, extending from quantum mechanical effects that dominate at small scales¹⁷⁰. Taking advantage of quantum computing could help to increase the performance of current VLSI devices or replace them altogether. Testing of these devices containing millions or billions of transistors is also a daunting task, considered to be NP-complete¹⁷¹. Using quantum computing, it could be possible to quickly determine the quality of a given circuit reducing time and costs in production and manufacturing¹⁷¹.

Though a variety of material and techniques are being evaluated for creating a quantum computer¹⁶⁸, to date only very trivial problems have been solved by quantum computing such as the factorization of numbers with up to three digits^{172,173}. However, with improved error correction¹⁷⁴, it is likely that we will see a technological breakthrough for this field in the not too distant future, though widespread commercial availability is much further down the road.

4.2.3. Other computation techniques

Other types of computing are under development including neuronal and optical computing and spintronics among others, which aim to either supplement or replace modern computing techniques. Neuronal computing could also be used in solving NP-complete problems¹⁷⁵. It has also been proposed that neural networks can be used to encode some type of logical programming in order to perform digital calculations such as AND and OR operations¹⁵⁴. More commonly, research is aimed at using neural networks as a model system, where networks of artificial design are connected in a similar way as neurons in living systems¹⁷⁶⁻¹⁷⁸. This form of computing holds potential for instance in recognition development, useful for human-machine interaction^{176,179}. Optical computing is another technique that has been under development for the last few decades¹⁸⁰⁻¹⁸³, it relies on replacement of electrons, used in standard computing, with photons produced from lasers or diodes¹⁸⁴. Spintronics or magneto-electronics is under development as a replacement or complement to current transistor technology and is based on the intrinsic spin of electrons and their magnetic moment and charge^{185,186}. Microfluidics has also been used for solving a small-scale instance of an NP-complete problem¹⁰. However, the ability to scale up the problem would require unreasonably large external pressures to force fluids through channels and is not suggested to be a viable computing approach¹⁰, but may be useful for supplementing DNA techniques¹⁸⁷.

4.3. Biocomputation with molecular motors

As the above mentioned methods of computing offer their own benefits and drawbacks, none of these have been able to outperform a modern computer, as yet. There exists another alternative, i.e. biocomputation with molecular motors, which may offer this possibility, due to their small size, energy efficiency and self-propelled motion, i.e. they do not rely on an externally driven power supply.

Biocomputation with molecular motors was envisaged by Nicolau *et al.*, where they discussed the possibility to use thousands of molecular motors to perform highly parallel computation in a nano-scale device³⁰. In their work, they described a directed network, which encodes the subset sum problem (SSP). In our work, we demonstrate the realization of such a directed two-dimensional network, where molecular motors propel actin filaments and microtubules (agents) through a series of junctions terminating at exits, where all possible subsets (solutions) for a specific instance of the SSP can be read out.

Development of a proper network for encoding the mathematical problem of interest is at the basis of designing a functional biocomputation device. However, other components are also required to fulfill criteria related to scalability of such a device. Figure 4.4 gives an overview of a generic biocomputation device. The essential device components are i) large source inlet, required for delivering many motile objects needed for computation, ii) parallel computing network with all possible paths leading to a solution in the given problem, iii) junctions which can be designed for desired functionality, i.e. passive junctions connected to active junctions that are responsible for agents making decisions or gated junctions which can be used to control agents in time, adding an extra dimension to the problem solving, and iv) detectors which enable local read out of filaments, useful for error reduction in detection.

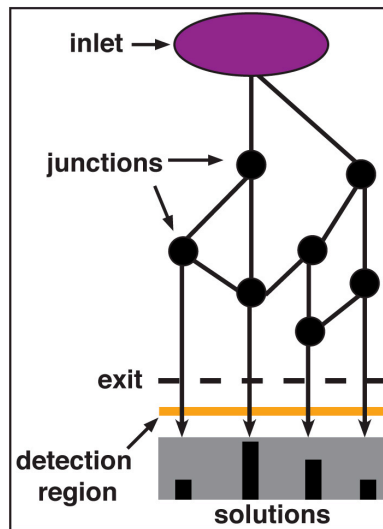


Figure 4.4. Schematic example of biocomputation device. In a directed network, agents (actin or microtubules) should enter at one inlet and traverse the network in a consistent forward direction. Individual junctions should be passive, allowing objects to continue on their path, or active, with the capability to stop or start motion or change the trajectory from left to right, for example. Detectors should be included at exits in order to count the number of motile objects exiting at a particular solution. They may also be included throughout the network to enable tracking up solutions to the starting point.

In order to encode our problem of interest, namely, the SSP, we write the mathematical formulation, shown in equation 4.1, in terms of motion of motile objects in the device. We choose the set of positive real integers ($S = s_1, s_2, \dots, s_n$), for example, $s_1 = 2$, $s_2 = 5$, and $s_3 = 9$. At every s_i , the motile object can move in the x-direction or the y-direction by a number of steps set by the value of s_i , i.e. +2, +5, or +9 for s_1 , s_2 , and s_3 , respectively. If the object moves in the x-direction

there is an increase (addition) in the final solution value. If the object moves in the y-direction, there is no increase in the final solution value. We assign binary values (0,1) for adding in the x-direction and determine the possible solutions or target sums T :

$$T = \sum_{i=1}^n x_i * s_i \quad (4.2).$$

Figure 4.5 shows a schematic representation of the graph for the set $[2, 5, 9]$, i.e. the instance of the SSP we encode. For each s_i we add to the total solution value, so that if we go two steps in the x-direction at s_1 and five steps in the y direction at s_2 , then nine steps in the x-direction at s_3 , the final sum is: $(1*s_1 + 0*s_2 + 1*s_3 = s_1 + s_3 = 2 + 9 = 11)$. This path is shown in figure 4.5 in yellow. If the motile object starts from the entry point and moves only in the y-direction, the sum is given by: $(0*s_1 + 0*s_2 + 0*s_3 = 0)$, this path is the trivial solution and is given by the blue curve in figure 4.5. Exits which are target sums T (2, 5, 7, 9, 11, 14 and 16) as well as the trivial solution 0. Those exits which are not target sums (1, 3, 4, 6, 8, 10, 12, 13 and 15) are shown in pink. Because the graph is directed, no values can be subtracted from the sum, i.e. only positive integer addition is possible.

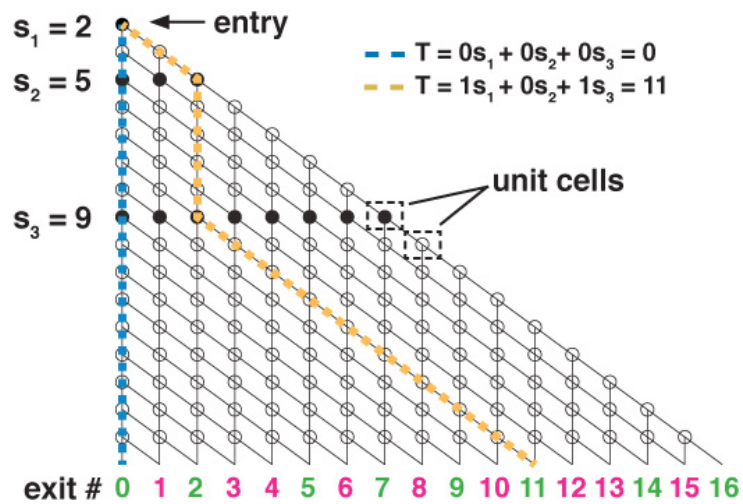


Figure 4.5. Schematic of subset sum graph for the set $[2, 5, 9]$. Filled circles represent junctions where x or y movement is possible, while open circles represent junctions where no change in direction can occur. The motile objects start at the upper left hand corner. The exits are marked by their corresponding values. Exits marked in green are target sums T while those marked in pink are not target sums. Two example paths are shown by dashed lines: the trivial solution, $T = 0$ (blue), and the sum $T = 11$ (yellow). Figure modified from Article III.

4.3.1. Device design

Unit cells. Depending on the given set S , the SSP is translated into a two dimensional graphical network of isomorphic unit cells. The unit cells consist of two types of junctions: split-junctions (S-junction, filled circles in figure 4.5), and pass-junctions (P-junction, open circles in figure 4.5). Each type of junction is designed to guide the motile objects so that they can solve the problem, as long as they obey the encoded architecture of the junction design. S-junctions are designed as crossings, allowing the filaments to go either in the same direction as they are traveling or to turn, with an expected split of 50 percent. P-junctions are designed to only allow the filaments to continue in the same direction from which they came. Figure 4.6 provides details on the unit cells for both the P- and S-junction designs. For P-junctions, filaments entering from side A or B exit at 2 or 1, respectively. S-junctions allow filaments to randomly turn, when entering from A or B, to exit at either 1 or 2.

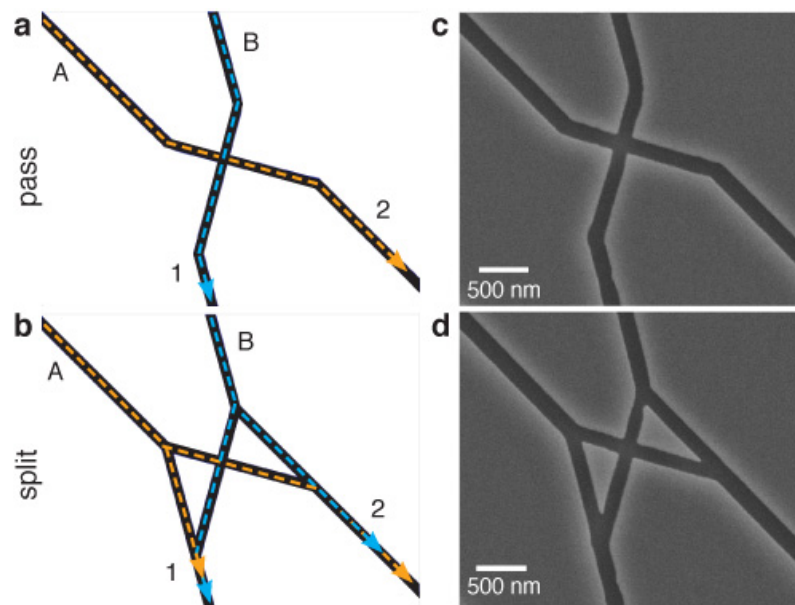


Figure 4.6. Schematics and scanning electron micrographs of the two types of junctions. a) Unit cell of P-junction with designed paths depicted by colored arrows, i.e. filaments coming from A and exiting at 2 (A2) is an intended path, but filaments entering at A and exiting at 1 (A1) is not an intended path. b) Unit cell of S-junction with colored arrows showing the designed paths. Here, for example, A2 and A1 are both intended paths. c) Scanning electron micrograph of P-junction. d) Scanning electron micrograph of S-junction. Scale bar in c-d is 500 nm. SEM images were obtained after sputtering samples with 5 nm of Pt. Figure modified from Article III.

Device fabrication and design. The device fabrication was performed as described in Chapter 2.3. PMMA was used as a resist mask to create structures with EBL, see figure 2.4 for detail. The design of the computing network is based on the set [2, 5, 9], comprised of rows of S- and P-junctions, as shown in figure 4.7. Here we make use of the guiding properties of edges⁵³ by including many loading zones, i.e. regions for filament landing and transport^{53,60}, connected by nanochannels, which lead filaments to the computing network. Heart-shaped rectifiers^{2,79}, shown in figure 4.7, are also included in the design at strategic positions in channels leading to and from the network. These rectifiers maintain filament directionality such that filaments are concentrated to the entrance of the network and no filament should be able to turn around and enter from the wrong direction, i.e. the exits.

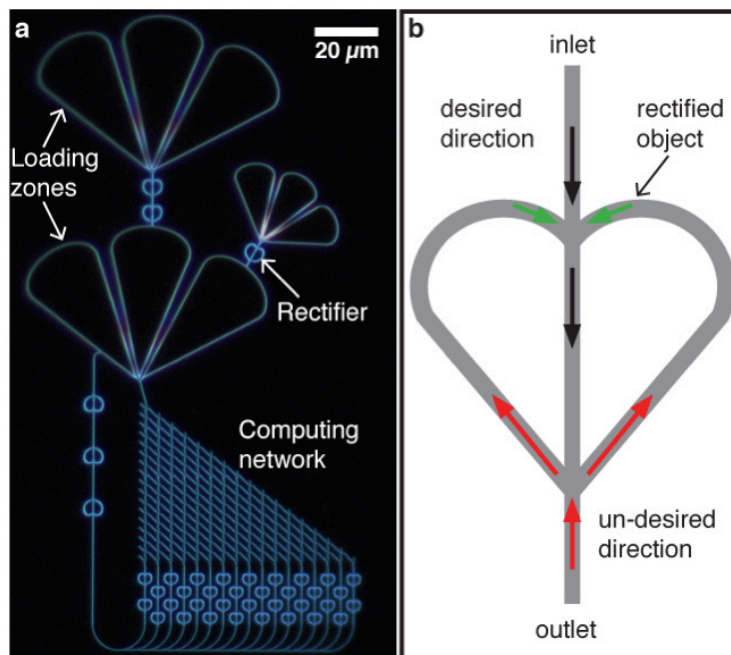


Figure 4.7. Dark field optical micrograph of biocomputation device design for the set [2, 5, 9] and schematic of rectifier. a) A series of loading zones (large open areas) are used for adsorption of functional HMM molecules to the surface for transport of actin filaments. Heart shaped rectifiers are added to filament guiding channels for directed movement to and from the computing network. See figure 4.6 for details on the junctions. Exiting filaments are collected and recycled through the network via feedback loops at the exit row. b) Rectifiers are designed to direct traffic flow in connecting channels, such that all filaments are forced to move in one preferred direction (black arrows). Those filaments traveling in the wrong direction (red arrow) will be guided into the rectifiers (based on the geometry used) and will be redirected (green arrows). Figure modified from Article III.

4.3.2. Error requirements and device performance

In order to confirm the device performance the junctions were first tested and evaluated for error. In the following subsection a description of error in the junctions is described. Finally, the overall device performance is described in terms of the exits where individual filaments arrived. A brief discussion is also included on possible improvements to the device.

Error in junctions. Errors in P-junctions can be propagated through the network and lead to the filaments exiting at positions, which do not correspond to target sums for the set. This is rather important to understand when designing the junctions and when deciding on the particular motile objects that will be used, as higher flexibility of actin filaments versus microtubules can lead to higher error at the crossings¹⁸⁸. If defects exist in P-junctions early on in the network, causing filaments to change their trajectory, this could lead to a number of incorrect calculations (additions) in the network for every subsequent row of S-junctions that the filaments encounter. Depending on the number of n in the chosen set ($S = s_1, s_2, \dots, s_n$), and the magnitude of each n , the significance of properly working P-junctions is more severe. As the magnitude of n grows, the number of P-junctions increases, therefore error in P-junctions could lead to a higher number of filaments arriving at incorrect solutions at the exits thus reducing signal (actual target sums) to noise (incorrect solutions).

An uneven distribution in S-junctions could lead to another form of error. That is to say, if too few filaments are directed in one side of the junction over the other, then this biasing could significantly reduce number of filaments at a given target. If the number of filaments arriving at a particular target sum is too low, i.e. on the same level as the “noise” caused by error in P-junctions, this target sum could be missed altogether.

Junction performance. Table 4.2 and 4.3 summarize the performance for each type of junction. The P-junctions and S-junctions were analyzed by tracking individual filaments through the devices. This information was used to gauge the performance of the junctions and as an input to Monte Carlo simulations of overall device performance (see figure 4.8).

	A1	A2	B1	B2	Tot A	Tot B	Tot
# Filaments	55	1885	1706	23	1940	1729	3669
Total Fraction	2.8%	97.2%	98.7%	1.3%			

Table 4.2: P-junction performance in the [2, 5, 9] subset sum device. A1, A2, B1, B2 denote the paths taken through the junction. For example: “A1” indicates a filament that entered the device through channel A and left the device through channel 1. Paths for which the P-junction was designed are shown in black. Those paths not intended in the design are shown in red. The total

fraction was obtained by taking the ratio of the number of filaments following a given path from one side divided by the total number of filaments entering the junction at that side.

	A1	A2	B1	B2	Tot A	Tot B	Tot
# Filaments	429	437	262	364	866	626	1492
Total Fraction	50%	50%	42%	58%			

Table 4.3: S-junction performance in the [2, 5, 9] subset sum device. A1, A2, B1, B2 denote the paths taken through the junction. The total fractions for A and B were obtained by taking the ratio of the number of filaments following a given path from one side divided by the total number of filaments entering the junction at that side.

In P-junctions, filaments recorded as making a wrong turn resulted in an overall error of 1-3%. This error lead to filaments exiting at incorrect sums (non-target sums) ~12% of the time or 273 incorrect sums out of a total of 2251 filaments counted at the exits. Though the error rate averaged over all P-junctions is low, a noticeable amount of “noise” is present, i.e. the S/N ratio ranges from 3 – 14. For S-junctions, the splitting ratio was in the range of 42/58 splitting for filaments entering at B, and 50/50 splitting for filaments entering at A, see figure 4.6 for junction details. This slightly higher bias on one side of the S-junctions was not significant enough to disturb the signal to noise ratio, i.e. target sums were statistically significantly different from non-target sums ($p < 0.001$; unpaired two-tailed t test). However, coupled with a higher error for P-junctions, this slightly uneven distribution could potentially have a detrimental effect when too few filaments are used in calculations. For example, doubling the error in P-junctions to 4% and maintaining the sample splitting for S-junctions, we no longer have a statistically significant difference for the trivial solution $T = 0$. Decreasing the total number of observed filaments exiting by two orders of magnitude (a possibility when scaling up for $n > 30$), while maintaining an error in P-junctions of 2%, results in suppression of target sums due to and low S/N ratios.

Device performance. After confirmation of the performance of the junctions, the full device (see figure 4.7) was evaluated. The results are summarized in figure 4.8 and include a comparison with Monte Carlo simulations of the device. The simulations are based on the experimental error tolerance of the junctions and the number of observed filaments for the device tested. The results show that the device performed as expected, i.e. all target sums of the set used, were found by the filaments, and the experimental results are well reproduced by the simulations.

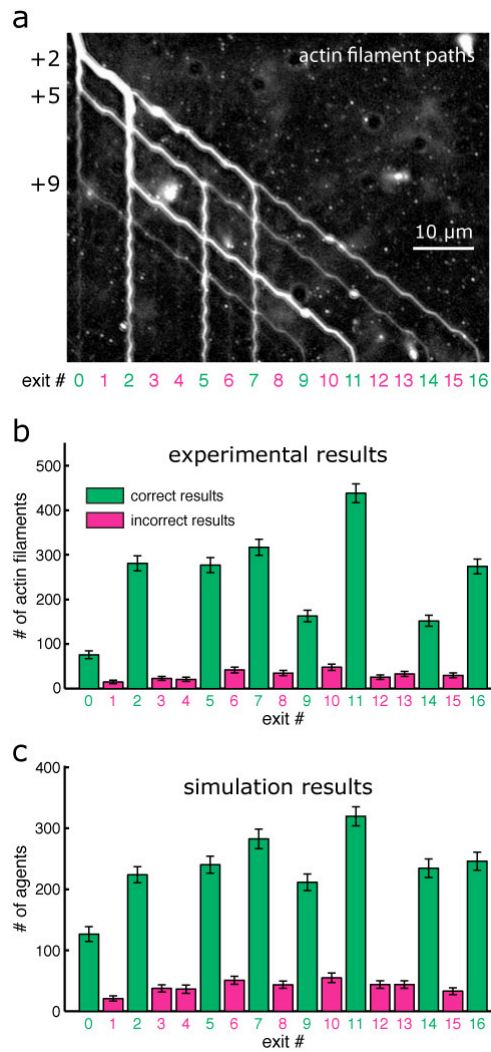


Figure 4.8. Solving the [2, 5, 9] subset sum problem by actin-filaments as agents. a) Average projection of several hundred typical fluorescence micrographs ($t \approx 50$ s) of actin filaments moving through a [2, 5, 9] device. b) Experimental results obtained from 2251 actin filaments arriving at exits. Error bars represent the counting error (\sqrt{n}). c) Monte Carlo simulation results (mean \pm standard deviation of 100 simulations) using the same number of total filaments, the measured error rates of the P-junctions, and measured splitting ratios of the S-junctions. (a-c) Green numbers and bars correspond to correct results (subset sums of the set) and magenta numbers and bars represent incorrect results. Figure modified from Article III.

Future considerations: scaling up. As mentioned above, an uneven distribution in the S-junctions is present, and this is partially reflected in figure 4.8, where the target sums have an unequal number of filaments across the set. This uneven distribution becomes more important when we consider the scaling up of such a

device. For larger sets, the number of filaments used must be increased based on the number of target sums predicted. As the magnitude of each s_i in the set S increases, we will observe a Gaussian distribution at the exits, with low number of filaments at very low and very high target sums. Therefore, the number of filaments required to find all target sums may need to be increased. This may be possible with enzymatic splitting filaments as they travel through the network¹⁸⁹. It is also relevant to consider the possibility of manipulating the design of the S-junctions to obtain a more even distribution of filaments at each target sum. In this way, the total time required for a significant number of filaments to reach each target sum can potentially be reduced. For sets with higher s_i values, the importance of P-junction performance is also critical. As the magnitude of each s_i increases, the number of P-junctions also increases, and thus the error can grow quickly across the device, leading to lower signal to noise ratio at the exits. This, coupled with an uneven distribution of filaments, can lead to an inability to identify target sums over the non-target sums. Therefore, in a scaled-up device, one would like to have an error tolerance $\ll 1\%$ in P-junctions.

Other requirements, related to scalability, include the monitoring of many numbers of exits (in large sets) and for counting filaments (potentially thousands) upon exiting. Therefore, detectors could be placed at the exits so that filaments can be automatically and efficiently tracked while leaving events in the bulk of the graph largely unknown. Here we would simply like to record “local” regions where filaments are detected and where we could easily ascertain that only filaments, which have been directed from the network, are counted. The design of such local detection points is described in the following chapter as well as a discussion on the removal of false positives, such as filaments moving in the wrong direction, and those passing by in solution.

Summary. In order to summarize the results of our biocomputer, we note the following points about the scalability and performance of the device.

- 1) The unit cells are planar and modular, and thus fully scalable. This particular advantage over, for example, microfluidics-based networks¹⁰, is important in terms of engineering and versatility between molecular motor usage.
- 2) The size of the physical network grows polynomially as $\sim N^2$, while the size of the problem grows exponentially. As a result, a full device encoding the SSP, capable of competing with a modern PC, e.g. for $N = 30$, can fit onto a 2 inch wafer. Details provided in supplemental information for Article III.
- 3) The agents (molecular motors) used are small, fast and self-propelled. Similar to DNA-computing, the system does not require an external driving force in order to operate.
- 4) As a result of the high speed of the agents ($\sim 10 \mu\text{m}^2/\text{s}$ for actin filaments), the time required to find solutions is fast, and in a fully scaled device, e.g. for $N =$

30, our biocomputer can potentially out-compete a modern PC in solution time.

- 5) The energy efficiency of our agents is high, with an estimated energy requirement of $2 \cdot 10^{-14}$ J/operation, compared to modern electronic computers requiring $\sim 3-6 \cdot 10^{-10}$ J/operation¹⁹⁰.
- 6) The read out of solutions, in a fully scaled device, may be slow, without use of architectural elements (described in Ch. 5), and therefore, may be a limiting factor in terms of the ability of our biocomputer to compete with a PC.
- 7) The error in junctions, particularly in pass-junctions, is a limiting factor, in terms of accurately determining solutions (target sums in the SSP) to the problem. Therefore, error-free pass-junctions (discussed in Ch. 5) must be implemented in a fully scaled device, in order to increase accuracy.

5. Architectural elements

The previous chapter described the biocomputation network in which motile agents (actin filaments) are used to solve the SSP. This chapter provides details on architectural elements, see figure 4.6, which are designed to improve readout and reduce error in the biocomputation device. One element is a fluorescence interference contrast detector, enabling the possibility to track individual filaments, moving through or exiting the network, at checkpoints. By cross-correlating the signal from pairs of detectors, we can ascertain the direction of motion and reduce error in counting. Another element is a hollow nanowire, which allows fully confined uni-directional transport of actin filaments. With these hollow nanowires, we can create error free pass-junctions in the network, thus greatly improving the signal to noise regarding the readout of filaments at exits.

5.1. Detection: fluorescence contrast checkpoints

Fluorescence interference contrast (FLIC) is an optical method that has been developed for many biological applications¹⁹¹⁻¹⁹⁵. In an IVMA where actin filaments (or microtubules) are fluorescently labeled with fluorophores, we can optimize signal to noise with FLIC to enhance the optical (fluorescent) signal in contrast to the background. The optical signal can then be used to count many actin filaments at local detection points. In applications where one would like to track many filaments, for example, at the exits, in a biocomputation device, we can use FLIC detectors, in which individual filaments could be identified and the number of false positives could be reduced. The basic principles of this method are described below.

5.1.1. FLIC Theory

Fluorescence interference contrast can be used to turn on or off the signal of a fluorescent object near a surface, based on a fundamental optical phenomenon. Light from an excitation source impinges on a reflective surface, e.g. Si, through a semi-transparent oxide layer, e.g. SiO₂. This incoming light is then reflected and subsequently excites fluorophores on the actin filament above the silicon oxide

surface. The emission signals of the fluorophores excited directly by the source or indirectly by reflected light can interfere. This interference can be either constructive or destructive, due to a phase shift in the reflected signals, thus enhancing or quenching the detected fluorescence respectively, see figure 5.1.

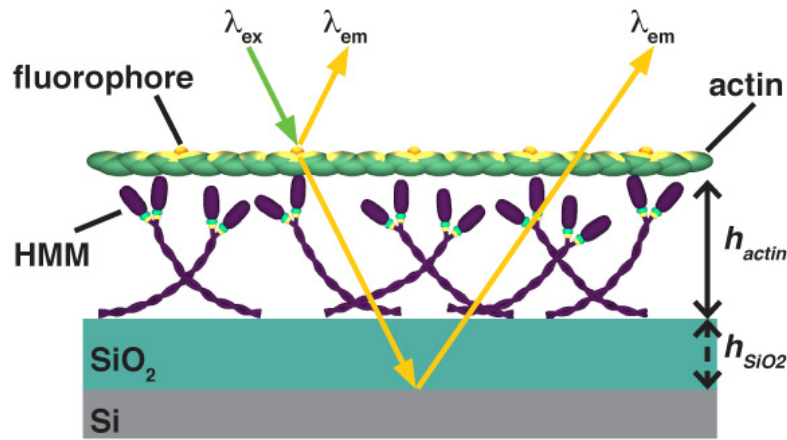


Figure 5.1. Schematic of FLIC concept. Here h_{SiO_2} (the thickness of the SiO_2 layer) can be tuned in order to adjust the enhancement or quenching of the fluorescence signal of excited fluorophores on the actin filament. See equation (5.1) for more detail.

These interference patterns can be used to determine the position of a fluorescent object, e.g. a labeled actin filament or microtubule, above the surface of the SiO_2 , with high precision and nanometer accuracy^{192,194,195}, and is represented as a double sin squared modulation of the intensity¹⁹³ according to:

$$I_{FLIC} = \sin^2\left(\frac{2\pi}{\lambda_{ex}}(n_{SiO_2}h_{SiO_2} + n_w h_{actin})\right) \sin^2\left(\frac{2\pi}{\lambda_{em}}(n_{SiO_2}h_{SiO_2} + n_w h_{actin})\right) \quad (5.1),$$

where excitation (λ_{ex}) and emission (λ_{em}) wavelengths depend on the fluorescent molecule used. The indices of refraction for the oxide and medium of immersion are determined by the system used. The thickness of the oxide layer above the reflective surface or the height that the fluorescent object sits above the surface, can be modified, in order to induce constructive or destructive interference in the emission signal of the fluorescent object. In this way, FLIC can be used to characterize numerous experimental systems, as a way to gain a deeper understanding of biophysical interactions and their applications¹⁹³⁻¹⁹⁵.

Figure 5.2 shows the normalized fluorescence intensity plotted as a function of the oxide thickness h_{SiO_2} , for TRITC and FITC excitation and emission wavelengths.

The indices of refraction for water and SiO₂ are $n_w = 1.33$ and $n_{\text{SiO}_2} = 1.46$. Finally, the height of the fluorophore is $h_{\text{actin}} = 40$ nm, determined by the height that actin filaments are held above the surface by HMM¹⁹⁵. For thicker layers of SiO₂ (> 300) nm, the FLIC curve will become “smeared” or spread primarily due to the objective having a finite numerical aperture and the fluorophores having polychromatic emission¹⁹³. This smearing is not represented in figure 5.2. In order to take full advantage of the FLIC effect, oxide layers above the reflective surface are desired to be less than a few hundred nanometers. One can also use a combination of different thicknesses of SiO₂ in order to create regions of local enhancement and quenching of the fluorescence signal.

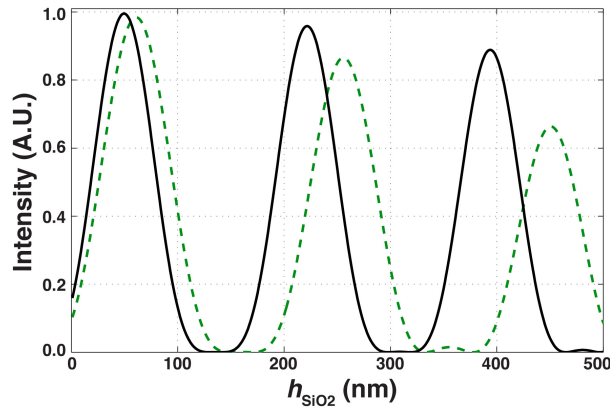


Figure 5.2. Graph of FLIC curve for SiO₂ on Si. Using equation 5.1, the maximum and minimum intensity contrast can be found for the two filter sets if interest in our experiments with actinomyosin. The tetra methyl rhodamine iso-thiocyanate (TRITC) filter set corresponds to $\lambda_{\text{ex}} = 540$ nm and $\lambda_{\text{em}} = 605$ nm (dashed green curve). The fluorescein isothiocyanate (FITC) filter set corresponds to $\lambda_{\text{ex}} = 488$ nm and $\lambda_{\text{em}} = 519$ nm (solid black curve). See text for details.

5.1.2. Device Design

In order to create local detection points on the surface that would later be integrated with the biocomputation device, we set up a scheme where Au lines coated with SiO₂ acted as the reflective surface “locally” on a patterned SiO₂/Si chip. Here the Au lines were placed patterned perpendicular to the nanochannels running between two large regions (loading zones) where actin filaments could move freely and enter the nanochannels. Loading zones and nanochannels were fabricated from a double-layer resist system (PMMA/LOR), for details see Article IV. As the filaments passed the Au lines (covered with SiO₂) their fluorescence signal was effectively increased. Figure 5.3 gives an example of such a local enhancement where one filament is passing over three consecutive 2 μm wide Au

lines with 2 – 3 μm wide gaps in between. It is clear that there is enhancement of the fluorescence signal. We would like to be able to ensure that filaments can be distinguished easily above the noise level and to identify the direction of movement (applicable for biocomputation).

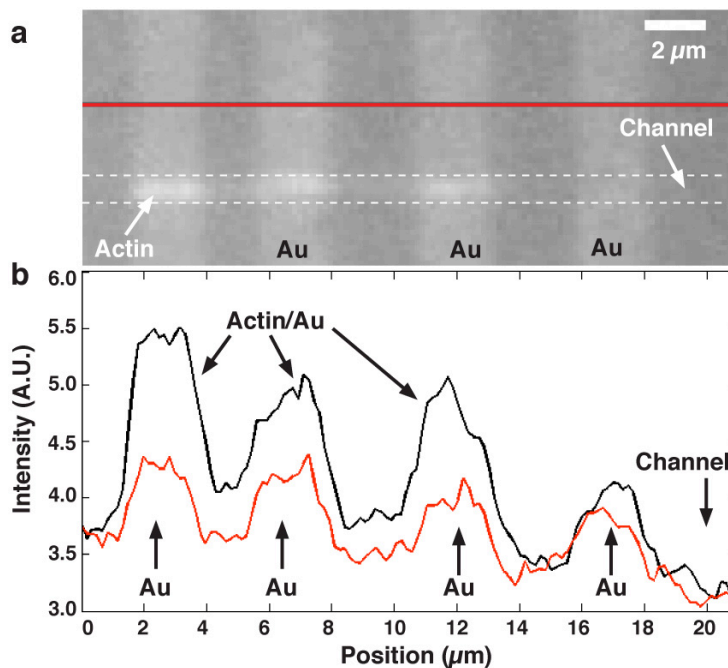


Figure 5.3. Fluorescence micrograph and intensity profile of filament on and off the FLIC detectors. a) Fluorescence micrograph from an IVMA. A single filament ($\sim 12.2 \mu\text{m}$ long) passes over three consecutive Au lines ($2 \mu\text{m}$ wide) in the nanochannel. SiO_2 is added $h_{\text{SiO}_2} = 240 \text{ nm}$ above the Au lines creating local enhancement. The channel region is demarcated by two dashed lines. Channel width is approximately 260 nm wide at the base. b) Fluorescence intensity profile of the filament (black curve) is shown including a reference trace (red curve) corresponding to the intensity profile along the red line in (a). The intensity profile measured with a single pixel wide line approximately $21 \mu\text{m}$ long. The filament extends slightly over the third Au line (from left to right). In the last segment of the figure (denoted “Channel”) no filament is present.

5.1.3. Cross-correlation

In order to reduce the errors in this design, we make use of cross-correlation, by which the fluorescence signal from two detectors (D_1 and D_2) can be correlated. Errors in this case may be attributed to filaments that pass by the detectors going the wrong way along the channels or filaments that may be floating in solution, causing an increase in the fluorescence signal when passing by the detectors.

Using this method, we can also identify the speed of the filaments. As shown in figure 5.4, we have two Au lines used as individual detectors, spaced a few microns apart. As a filament passes the first detector the signal (D_1) on this position is increased accordingly, while the second detector has only a background signal. As the filament encounters the second detector, the signal (D_2) is recorded, but with some time delay from the first detector. Each detection region can be plotted and the signals can be cross-correlated by shifting one detector's signal back in time with respect to the other based on the physical positioning. For example, in figure 5.4, D_2 would be shifted back in time with respect to D_1 in order to identify the maximum signal, corresponding to overlap of filament peak signals. The correlated signal of a filament passing both detectors is expected to be significantly higher than the background signal (uncorrelated). The multiplied intensity of the two correlated signals can be used to significantly remove noise from the background and increase the fluorescence signal of individual filaments, while at the same time removing those filaments that are possibly floating by in solution or passing the detectors in the wrong direction.

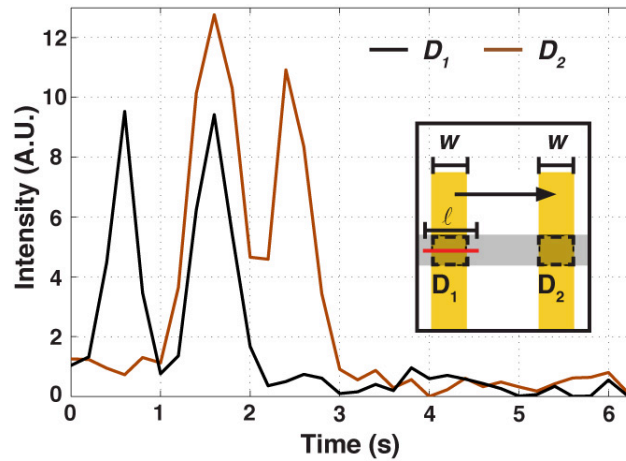


Figure 5.4. Two-line detector system. Here two filaments (observed by visual inspection) travel past each $2 \mu\text{m}$ wide (w) detector (D_1 and D_2) separated by $5 \mu\text{m}$ spacing. The background-subtracted fluorescent signals from the filaments are plotted over time for each detection position. The detection window corresponds to the $2 \mu\text{m}$ wide Au detectors at the nanochannel location. A single-pixel wide line is used to measure the fluorescence across the length of each detector. Here D_2 would be shifted back in time with respect to D_1 and the combined signal would be at a maximum after about 1 second shift time. Inset: Detectors having the same width, and a given separation. A single filament of length l (red) passes by the detectors from D_1 to D_2 as indicated by the arrow.

The cross-correlation method can be useful for identifying individual filaments and increasing signal to the noise, however, some errors can invariably remain. Considering the IVMA procedures used for actomyosin, the lower limit on the length of the filaments that can be tracked will be ($l > 1 \mu\text{m}$). This is due to the

limited motility of actin filaments, shorter than 1 μm , in the absence of methylcellulose¹⁹⁶. Such a restriction is relevant for nanotechnological applications where actomyosin is used^{55,58}. If two filaments are traveling in the nanochannel and have a separation below the minimum (i.e. $<$ detector width, w), the filaments may be recorded as a single filament. The minimum resolvable filament separation distance may be adjusted by increasing the frame rate, however, the speed or the standard deviation of filament speed, which can be caused by non-uniformity in the HMM layer or slight defects in the device, can lead to difficulties in resolving closely spaced filaments^{38,79}. A more detailed evaluation of the detector widths, spacing and filament lengths is described in the Article IV.

Summary and outlook. Local signal enhancement and error reduction in filament tracking is possible with the FLIC and cross-correlation techniques described. The ability to use FLIC detectors in a scaled-up version of our biocomputation device is possible with EBL or UV-lithography. In one configuration, the exits of the network can be positioned over a pair of detectors running the length of the device. In another arrangement, multiple detectors with varying spacing can be placed along the exits of the biocomputation network. In this way, it should be possible to select out filaments from different exits by performing different time shifts when cross-correlating filaments. This may be necessary, if, for example, the exits are aligned with very short spacing in between. Also, by placing these FLIC detectors throughout the network, we may be able to track different rows of junctions to identify information on splitting ratios etc.

5.2. Hollow nanowire tunnels

Here, we employ hollow nanowires (HNWs) to control transport of actin filaments, fully confined to 1D motion, useful for precise guiding at junctions in a biocomputation device as described in Chapter 4. In this section, we describe the method used to fabricate HNWs¹¹⁸ and the interfacing of these wires with an *in vitro* motility gliding assay.

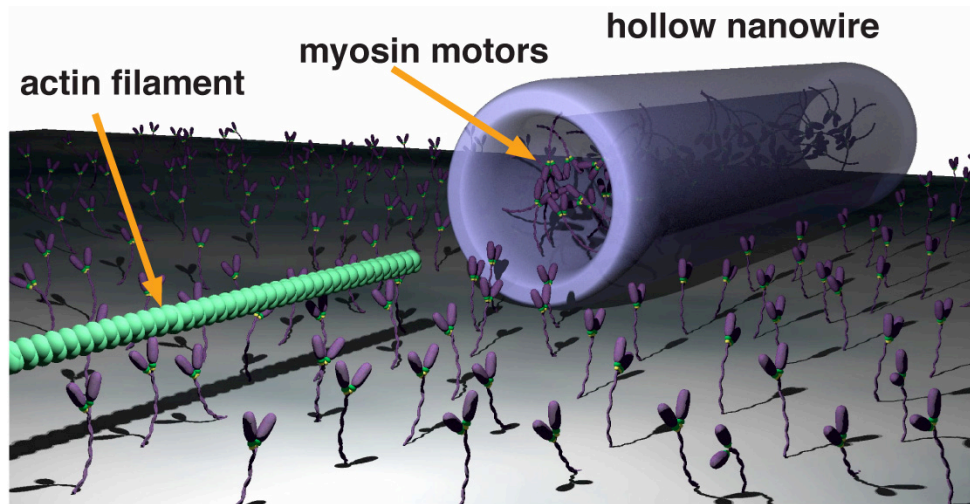


Figure 5.5: Schematic illustration of actin transport through hollow nanowire. HNWs made of Al_2O_3 are deposited on a SiO_2 surface. Myosin propels actin on the 2D surface and through the HNW in 1D. This type of control over the conformation of myosin and actin can be used in biocomputation networks (see Ch. 4) and potentially to study fundamental interactions of the molecular motor and cytoskeletal system.

5.2.1. HNW fabrication and alignment

Fabrication of HNWs. The HNWs are fabricated from particle-assisted MOVPE growth of gallium phosphide (GaP) nanowires coated with Al_2O_3 , as described in Chapter 2. Here, however, we do not pattern the Au particles in an array, but use aerosol deposition¹⁹⁷ to generate Au seed particles (~ 80 nm diameter with a density of $\sim 1/\mu\text{m}^2$) on the GaP surface for growth. In figure 5.6, a schematic of the fabrication process is shown. Briefly, Al_2O_3 coated GaP nanowires (Fig. 5.6a) are embedded in a resist by spin coating, leaving only the tips exposed (Fig. 5.6b). Next the sample is subject to etching with Argon plasma for approximately 15 min. This gas sputtered onto the surface of the sample, attacking and etching away the tips of the nanowires (Fig. 5.6c). Subsequently, the sample is exposed to oxygen plasma, for approximately 20 min, in order to remove the resist. Finally, the sample is immersed in nitro-hydrochloric acid ($\text{HNO}_3:\text{HCl}$; 1:3) in order to remove the exposed GaP core (Fig. 5.6d). The etching rate of GaP wires is approximately $1 \mu\text{m}$ per minute.

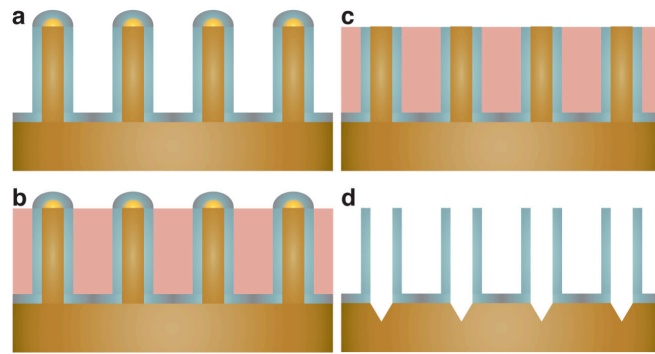


Figure 5.6: Schematic of hollow nanowire fabrication. a) GaP nanowires are used as a template for deposition of the ~60 nm thick Al_2O_3 shell deposited by atomic layer deposition. b) The coated nanowires are embedded in resist with the tips of the wires exposed. c) Etching of the tips is performed with argon plasma. d) Next, oxygen plasma is used to remove the resist, and the cores of the nanowires are removed by acid etching.

Our aim was to investigate the transport of actin filaments inside the HNWs. In order to do this, we can confine the HNWs under metal barriers, as a way to ensure that transport was inside the HNWs and not above or alongside⁸⁴ them. We first transfer HNWs to another surface (SiO_2/Si) and add metal lines on top in a lithographic process. The transfer is typically performed by contact method, i.e. using a piece of cleanroom tissue to break nanowires from their substrate and then to gently swipe it over the substrate intended for use. However, this results in a highly random distribution of wires on the surface. Here an alignment strategy¹⁹⁸ is used to enable precise placement of HNWs. Afterwards, metal contacts are aligned on top of the HNWs, in order to segment off areas of active transport, see figure 5.7. Whereby, HNWs act as tunnels between the regions. In this way, actin filaments could only reach the neighboring areas by traveling through the HNWs.

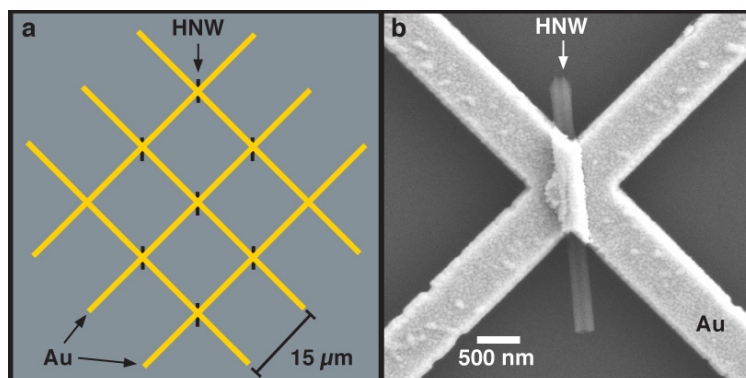


Figure 5.7: Schematic and image of HNWs with Au barriers. a) HNWs are aligned on the surface and Au barriers are placed on top of wires using EBL and metal evaporation. b) Scanning electron micrograph of HNW confined by Au barriers.

Aligning HNWs. In order to align HNWs on a surface we first start with creating alignment markers as a guide for a series of lithographic steps. A double-layer resist system (LOR/PMMA) was added to a SiO₂/Si sample surface and EBL was used to create alignment markers for subsequent lithography steps. After Au deposition and lift-off we spin coated PMMA resist onto the surface as previously, and performed EBL to form wells slightly larger than the HNW dimensions. After development and plasma ashing, we deposited the wires into the wells using a brushing technique. This was performed by rinsing a brush in IPA, touching the brush to the surface of the HNW sample, and then to the surface of the sample. After this, we removed the resist, leaving behind only the HNWs on the surface, and again added a double-layer resist (LOR/PMMA) to the sample. The sample was then exposed to EBL and metal evaporation to form Au barriers over the HNWs. Finally, excess Au and resist was removed and the sample was silanized with TMCS in order to promote functional HMM binding to the SiO₂ surface. Figure 5.7a shows a schematic of HNWs covered with Au lines in a diamond pattern used. Scanning electron microscopy was used to confirm confinement positions of HNWs (Figure 5.7b). The yield in each lithographic step reduced slightly, in lift-off, spin coating and alignment steps. The final yield of accessible HNWs in target positions was approximately 9%.

Transport of actin filaments through HNWs. After fabrication and silanization, we performed IVMA experiments with actin filaments and HMM as previously (see Ch. 2). HNWs that were identified as correctly confined under Au barriers were observed to either transport filaments or to be clogged by actin filaments. In the latter case, no transport was observed, as blockage was likely due to inactive HMM heads inside the HNWs. We therefore investigated those HNWs that seemed to transport filaments. Here we found that on average filaments were transported at a rate of ~4 filaments per minute (36 events in 5 min. for two HNWs

observed under identical conditions). An example of transport is shown in figure 5.8.

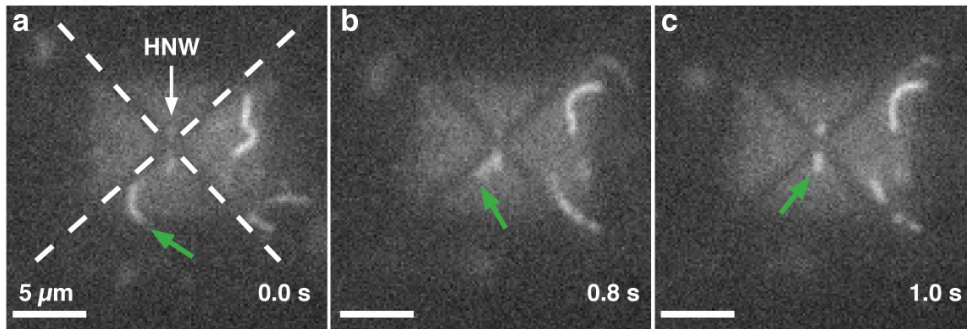


Figure 5.8: Fluorescence micrograph series of actin filament transport through HNW. a) Actin filament approaches the HNW (green arrow indicates trailing end of filament). b) Filament partially inside of the HNW. c) Filament inside the HNW with dark mid-section due to non-transparent Au. Scale bar: 5μm (a-c). Figure modified from Article V.

Active versus passive transport. The question as to whether actin filament transport is driven by HMM motors adsorbed inside the HNWs, or if it is diffusion based, is first addressed. We first tracked actin filaments traveling through two HNWs of length $l \approx 2.9 \mu\text{m}$ under identical conditions, figure 5.9. Then, we estimate the time required for actin filaments, of the same lengths, to diffuse (by 1D diffusion) through the length of a HNW, of similar dimensions to our experimental tests. The 1D translational diffusion coefficient for an actin filament (long rod-like object) moving close to a surface can be written as ^{199,200}:

$$D_t^s = \frac{k_b T}{2\pi\eta L} \left(\ln \frac{4r}{d} \right) \quad (5.2),$$

where $k_b T = 4.1 \cdot 10^{-21} \text{ J}$, $\eta = 1 \cdot 10^{-3} \text{ kg m}^{-1} \text{ s}^{-1}$, L is the filament length and $r = 40 \text{ nm}$, the distance from the underlying surface ¹⁹⁵. From equation 5.2, we can calculate the expected travel time t_p , of a filament diffusing through a HNW of length l as:

$$t_p = \frac{l^2}{2D_t^s} \quad (5.3).$$

Here we see that the travel time is relatively constant for long and short filaments, i.e. those filaments longer or shorter than the length of the HNW. However, the

expected travel time of a diffusing filament, based on equation 5.3, increases linearly with filament length.

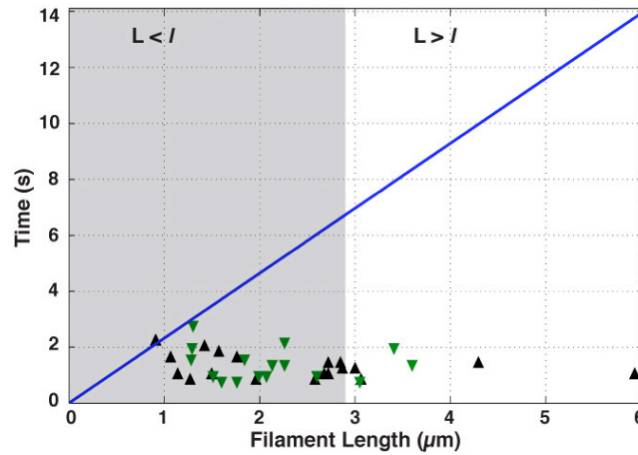


Figure 5.9: Comparison of active versus passive transport of actin filaments through HNWs. Experimental data for two HNWs of $l \approx 2.9 \mu\text{m}$ shown as black and green triangles demonstrating constant transport time for filaments of length (L) shorter and longer than the length of HNWs, respectively. Blue line shows estimated transport time for filaments based on equation 5.3. Figure modified from Article V.

We did not see a significant difference ($p = 0.54$, two-tailed unpaired t test) between the speeds of filaments traveling through the HNW having a shorter ($< 2.9 \mu\text{m}$, grey box in figure 5.9) or longer length than the HNW. However, we do see a significant difference ($p < 0.0001$, two-tailed unpaired t test) between the average speed of filaments traveling through the HNW in 1D ($2.44 \pm 0.14 \mu\text{m/s}$; mean \pm standard error of mean; $n = 36$) and those on the surface in 2D ($9.91 \pm 0.17 \mu\text{m/s}$; $n = 30$). Importantly, the consistent transport time for filaments shorter and longer than the length of the HNW lead us to believe that the transport is likely an active process, driven by HMM inside the HNW and not due to passive diffusion.

A full investigation into the cause of the reduction in speed for filaments inside HNWs was outside the scope of this study, however, some factors can be proposed. The most likely cause of a lower speed inside the HNW could be due to reduced number of HMM inside compared to outside³⁸. Alternatively, overcrowding of HNWs by filaments that become stuck inside, due to inactive HMM or sub-optimal diameters of the HNWs, could also be reasons for reduced speed inside.

5.2.2. Potential and future use

After confirmation of actin filament transport through HNWs, we propose that such architectural elements can be used as error-free crossings in a bio-computation device (see Ch. 4). These fully enclosed tunnels would essentially eliminate error at the pass junctions, as filaments would not be able to make wrong turns.

Furthermore, these HNWs could be used to add an extra element of control in the bio-computation network by electrostatic gating^{83,201}. This may be done by generating an electric field through the HNW, possibly using a back gate on the sample substrate and using the Au lines that cross over HNWs as top contacts. Under the influence of the highly localized electric field, the charged actin filaments could potentially be stopped and started.

Previously, HNWs have been investigated for cell injection studies, where they may be used as syringes in order to inject or extract molecules to and from cells^{118,130}. It may also be possible to use HNWs, with HMM adsorbed inside, in order to achieve directed transport of molecules, attached to actin filaments, into cells. Beyond these applications, the possibility to use the HNWs for more physiological studies is also interesting. As much of the work performed with actomyosin in conventional IVMA is limited to interactions in only 2D⁴⁶, or 1D⁸⁴, we have the capability here, to study HMM interaction in all directions around actin filaments, while maintaining 1D transport of filaments. With this higher level of interaction and the similarity to the physiological length scale for actin-myosin in the sarcomere, there is a further possibility to investigate the fundamental interactions of the myosin-actin complex²⁰².

6. Conclusions

Biosensing. Two separate devices and methods were presented here as potential biosensors. First, we demonstrated molecular concentration, with actin filaments propelled by HMM as probes, concentrated in a 2D plane. We achieved faster concentration, in a more highly miniaturized area, than previously developed devices based on kinesin molecular motors¹². While, the sensitivity or limit of detection of this device, has yet to be fully investigated, the potential utility of this device remains. With a high speed of operation and extremely miniaturized detection area, hundreds or even thousands of these devices can potentially be patterned in 1 mm² area onto a single chip, where readout can be performed quickly and accurately.

Secondly, we demonstrated the use of nanowires as biosensors. With this method of detection, we can observe a direct localization of fluorescence from target molecules (labeled actin filaments) by utilizing light-guiding properties of Al₂O₃ coated GaP nanowires. This method has promise as a future detection system, extending beyond molecular motors, to encompass a variety of fluorescent probe-based biosensing mechanisms²⁰³. For example, the nanowires can be used to detect analyte in an ELISA based assay⁹³, with the potential for higher signal-to-noise ratio due to their intrinsically higher surface-area-to-volume ratio. They may also be used to detect conformational information of cell membranes¹²⁹ or lipid bilayers¹³² coating the nanowires. The utility of such a system can be further developed, by tuning the physical dimensions of the nanowires, the spacing and surface chemistry, as required.

Computation. An alternative method to computation, using molecular motors, was also shown. We encoded a mathematical problem (the Subset Sum problem) into a 2D network, and used molecular motors to find all possible solutions. This entirely novel approach to solving such problems offers a potentially large improvement over alternative methods proposed, as they are not competitive in time efficiency, construction and cost or scaling up of the problem/solution space. The scaling up of the proof-of-concept biocomputation device shown here should, in principle, be realizable with the use of current state-of-the-art lithographic approaches, such as nano-imprint lithography, where full wafer-scale devices can be printed in a fraction of the time required for EBL techniques. The ability to scale up the size of the problem is a requirement, in order to demonstrate the utility of our

biocomputation method. A primary challenge for such a scaled up device would be in the monitoring of all exits in the device. As such, there may be other geometrical configurations, yet to be devised, which would prove to be more advantageous for fast readout of solutions.

Detection. Finally, localized detectors were proposed as useful components in biocomputation. The utility of FLIC can be found also in combination with the molecular concentration devices shown here. Where local FLIC effects can be used to enhance the fluorescence signal of pico or even femto molar concentrations of target molecules. These FLIC detectors can be highly useful for integrating more automated counting of large numbers of motile objects, a requirement for scaling in our biocomputation device. It should however, be considered how one should deal with data storage of a large-scale device, where observations for larger sets could lead to hours of IVMA recordings.

Hollow nanowires were also demonstrated to achieve actomyosin motility inside, i.e. transport of actin filaments by HMM motors within the 1D structures. As 1D tunnels, they can be of primary use in our biocomputation device, where complete control of motion must be achieved to enable error-free pass-junctions. The placement of these HNWs at each P-junction in a biocomputation network can be facilitated by the alignment strategy shown. Furthermore, electrostatic control of actin filaments traveling through HNWs may also be possible to integrate within a biocomputation network. These HNWs may also prove useful in the fundamental study of actin and myosin interactions as the dimensions are relevant to the physiological length scale of the sarcomere, the basic repeating unit in skeletal muscle.

Abbreviations

ADP – adenosine diphosphate

ALD – atomic layer deposition

Al₂O₃ – aluminum oxide

Aph – Alexa Fluor 488 phalloidin

ATP – adenosine triphosphate

CTR-LZ – control loading zone

CVD – chemical vapor phase deposition

DNA – deoxyribonucleic acid

EBL – electron beam lithography

ELISA – enzyme-linked immunosorbent assay

FET – field effect transistor

FITC - fluorescein isothiocyanate

FLIC – fluorescence interference contrast

GaP – Gallium Phosphide

HMM – heavy meromyosin

HNW – hollow nanowire

HSQ - hydrogen silsesquioxane

IPA – isopropanol

IVMA – *in vitro* motility assay

LMM – light meromyosin

LOR – lift off resist

LZ – loading zone

MOVPE – metalorganic vapor phase epitaxy

MIBK - methyl isobutyl ketone

NP - nondeterministic polynomial

P – polynomial

PH₃ - phosphine

P-junction – pass junction

PMMA – polymethyl methacrylate

PCR - polymerase chain reactions

Qubit – quantum binary digit

RhPh - rhodamine phalloidin

SAT - Boolean satisfiability problem

SEM – scanning electron microscopy

S-junction – split junction

SSP – subset sum problem

TMAI – trimethylaluminum

TMCS – trimethylchlorosilane

TMGa – trimethylgallium

TRITC – tetramethyl rhodamine iso-thiocyanate

TSP – travelling salesman problem

TZ – trapping zone

VLSI – very large scale integration

λ_{em} – wavelength of emission light

λ_{ex} – wavelength of excitation light

Acknowledgements

I would like to conclude this thesis by acknowledging those who have helped me along the way and in my PhD studies. First, I would like to thank my supervisors, Prof. Heiner Linke and Prof. Alf Månsson, for their great efforts in guiding me through these last four years and making this thesis possible. Heiner, I have nothing but appreciation for your tireless efforts in leading me through this work. From the beginning, you have always shown me respect and support and you have given me a chance to speak freely and become the scientist that I can call myself today. Alf, you are, by far, the most creative thinker I have had the pleasure to work with. You have also been consistently encouraging and supportive and have offered me an enormous amount of inspiration in my scientific progress. Thank you both for everything.

I spent a great deal of my time, during these years in Kalmar, working with the PhD students and post docs of Prof. Månsson's group and I would like to say a special thank you to them as well. To my close collaborators: Dr. Malin Persson and Dr. Lasse ten Siethoff, which I have worked most with on my projects. I offer my humble gratitude. As the last in our (MONAD) group to finish, I consider myself lucky to have had the opportunity to learn and grow from you both. Malin, you are extremely sharp (in wit and rationale) and kind, and it has been a pleasure to work alongside and learn from you. Lasse, you are an endearing and genuinely honest individual, who I am very blessed to call my friend. I will always appreciate the conversations that we had during these years and hope they will continue in the future. I wish you both the best in all your future endeavors. I would also like to thank Dr. Saroj Kumar and Dr. Elina Bengtsson. Our work was not always easy, but it was fun. Thank you Saroj, for having a great sense of humor and Elina, for being so kind.

Here in Lund, I also had the pleasure of working with a few special individuals. To the members of the bio-group, to whom I owe much gratitude: Karl Adolfsson, Dr. Martina Balaz, Dr. Jason Beech, Dr. Johanna Generosi, Stefan Holm, Cassandra Niman and Henrik Persson. You have all helped me to improve my work and to become a better educator, thank you so much for your time and consideration. I would also like to thank the senior members of our bio-group, Dr. Christelle Prinz and Dr. Jonas Tegenfeldt, for meaningful and stimulating conversations throughout these years. I am highly appreciative of your openness

and eagerness in the interest of science. To Dr. Ivan Maximov, thank you, for being so kind and for always having the time to discuss the difficult challenges we have faced in our MONAD and ABACUS work. To Jan-Göran Gluschke, I owe you so much for your kindness and support through those most difficult times in my PhD, you are a true friend, *vielen danke*.

I would also like to thank my collaborators from outside of Sweden. Prof. Stefan Diez, and Dr. Till Korten thank you both for your insightful discussions and for your unflinching commitment to see the work through. Prof. Dan Nicolau Sr. thank you for keeping a sense of humor through all of this and for your guidance through MONAD and into ABACUS, I am proud to have been a part of your vision. Dr. Dan Nicolau Jr. thank you for sharing your vast knowledge of mathematics. Dr. Falco van Delft, thank you for all the valuable discussions and for your dedication to problem solving. Joanna Hajne, thank you for being such a great person and friend. I hope to be able to visit you more in the future.

Till FTF faculty och tekniska och administrativa personal: *ett stort tack till er alla!*

I would like to give a special thank you to the She-Wolf pack: Sofia Falvik Svensson, Dr. Sepideh Gorji Ghalamestani, Dr. Karla Hillerich, Linda Johansson, Sofia Johansson, Dr. Maria Messing, and Susanne Norlén. I am indebted to you all for making my time here so much more special than I ever thought it could be. To the best office-mate ever Gustav Nylund. Thanks for making my time here easier.

To my friends and family back home, who have guided me on my journey before choosing to become a scientist. I want to say thank you for everything. My friends: Melanie Chapman, Grazzia Morash, Erin J. Mulliken, Heather K. Shockey, and Brandi Westrom, you are the glue that holds it all together. To my family including my brothers: Joseph, Michael, David, Jeff, Paul, Kenneth and Matthew, and my dear sisters: Mary, Donna, DeAnna, Karen, Marjorie, Judy, Hope, Holly, Faith, Grace and Jolene thank you for your continued love and support. Sometimes, I wish I could teleport home to visit *y'all* for the weekends.

Mercy Lard

Lund University

1 August 2014

References

- 1 Nicolau, D. V., Suzuki, H., Mashiko, S., Taguchi, T. & Yoshikawa, S. Actin motion on microlithographically functionalized myosin surfaces and tracks. *Biophys. J.* **77**, 1126-1134 (1999).
- 2 Hiratsuka, Y., Tada, T., Oiwa, K., Kanayama, T. & Uyeda, T. Q. Controlling the direction of kinesin-driven microtubule movements along microlithographic tracks. *Biophys. J.* **81**, 1555-1561. (2001).
- 3 Schroeder, V., Korten, T., Linke, H., Diez, S. & Maximov, I. Dynamic guiding of motor-driven microtubules on electrically heated, smart polymer tracks. *Nano Lett* **13**, 3434-3438 (2013).
- 4 Hess, H., Clemmens, J., Qin, D., Howard, J. & Vogel, V. Light-controlled molecular shuttles made from motor proteins carrying cargo on engineered surfaces. *Nano Lett* **1**, 235-239 (2001).
- 5 Hess, H. Engineering applications of biomolecular motors. *Annu. Rev. Biomed. Eng.* **13**, 429-450 (2011).
- 6 Korten, T., Mansson, A. & Diez, S. Towards the application of cytoskeletal motor proteins in molecular detection and diagnostic devices. *Curr. Opin. Biotechnol.* **21**, 477-488 (2010).
- 7 Rivet, C., Lee, H., Hirsch, A., Hamilton, S. & Lu, H. Microfluidics for medical diagnostics and biosensors. *Chem. Eng. Sci.* **66**, 1490-1507 (2011).
- 8 Whitesides, G. M. The origins and the future of microfluidics. *Nature* **442**, 368-373 (2006).
- 9 Jokerst, J. V. *et al.* Programmable nano-bio-chip sensors: Analytical meets clinical. *Anal. Chem.* **82**, 1571-1579 (2010).
- 10 Chiu, D. T., Pezzoli, E., Wu, H., Stroock, A. D. & Whitesides, G. M. Using three-dimensional microfluidic networks for solving computationally hard problems. *P Natl Acad Sci USA* **98**, 2961-2966 (2001).
- 11 Lard, M. *et al.* Ultrafast molecular motor driven nanoseparation and biosensing. *Biosens. Bioelectron.* **48**, 145-152 (2013).
- 12 Lin, C. T., Kao, M. T., Kurabayashi, K. & Meyhofer, E. Self-contained, biomolecular motor-driven protein sorting and concentrating in an ultrasensitive microfluidic chip. *Nano Lett* **8**, 1041-1046 (2008).
- 13 Katira, P. & Hess, H. Two-stage capture employing active transport enables sensitive and fast biosensors. *Nano Lett* **10**, 567-572 (2010).
- 14 Nicolau, D. V. J., Lard, M., Korten, T., van Delft, F., Persson, M., Bengtsson, E., Månsson, A., Diez, S., Linke, H., Nicolau, D. V. Parallel computation using self-propelled biological agents in nanofabricated networks. *Submitted* (2014).
- 15 Nitta, T., Hess, H. Dispersion in active transport by kinesin-powered molecular shuttles. *Nano Lett* **5**, 1337-1342 (2005).
- 16 Sheehan, P. E., Whitman, L. J. Detection limits for nanoscale biosensors. *Nano Lett* **5**, 803-807 (2005).

- 17 Bachand, G. D., Hess, H., Ratna, B., Satir, P. & Vogel, V. "Smart dust"
biosensors powered by biomolecular motors. *Lab Chip* **9**, 1661-1666,
doi:10.1039/B821055A (2009).
- 18 Fischer, T., Agarwal, A. & Hess, H. A smart dust biosensor powered by kinesin
motors. *Nat. Nanotechnol.* **4**, 162-166 (2009).
- 19 Barabási, A.-L. & Albert, R. Emergence of scaling in random networks. *Science*
286, 509-512 (1999).
- 20 Yan, G., Zhou, T., Hu, B., Fu, Z.-Q. & Wang, B.-H. Efficient routing on complex
networks. *Phys. Rev. E* **73**, 046108 (2006).
- 21 Diffie, W. & Hellman, M. E. New directions in cryptography. *IEEE Trans. Inf.*
Theory **22**, 644-654 (1976).
- 22 Merkle, R. & Hellman, M. Hiding information and signatures in trapdoor
knapsacks. *IEEE Trans. Inf. Theory* **24**, 525-530 (1978).
- 23 Rivest, R. L., Shamir, A. & Adleman, L. A method for obtaining digital
signatures and public-key cryptosystems. *Commun. ACM* **21**, 120-126 (1978).
- 24 Fraenkel, A. S. Complexity of protein folding. *Bull. Math. Biol.* **55**, 1199-1210
(1993).
- 25 Berger, B. & Leighton, T. Protein folding in the hydrophobic-hydrophilic (HP)
model is NP-complete. *J. Comput. Biol.* **5**, 27-40 (1998).
- 26 Crescenzi, P., Goldman, D., Papadimitriou, C., Piccolboni, A. & Yannakakis, M.
On the complexity of protein folding. *J. Comput. Biol.* **5**, 423-465 (1998).
- 27 Adleman, L. M. Molecular computation of solutions to combinatorial problems.
Science **266**, 1021-1024 (1994).
- 28 Lipton, R. DNA solution of hard computational problems. *Science* **268**, 542-545
(1995).
- 29 DiVincenzo, D. P. Quantum computation. *Science* **270**, 255-261 (1995).
- 30 Nicolau Jr, D. V. & Nicolau, D. V. Biocomputation schemes based on the
directed and directional movements of motile biological objects. *Proc. SPIE*
5651, 134-143 (2005).
- 31 Huxley, H. E. Structural difference between resting and rigor muscle; Evidence
from intensity changes in the low-angle equatorial X-ray diagram. *J. Mol. Biol.*
37, 507-520 (1968).
- 32 Millman, B. M. The filament lattice of striated muscle. *Physiol. Rev.* **78**, 359-391
(1998).
- 33 Ebashi, S. & Endo, M. Calcium and muscle contraction. *Prog. Biophys. Mol.*
Biol. **18**, 123-183 (1968).
- 34 Huxley, H. E. The mechanism of muscular contraction. *Science* **164**, 1356-1365
(1969).
- 35 Gordon, A. M., Homsher, E. & Regnier, M. Regulation of contraction in striated
muscle. *Physiol. Rev.* **80**, 853-924 (2000).
- 36 Rayment, I. & Holden, H. M. The three-dimensional structure of a molecular
motor. *Trends Biochem. Sci.* **19**, 129-134 (1994).
- 37 Winkelmann, D. A., Baker, T. S. & Rayment, I. Three-dimensional structure of
myosin subfragment-1 from electron microscopy of sectioned crystals. *J. Cell*
Biol. **114**, 701-713 (1991).
- 38 Uyeda, T. Q. P., Kron, S. J. & Spudich, J. A. Myosin step size: estimation from
slow sliding movement of actin over low densities of heavy meromyosin. *J. Mol.*
Biol. **214**, 699-710 (1990).

- 39 Månsson, A. Actomyosin-ADP states, interhead cooperativity, and the force-
velocity relation of skeletal muscle. *Biophys. J.* **98**, 1237-1246 (2010).
- 40 Piazzesi, G., Lucii, L., Lombardi, V. The size and the speed of the working stroke
of muscle myosin and its dependence on the force. *J. Physiol.* **545**, 145-151
(2002).
- 41 Barclay, C. J. Estimation of cross-bridge stiffness from maximum thermodynamic
efficiency. *J. Muscle Res. Cell Motil.* **19**, 855-864 (1998).
- 42 Stewart, M. & Edwards, P. Length of myosin rod and its proteolytic fragments
determined by electron microscopy. *FEBS Lett.* **168**, 75-78 (1984).
- 43 Margossian, S. S. & Lowey, S. Preparation of myosin and its subfragments from
rabbit skeletal muscle. *Methods Enzymol.* **85**, 55-71 (1982).
- 44 Holmes, K. C., Popp, D., Gebhard, W., Kabsch, W. Atomic model of the actin
filament. *Nature* **347**, 44-49 (1990).
- 45 Sheetz, M. P. & Spudich, J. A. Movement of myosin-coated fluorescent beads on
actin cables in vitro. *Nature* **303**, 31-35 (1983).
- 46 Kron, S. J. & Spudich, J. A. Fluorescent actin filaments move on myosin fixed to
a glass surface. *P Natl Acad Sci USA* **83**, 6272-6276 (1986).
- 47 Howard, J., Hudspeth, A. J. & Vale, R. D. Movement of microtubules by single
kinesin molecules. *Nature* **342**, 154-158 (1989).
- 48 Kron, S. J., Toyoshima, Y. Y., Uyeda, T. Q. & Spudich, J. A. Assays for actin
sliding movement over myosin-coated surfaces. *Methods Enzymol.* **196**, 399-416
(1991).
- 49 Kabsch, W., Mannherz, H. G., Suck, D., Pai, E. F., Holmes, K. C. Atomic
structure of the actin: DNase I complex. *Nature* **347**, 37-44 (1990).
- 50 Balaz, M. & Månsson, A. Detection of small differences in actomyosin function
using actin labeled with different phalloidin conjugates. *Anal. Biochem.* **338**, 224-
236 (2005).
- 51 Ruhnaw, F., Zwicker, D. & Diez, S. Tracking single particles and elongated
filaments with nanometer precision. *Biophys. J.* **100**, 2820-2828 (2011).
- 52 Månsson, A. & Tågerud, S. Multivariate statistics in analysis of data from the in
vitro motility assay. *Anal. Biochem.* **314**, 281-293 (2003).
- 53 Månsson, A., Bunk, R., Sundberg, M., Montelius, L. Self-organization of motor-
propelled cytoskeletal filaments at topographically defined borders. *J. Biomed.
Biotechnol.* **2012** (2012).
- 54 Hess, H., Clemmens, J., Howard, J. & Vogel, V. Surface imaging by self-
propelled nanoscale probes. *Nano Lett* **2**, 113-116 (2002).
- 55 Sundberg, M. *et al.* Selective spatial localization of actomyosin motor function by
chemical surface patterning. *Langmuir* **22**, 7302-7312 (2006).
- 56 Kumar, S. *et al.* Antibodies covalently immobilized on actin filaments for fast
myosin driven analyte transport. *PLoS One* **7**, e46298 (2012).
- 57 Patolsky, F., Weizmann, Y. & Willner, I. Actin-based metallic nanowires as bio-
nanotransporters. *Nat. Mater.* **3**, 692-695 (2004).
- 58 Sundberg, M. *et al.* Actin filament guidance on a chip: toward high-throughput
assays and lab-on-a-chip applications. *Langmuir* **22**, 7286-7295 (2006).
- 59 Takatsuki, H. *et al.* Transport of single cells using an actin bundle-myosin
bionanomotor transport system. *Nanotechnology* **22**, 245101 (2011).
- 60 Bunk, R. *et al.* Guiding motor-propelled molecules with nanoscale precision
through silanized bi-channel structures. *Nanotechnology* **16**, 710-717 (2005).

- 61 Sundberg, M. *et al.* Silanized surfaces for in vitro studies of actomyosin function
and nanotechnology applications. *Anal. Biochem.* **323**, 127-138 (2003).
- 62 Månsson, A. Translational actomyosin research: fundamental insights and
applications hand in hand. *J. Muscle Res. Cell Motil.* **33**, 219-233 (2012).
- 63 Wang, J. Cargo-towing synthetic nanomachines: towards active transport in
microchip devices. *Lab Chip* **12**, 1944-1950 (2012).
- 64 Agarwal, A. & Hess, H. Biomolecular motors at the intersection of
nanotechnology and polymer science. *Prog. Polym. Sci.* **35**, 252-277 (2010).
- 65 Ramachandran, S., Ernst, K. H., Bachand, G. D., Vogel, V. & Hess, H. Selective
loading of kinesin-powered molecular shuttles with protein cargo and its
application to biosensing. *Small* **2**, 330-334 (2006).
- 66 van den Heuvel, M. G., de Graaff, M. P. & Dekker, C. Molecular sorting by
electrical steering of microtubules in kinesin-coated channels. *Science* **312**, 910-
914 (2006).
- 67 van den Heuvel, M. G. L. & Dekker, C. Motor proteins at work for
nanotechnology. *Science* **317**, 333-336 (2007).
- 68 Soto, C. M., Martin, B. D., Sapsford, K. E., Blum, A. S. & Ratna, B. R. Toward
single molecule detection of staphylococcal enterotoxin B: mobile sandwich
immunoassay on gliding microtubules. *Anal. Chem.* **80**, 5433-5440 (2008).
- 69 Vale, R. D. *et al.* Direct observation of single kinesin molecules moving along
microtubules. *Nature* **380**, 451-453 (1996).
- 70 Choi, D. S., Byun, K.-E. & Hong, S. Dual transport systems based on hybrid
nanostructures of microtubules and actin filaments. *Small* **7**, 1755-1760 (2011).
- 71 Dennis, J. R., Howard, J., Vogel, V. Molecular shuttles: directed motion of
microtubules along nanoscale kinesin tracks. *Nanotechnology* **10**, 232 (1999).
- 72 Clemmens, J., Hess, H., Howard, J. & Vogel, V. Analysis of microtubule
guidance in open microfabricated channels coated with the motor protein kinesin.
Langmuir **19**, 1738-1744 (2002).
- 73 Bunk, R. *et al.* Actomyosin motility on nanostructured surfaces. *Biochem.*
Biophys. Res. Commun. **301**, 783-788 (2003).
- 74 Bunk, R., Carlberg, P., Månsson, A., Nicholls, I., A., Omling, P., Sundberg, M.,
Tågerud, S., Montelius, L. Guiding molecular motors with nano-imprinted
structures. *Jpn. J. Appl. Phys.* **44**, 3337 (2005).
- 75 Clemmens, J., Hess, H., Lipscomb, R., Hanein, Y., Böhringer, K. F., Matzke, C.
M., Bachand, G. D., Bunker, B. C., Vogel, V. Mechanisms of microtubule
guiding on microfabricated kinesin-coated surfaces: Chemical and topographic
surface patterns. *Langmuir* **19**, 10967-10974 (2003).
- 76 Hess, H., Matzke, C. M., Doot, R. K., Clemmens, J., Bachand, G. D., Bunker, B.
C., Vogel, V. Molecular shuttles operating undercover: A new photolithographic
approach for the fabrication of structured surfaces supporting directed motility.
Nano Lett **3**, 1651-1655 (2003).
- 77 Huang, Y.-M., Uppalapati, M., Hancock, W. & Jackson, T. Microtubule transport,
concentration and alignment in enclosed microfluidic channels. *Biomed.*
Microdevices **9**, 175-184 (2007).
- 78 van den Heuvel, M. G. L., Butcher, C. T., Smeets, R. M. M., Diez, S. & Dekker,
C. High rectifying efficiencies of microtubule motility on kinesin-coated gold
nanostructures. *Nano Lett* **5**, 1117-1122 (2005).
- 79 Vikhorev, P. G. *et al.* Diffusion dynamics of motor-driven transport: Gradient
production and self-organization of surfaces. *Langmuir* **24**, 13509-13517 (2008).
- 92

- 80 Clemmens, J., Hess, H., Doot, R., Matzke, C. M., Bachand, G. D., Vogel, V. Motor-protein "roundabouts": Microtubules moving on kinesin-coated tracks through engineered networks. *Lab Chip* **4**, 83-86 (2004).
- 81 Nitta, T., Tanahashi, A., Obara, Y., Hirano, M., Razumova, M., Regnier, M., Hess, H. Comparing guiding track requirements for myosin- and kinesin-powered molecular shuttles. *Nano Lett* **8**, 2305-2309 (2008).
- 82 Lee, Y., Carroll, L., Holland, L., Famouri, P. in *IEEE Conf. Nanotechnol.*, 8th. 667-672.
- 83 Riveline, D. *et al.* Acting on actin: the electric motility assay. *Eur. Biophys. J.* **27**, 403 (1998).
- 84 Byun, K. E., Heo, K., Shim, S., Choi, H. J., Hong, S. Functionalization of silicon nanowires with actomyosin motor protein for bioinspired nanomechanical applications. *Small* **5**, 2659-2664 (2009).
- 85 Kim, K. *et al.* Microtubule shuttles on kinesin-coated glass micro-wire tracks. *Biomed. Microdevices*, 1-8 (2014).
- 86 Byun, K.-E., Kim, M.-G., Chase, P. B. & Hong, S. Selective assembly and guiding of actomyosin using carbon nanotube network monolayer patterns. *Langmuir* **23**, 9535-9539 (2007).
- 87 Sikora, A. *et al.* Molecular motor-powered shuttles along multi-walled carbon nanotube tracks. *Nano Lett* **14**, 876-881 (2014).
- 88 Byun, K.-E. *et al.* Graphene-polymer hybrid nanostructure-based bioenergy storage device for real-time control of biological motor activity. *ACS Nano* **5**, 8656-8664 (2011).
- 89 Eunji, K. *et al.* Electrical control of kinesin-microtubule motility using a transparent functionalized-graphene substrate. *Nanotechnology* **24**, 195102 (2013).
- 90 Albet-Torres, N. *et al.* Mode of heavy meromyosin adsorption and motor function correlated with surface hydrophobicity and charge. *Langmuir* **23**, 11147-11156 (2007).
- 91 Wanekaya, A. K., Chen, W., Myung, N. V. & Mulchandani, A. Nanowire-based electrochemical biosensors. *Electroanalysis* **18**, 533-550 (2006).
- 92 Hoa, X. D., Kirk, A. G. & Tabrizian, M. Towards integrated and sensitive surface plasmon resonance biosensors: A review of recent progress. *Biosens. Bioelectron.* **23**, 151-160 (2007).
- 93 Engvall, E. & Perlmann, P. Enzyme-linked immunosorbent assay, Elisa: III. Quantitation of specific antibodies by enzyme-labeled anti-immunoglobulin in antigen-coated tubes. *J. Immunol.* **109**, 129-135 (1972).
- 94 Bachand, G. D., Rivera, S. B., Carroll-Portillo, A., Hess, H., Bachand, M. Active capture and transport of virus particles using a biomolecular motor-driven, nanoscale antibody sandwich assay. *Small* **2**, 381-385 (2006).
- 95 Carroll-Portillo, A., Bachand, M., Bachand, G. D. Directed attachment of antibodies to kinesin-powered molecular shuttles. *Biotechnol. Bioeng.* **104**, 1182-1188 (2009).
- 96 Månsson, A. *et al.* In vitro sliding of actin filaments labelled with single quantum dots. *Biochem. Biophys. Res. Commun.* **314**, 529-534 (2004).
- 97 Persson, M. *et al.* Transportation of nanoscale cargoes by myosin propelled actin filaments. *PLoS ONE* **8**, e55931 (2013).
- 98 Brunner, C., Wahnes, C., Vogel, V. Cargo pick-up from engineered loading stations by kinesin driven molecular shuttles. *Lab Chip* **7**, 1263-1271 (2007).

- 99 Kumar, S., ten Siethoff, L., Persson, M., Albet-Torres, N., Månsson, A. Magnetic capture from blood rescues molecular motor function in diagnostic nanodevices. *J. Nanobiotechnol.* **11** (2013).
- 100 Gao, A. *et al.* Signal-to-noise ratio enhancement of silicon nanowires biosensor with rolling circle amplification. *Nano Lett* **13**, 4123-4130 (2013).
- 101 Chu, C.-J. *et al.* Improving nanowire sensing capability by electrical field alignment of surface probing molecules. *Nano Lett* **13**, 2564-2569 (2013).
- 102 Fu, T.-M. *et al.* Sub-10-nm intracellular bioelectronic probes from nanowire–nanotube heterostructures. *Proc. Natl. Acad. Sci. U.S.A.* (2014).
- 103 Qing, Q., Jiang, Z., Xu, L., Gao, R., Mai, L., Lieber, C. M. Free-standing kinked nanowire transistor probes for targeted intracellular recording in three dimensions. *Nat. Nanotechnol.* **9**, 142-147 (2014).
- 104 Bonde, S. *et al.* Tuning InAs nanowire density for HEK293 cell viability, adhesion, and morphology: Perspectives for nanowire-based biosensors. *ACS Appl. Mater. Interfaces* **5**, 10510-10519 (2013).
- 105 Na, Y.-R. *et al.* Probing enzymatic activity inside living cells using a nanowire–cell “sandwich” assay. *Nano Lett* **13**, 153-158 (2012).
- 106 Persson, H. *et al.* Fibroblasts cultured on nanowires exhibit low motility, impaired cell division, and DNA damage. *Small* **9**, 4006-4016 (2013).
- 107 Curreli, M. *et al.* Real-time, label-free detection of biological entities using nanowire-based FETs. *IEEE Trans. Nanotechnol.* **7**, 651-667 (2008).
- 108 Gao, Z. *et al.* Silicon nanowire arrays for label-free detection of DNA. *Anal. Chem.* **79**, 3291-3297 (2007).
- 109 Cui, Y., Wei, Q., Park, H. & Lieber, C. M. Nanowire nanosensors for highly sensitive and selective detection of biological and chemical species. *Science* **293**, 1289-1292 (2001).
- 110 Patolsky, F. & Lieber, C. M. Nanowire nanosensors. *Mater. Today* **8**, 20-28 (2005).
- 111 Zheng, G., Patolsky, F., Cui, Y., Wang, W. U., Lieber, C. M. Multiplexed electrical detection of cancer markers with nanowire sensor arrays. *Nat. Biotechnol.* **23**, 1294-1301 (2006).
- 112 Noor, M. O. & Krull, U. J. Silicon nanowires as field-effect transducers for biosensor development: A review. *Anal. Chim. Acta* **825**, 1-25 (2014).
- 113 Gao, X. P. A., Zheng, Gengfeng, Lieber, Charles M. Subthreshold regime has the optimal sensitivity for nanowire FET biosensors. *Nano Lett* **10**, 547-552 (2009).
- 114 Zhou, W. *et al.* Long term stability of nanowire nanoelectronics in physiological environments. *Nano Lett* **14**, 1614-1619 (2014).
- 115 Chen, K.-I., Li, B.-R. & Chen, Y.-T. Silicon nanowire field-effect transistor-based biosensors for biomedical diagnosis and cellular recording investigation. *Nano Today* **6**, 131-154 (2011).
- 116 Stern, E., Klemic, J. F., Routenberg, D. A., Wyrembak, P. N., Turner-Evans, D. B., Hamilton, A. D., LaVan, D. A., Fahmy, T. M., Reed, M. A. Label-free immunodetection with CMOS-compatible semiconducting nanowires. *Nature* **445**, 519-522 (2007).
- 117 Hällström, W. *et al.* Gallium phosphide nanowires as a substrate for cultured neurons. *Nano Lett* **7**, 2960-2965 (2007).
- 118 Persson, H. *et al.* Vertical oxide nanotubes connected by subsurface microchannels. *Nano Res.* **5**, 190-198 (2012).

- 119 Mårtensson, T., Borgström, M., Seifert, W., Ohlsson, B. J. & Samuelson, L.
Fabrication of individually seeded nanowire arrays by vapour–liquid–solid
growth. *Nanotechnology* **14**, 1255 (2003).
- 120 Dick, K. A. *et al.* Control of III–V nanowire crystal structure by growth parameter
tuning. *Semicond. Sci. Technol.* **25**, 024009 (2010).
- 121 Seifert, W. *et al.* Growth of one-dimensional nanostructures in MOVPE. *J. Cryst.
Growth* **272**, 211-220 (2004).
- 122 Wacaser, B. A. *et al.* Preferential interface nucleation: An expansion of the VLS
growth mechanism for nanowires. *Adv. Mater.* **21**, 153-165 (2009).
- 123 Hällström, W. *et al.* Rectifying and sorting of regenerating axons by free-standing
nanowire patterns: a highway for nerve fibers. *Langmuir* **25**, 4343-4346 (2009).
- 124 Yan, R., Gargas, D., Yang, P. Nanowire photonics. *Nat. Photonics* **3**, 569-576
(2009).
- 125 Law, M. *et al.* Nanoribbon waveguides for subwavelength photonics integration.
Science **305**, 1269-1273 (2004).
- 126 Paniagua-Dominguez, R., Grzela, G., Rivas, J. G. & Sanchez-Gil, J. A. Enhanced
and directional emission of semiconductor nanowires tailored through
leaky/guided modes. *Nanoscale* **5**, 10582-10590 (2013).
- 127 Anttu, N. Geometrical optics, electrostatics, and nanophotonic resonances in
absorbing nanowire arrays. *Opt. Lett.* **38**, 730-732 (2013).
- 128 Adolffson, K. *et al.* Fluorescent nanowire heterostructures as a versatile tool for
biology applications. *Nano Lett* **13**, 4728-4732 (2013).
- 129 Silvius, J. R. & Nabi, I. R. Fluorescence-quenching and resonance energy transfer
studies of lipid microdomains in model and biological membranes (Review). *Mol.
Membr. Biol.* **23**, 5-16 (2006).
- 130 VanDersarl, J. J., Xu, A. M. & Melosh, N. A. Nanostraws for direct fluidic
intracellular access. *Nano Lett* **12**, 3881-3886 (2011).
- 131 Shalek, A. K. *et al.* Vertical silicon nanowires as a universal platform for
delivering biomolecules into living cells. *Proc. Natl. Acad. Sci. U.S.A.* **107**, 1870-
1875 (2010).
- 132 Dabkowska, A. P. *et al.* Fluid and highly curved model membranes on vertical
nanowire arrays. *Nano Lett*, doi:10.1021/nl500926y (2014).
- 133 Mårtensson, T. *et al.* Nanowire arrays defined by nanoimprint lithography. *Nano
Lett* **4**, 699-702 (2004).
- 134 Karp, R. M. in *Complexity of Computer Computations* (ed R. E. Miller and J. W.
Thatcher) 85-103 (Plenum Press, The IBM Research Symposia Series, New York,
NY, 1972).
- 135 Garey, M. R. & Johnson, D. S. *Computers and Intractability: A Guide to the
Theory of NP-Completeness*. (W. H. Freeman & Co., 1979).
- 136 Bokhari, S. S. Parallel solution of the subset-sum problem: an empirical study.
Concurr. Comp-Pract. E. **24**, 2241-2254 (2012).
- 137 Fortnow, L. The status of the P versus NP problem. *Commun. ACM* **52**, 78-86
(2009).
- 138 Bellmore, M. & Nemhauser, G. L. The traveling salesman problem: A survey.
Oper. Res. **16**, 538-558 (1968).
- 139 Schnorr, C. P. & Euchner, M. Lattice basis reduction: Improved practical
algorithms and solving subset sum problems. *Math. Program.* **66**, 181-199
(1994).

- 140 Kate, A. & Goldberg, I. Generalizing cryptosystems based on the subset sum
problem. *Int. J. Inf. Secur.* **10**, 189-199 (2011).
- 141 Naor, M. & Segev, G. Public-key cryptosystems resilient to key leakage. *SIAM J.*
Comput. **41**, 772-814 (2012).
- 142 Chor, B. & Rivest, R. L. A knapsack-type public key cryptosystem based on
arithmetic in finite fields. *IEEE T. Inform. Theory* **34**, 901-909 (1988).
- 143 Impagliazzo, R. & Naor, M. Efficient cryptographic schemes provably as secure
as subset sum. *J. Cryptology* **9**, 199-216 (1996).
- 144 Proctor, R. A. Solution of two difficult combinatorial problems with linear
algebra. *Am. Math. Mon.* **89**, 721-734 (1982).
- 145 Tomohiro, S., Taro, T. & Hidetoshi, N. Statistical mechanics of an NP-complete
problem: subset sum. *J. Phys. A: Math. Gen.* **34**, 9555 (2001).
- 146 Roweis, S. A. M. *et al.* A sticker-based model for DNA computation. *J. Comput.*
Biol. **5**, 615-629 (1998).
- 147 Liu, Q. *et al.* DNA computing on surfaces. *Nature* **403**, 175-179 (2000).
- 148 Hartmanis, J. On the weight of computations. *Bull. Eur. Assoc. Theor. Comput.*
Sci. **55**, 136-138 (1995).
- 149 Braich, R. S., Chelyapov, N., Johnson, C., Rothmund, P. W. K. & Adleman, L.
Solution of a 20-variable 3-SAT problem on a DNA computer. *Science* **296**, 499-
502 (2002).
- 150 Boneh, D., Dunworth, C., Lipton, R. J. & Sgall, J. i. On the computational power
of DNA. *Discrete Appl. Math.* **71**, 79-94 (1996).
- 151 Qian, L. & Winfree, E. Scaling up digital circuit computation with DNA strand
displacement cascades. *Science* **332**, 1196-1201 (2011).
- 152 Martínez-Pérez, I. M. & Zimmermann, K.-H. Parallel bioinspired algorithms for
NP complete graph problems. *J. Parallel Distr. Com.* **69**, 221-229 (2009).
- 153 Deutsch, D. Quantum theory, the Church-Turing principle and the universal
quantum computer. *Proc. R. Soc. London, Ser. A* **400**, 97-117 (1985).
- 154 Borresen, J. & Lynch, S. Neuronal computers. *Nonlinear Anal-Theor.* **71**, e2372-
e2376 (2009).
- 155 Ouyang, Q., Kaplan, P. D., Liu, S. & Libchaber, A. DNA solution of the maximal
clique problem. *Science* **278**, 446-449 (1997).
- 156 Ezziane, Z. DNA computing: Applications and challenges. *Nanotechnology* **17**,
R27-R39 (2006).
- 157 Benenson, Y., Gil, B., Ben-Dor, U., Adar, R., Shapiro, E. An autonomous
molecular computer for logical control of gene expression. *Nature* **429**, 423-429
(2004).
- 158 Macdonald, J. *et al.* Medium scale integration of molecular logic gates in an
automaton. *Nano Lett* **6**, 2598-2603 (2006).
- 159 Winfree, E., Liu, F., Wenzler, L. A. & Seeman, N. C. Design and self-assembly
of two-dimensional DNA crystals. *Nature* **394**, 539-544 (1998).
- 160 Rothmund, P. W. K. Folding DNA to create nanoscale shapes and patterns.
Nature **440**, 297-302 (2006).
- 161 Chengde Mao, T. H. L., John H. Reif, Nadrian C. Seeman. Logical computation
using algorithmic self-assembly of DNA triple-crossover molecules. *Nature* **407**,
493-496 (2000).
- 162 Gil, B., Kahan-Hanum, M., Skirtenko, N., Adar, R. & Shapiro, E. Detection of
multiple disease indicators by an autonomous biomolecular computer. *Nano Lett*
11, 2989-2996 (2011).

- 163 Benenson, Y., Paz-Elizur, T., Adar, R., Keinan, E., Livneh, Z., Shapiro, E. Programmable and autonomous computing machine made of biomolecules. *Nature* **414**, 430-434 (2001).
- 164 Feynman, R. Simulating physics with computers. *Int. J. Theor. Phys.* **21**, 467-488 (1982).
- 165 Cohen, E. & Tamir, B. D-Wave and predecessors: From simulated to quantum annealing. *Int. J. Quant. Inf.* **12**, 1430002 (2014).
- 166 Černý, V. Quantum computers and intractable (NP-complete) computing problems. *Phys. Rev. A* **48**, 116-119 (1993).
- 167 Lloyd, S. A potentially realizable quantum computer. *Science* **261**, 1569-1571 (1993).
- 168 Ladd, T. D. *et al.* Quantum computers. *Nature* **464**, 45-53 (2010).
- 169 Shor, P. W. Scheme for reducing decoherence in quantum computer memory. *Phys. Rev. A* **52**, R2493-R2496 (1995).
- 170 Hisao, K. in *Silicon Nanoelectron. Opt. Sci. Eng.* (ed David K. Ferry) 65-87 (CRC Press, 2005).
- 171 Singh, A., Bharadwaj, L. & Harpreet, S. DNA and quantum based algorithms for VLSI circuits testing. *Nat. Comput.* **4**, 53-72 (2005).
- 172 Martin-Lopez, E., Laing, A., Lawson, T., Alvarez, R., Zhou, X.-Q., O'Brien, J. L. Experimental realization of Shor's quantum factoring algorithm using qubit recycling. *Nat. Photonics* **6**, 773-776 (2012).
- 173 Xu, N. *et al.* Quantum factorization of 143 on a dipolar-coupling nuclear magnetic resonance system. *Phys. Rev. Lett.* **108**, 130501 (2012).
- 174 Reed, M. D., DiCarlo, L., Nigg, S. E., Sun, L., Frunzio, L., Girvin, S. M., Schoelkopf, R. J. Realization of three-qubit quantum error correction with superconducting circuits. *Nature* **482**, 382-385 (2012).
- 175 Hopfield, J. J. & Tank, D. W. "Neural" computation of decisions in optimization problems. *Biol. Cybern.* **52**, 141-152 (1985).
- 176 Kohonen, T. An introduction to neural computing. *Neural Networks* **1**, 3-16 (1988).
- 177 Basheer, I. A. & Hajmeer, M. Artificial neural networks: fundamentals, computing, design, and application. *J. Microbiol. Methods* **43**, 3-31 (2000).
- 178 Hopfield, J. J. & Tank, D. W. Computing with neural circuits: a model. *Science* **233**, 625-633 (1986).
- 179 Chua, L. O. & Yang, L. Cellular neural networks: applications. *IEEE T. Circuits Syst.* **35**, 1273-1290 (1988).
- 180 Szoke, A., Daneu, V., Goldhar, J. & Kurnit, N. A. Bistable optical element and its applications. *Appl. Phys. Lett.* **15**, 376-379 (1969).
- 181 Lynch, S. & Steele, A. L. Controlling chaos in nonlinear optical resonators. *Chaos, Solitons and Fractals* **11**, 721-728 (2000).
- 182 Smith, S. D. Optical bistability: Towards the optical computer. *Nature* **307**, 315-316 (1984).
- 183 Steele, A. L., Lynch, S. & Hoad, J. E. Analysis of optical instabilities and bistability in a nonlinear optical fibre loop mirror with feedback. *Opt. Commun.* **137**, 136-142 (1997).
- 184 Sawchuk, A. A. & Strand, T. C. Digital optical computing. *Proc. IEEE* **72**, 758-779 (1984).
- 185 Meservey, R. & Tedrow, P. M. Spin-polarized electron tunneling. *Phys. Rep.* **238**, 173-243 (1994).

- 186 Behin-Aein, B., Datta, D., Salahuddin, S., Datta, S. Proposal for an all-spin logic
device with built-in memory. *Nat. Nano.* **5**, 266-270 (2010).
- 187 Grover, W. H. & Mathies, R. A. An integrated microfluidic processor for single
nucleotide polymorphism-based DNA computing. *Lab Chip* **5**, 1033-1040 (2005).
- 188 Vikhorev, P. G., Vikhoreva, N. N. & Månsson, A. Bending flexibility of actin
filaments during motor-induced sliding. *Biophys. J.* **95**, 5809-5819 (2008).
- 189 Sun, H. Q., Yamamoto, M., Mejillano, M. & Yin, H. L. Gelsolin, a
multifunctional actin regulatory protein. *J. Biol. Chem.* **274**, 33179-33182 (1999).
- 190 Gepner, P., Fraser, D. L. & Gamayunov, V. Evaluation of the 3rd generation Intel
core processor focusing on HPC applications. *Technology* **7**, i7-2600 (2012).
- 191 Ajo-Franklin, C. M., Yoshina-Ishii, C. & Boxer, S. G. Probing the structure of
supported membranes and tethered oligonucleotides by fluorescence interference
contrast microscopy. *Langmuir* **21**, 4976-4983 (2005).
- 192 Lambacher, A. & Fromherz, P. Luminescence of dye molecules on oxidized
silicon and fluorescence interference contrast microscopy of biomembranes. *J Opt
Soc Am B* **19**, 1435-1453 (2002).
- 193 Parthasarathy, R. & Groves, J. T. Optical techniques for imaging membrane
topography. *Cell Biochem. Biophys.* **41**, 391-414 (2004).
- 194 Kerssemakers, J., Howard, J., Hess, H. & Diez, S. The distance that kinesin-1
holds its cargo from the microtubule surface measured by fluorescence
interference contrast microscopy. *P Natl Acad Sci USA* **103**, 15812-15817 (2006).
- 195 Persson, M. *et al.* Heavy meromyosin molecules extending more than 50 nm
above adsorbing electronegative surfaces. *Langmuir* **26**, 9927-9936 (2010).
- 196 Toyoshima, Y. Y., Kron, S. J. & Spudich, J. A. The myosin step size:
measurement of the unit displacement per ATP hydrolyzed in an in vitro assay. *P
Natl Acad Sci USA* **87**, 7130-7134 (1990).
- 197 Messing, M. *et al.* A comparative study of the effect of gold seed particle
preparation method on nanowire growth. *Nano Res.* **3**, 506-519 (2010).
- 198 Lim, J. K. *et al.* Alignment strategies for the assembly of nanowires with
submicron diameters. *Small* **6**, 1736-1740 (2010).
- 199 Howard, J. *Mechanics of Motor Proteins and the Cytoskeleton.* (Sinauer
Associates, 2001).
- 200 Hunt, A. J., Gittes, F. & Howard, J. The force exerted by a single kinesin
molecule against a viscous load. *Biophys. J.* **67**, 766-781 (1994).
- 201 Jia, L., Moorjani, S., Jackson, T. & Hancock, W. Microscale transport and sorting
by kinesin molecular motors. *Biomed. Microdev.* **6**, 67-74 (2004).
- 202 Sanger, J. *et al.* How to build a myofibril. *J. Muscle Res. Cell Motil.* **26**, 343-354
(2005).
- 203 Anttu, N., Dabkowska, A., Lard, M., Linke, H., Månsson, A., Niman, C.,
Ohlsson, J., Prinz, C. Optical molecular nanowire sensor. Patent application
EP1478073 (Unpublished) patent (2014).